On the formation mechanisms and properties of MAX phases
A review

Zhang, Zhuo; Duan, Xiaoming; Jia, Dechang; Zhou, Yu; van der Zwaag, Sybrand

DOI
10.1016/j.jeurceramsoc.2021.02.002

Publication date
2021

Document Version
Final published version

Published in
Journal of the European Ceramic Society

Journal of the European Ceramic Society 41 (2021) 3851–3878

Contents lists available at ScienceDirect

Journal of the European Ceramic Society

journal homepage: www.elsevier.com/locate/jeurceramsoc

Review article

On the formation mechanisms and properties of MAX phases: A review

Zhuo Zhang [a,b,c], Xiaoming Duan [a,b,*], Dechang Jia [a,b], Yu Zhou [a,b], Sybrand van der Zwaag [c,**]

[a] Key Laboratory of Advanced Structural-Functional Integration Materials & Green Manufacturing Technology, Harbin Institute of Technology, Harbin, 150001, China
[b] Institute for Advanced Ceramics, School of Materials Science and Engineering, Harbin Institute of Technology, Harbin, 150001, China
[c] Novel Aerospace Materials Group, Faculty of Aerospace Engineering, Delft University of Technology, 2629HS, Delft, The Netherlands

ARTICLE INFO

Keywords:
MAX phases
Formation mechanisms
Point defects
Solid solutions
Texture

ABSTRACT

MAX phases are a family of ternary carbide or nitride ceramics possessing a layered crystal structure and, due to their chemical bonds having a mixed covalent-ionic-metallic nature, have unique properties combining those of metals and ceramics. In this review, the formation mechanisms of MAX phases from elemental and compound powders are reviewed in detail, as the formation mechanisms are closely related to the unique properties of well-synthesized MAX phases. The stability of MAX phases in some harsh external environments is significantly influenced by the defect population, allowing the mechanisms of defect formation and migration to strongly influence their self-healing performance and radiation tolerance. The properties of MAX phases can be tailored by creating solid solutions, which have lattice distortions, and texturing which results in the preferential orientation of plate-like grains.

1. Introduction

MAX phases are a family of ternary carbide or nitride ceramics all belonging to the hexagonal crystal system and having a layered structure. Their general formula is $M_{n+1}AX_n$, where n usually equals 1~3, M is a transition metal element, A is an A group element and X is C or N. In the last two years, also some MAX phase ceramics with B as the X element have been synthesized [1–3]. Depending on the value of n, the early generation of MAX phases are classified as 211 phases, 312 phases and 413 phases [4–6]. Their crystal structure can be described as $M_{n+1}X_n$ layers and A layers alternately stacked along the c-axis, as shown in Fig. 1 [7]. The $M_{n+1}X_n$ layers consist of edge-shared M_6X octahedra with strong M—X bonds, while the $M_{n+1}X_n$ layers and A layers are combined by the relatively weak M—A bonds. Recently, some other phases with higher "n" values have also been discovered in the MAX family, such as 523 phases ($Ti_5Al_2C_3$), 615 phases (Ta_6AlC_5), 725 phases ($Ti_7Si_2C_5$), *etc.* [8]. Unlike bonds in real ceramics, chemical bonds in MAX phases have a mixed covalent-ionic-metallic nature, which results in their unique properties combining those of ceramics and metals, such as being machinable and ductile, light and strong, electrically and thermally conductive, having good oxidation resistance, remarkably high temperature stability and good thermal shock resistance, *etc.* [9–11], making them an ideal family of materials suitable for many fields such as thermal shock resistant refractory materials, coatings for electrical contacts, neutron radiation resistant parts for nuclear applications, *etc.* [12–14].

Due to the relatively weak M—A bonds between the $M_{n+1}X_n$ layers and A layers, A atoms tend to diffuse outwards and be oxidized more easily when exposed to oxygen at high temperatures. As a result, existing microcracks can be filled by the volume expansion caused by the formation of the A oxides. Therefore, MAX phases are prominent examples of intrinsic self-healing materials [15–17]. The rapid diffusion of A atoms is realized by the formation and migration of point defects; furthermore, the outward diffusion of A atoms will result in the change of compositions, forming substoichiometric $M_{n+1}A_{1-x}X_n$ phases. Thus, point defects in MAX phases and the stability of defective MAX phases have an important effect on the oxidation resistance and self-healing performance of MAX phases [18,19]. Point defects in MAX phases have also been reported to have a strong relationship with their radiation tolerance, which is important for neutron radiation resistant parts [20].

As MAX phases have a lamellar crystal structure, their properties along different crystal directions are different. If a favorable external condition, such as a uniaxial pressure or a magnetic field, is applied

* Corresponding author at: Key Laboratory of Advanced Structural-Functional Integration Materials & Green Manufacturing Technology, Harbin Institute of Technology, Harbin, 150001, China.
** Corresponding author at: Novel Aerospace Materials Group, Faculty of Aerospace Engineering, Delft University of Technology, 2629HS, Delft, The Netherlands
E-mail addresses: dxmhit@126.com (X. Duan), S.vanderZwaag@tudelft.nl (S. van der Zwaag).

https://doi.org/10.1016/j.jeurceramsoc.2021.02.002
Received 13 October 2020; Received in revised form 1 February 2021; Accepted 3 February 2021
Available online 12 February 2021

during the preparation process of MAX phases, lamellar grains can be preferentially aligned along specific directions, forming textured MAX phases possessing anisotropic properties [21–23]. Texturing of MAX phases can significantly improve their properties along specific directions and extend their application fields.

In this review, an overview of the formation mechanisms of MAX phases from elemental and compound powders is given. In addition, point defects and their influence on the self-healing performance and radiation tolerance, the use of solid solutions to tailor properties, and texture formation and anisotropic properties of MAX phases are discussed.

2. Formation mechanisms

As a MAX phase is composed of three different elements, it must be synthesized from mixed powders of several kinds of elemental or binary compound powders containing the three elements. In this section, the formation mechanisms of MAX phases from different starting materials are discussed.

2.1. Formation mechanisms from elemental powders

The formation process of MAX phases from elemental powders necessarily contains several steps. As the structure of MAX phases can be divided into the $M_{n+1}X_n$ layers consisting of edge-shared M_6X octahedra with the strong M—X bonds and the A layers combined with the $M_{n+1}X_n$ layers by the weak M—A bonds, it is reasonable to speculate that the M_xX_y compound could be an intermediate phase during the synthesis process of MAX phases, which has been proven to be consistent with many experimental results.

Hashimoto et al. [24] studied the formation mechanism of Ti_2AlC from 2Ti:1Al:1C powders during self-propagating high-temperature synthesis (SHS). After ignition, the exothermic reaction between Ti and C forming TiC leads to the melting of Al, which forms an Al-Ti liquid phase. Subsequently, these TiC crystals are dissolved into the Al-Ti liquid phase, forming Ti_2AlC. Such a formation process of Ti_2AlC has also been proven by Thomas et al. [25] who studied the effect of particle sizes of the carbon sources on the phase compositions of samples produced from 2Ti:1Al:1C powders. When carbon fibers were used as the carbon source, the contact area between Al and Ti increased due to the shape and size of carbon fibers, resulting in a high thermal conductivity of the cold pressed reactant. Ti_3Al alloy and TiC would be formed very fast, and then there would be a rapid cooling. The holding time at high temperatures would not be long enough for formation of Ti_2AlC from Ti-Al and TiC, as shown in Fig. 2(a). When graphite or carbon black powders were used as the carbon source, the contact area between Al and Ti decreased because they were surrounded by carbon, resulting in a low thermal conductivity of the cold pressed reactant which led to a much slower propagation of the combustion wave and ensured the completion of the reaction between Ti-Al and TiC to form Ti_2AlC, as shown in Fig. 2(b).

Similar results have also been obtained for the formation process of other MAX phases during SHS or other synthesis methods. Meng et al. [26] studied the reaction paths of SHS-ed Ti_3SiC_2 by quenching at the bottom of a V-groove filled with mixed 3Ti:1Si:2C powders right after ignition, and analyzed the phase compositions of different layers of the sample, as shown in Fig. 3. With the decrease of heat dissipation from bottom to top of the sample, the content of Ti_3SiC_2 increased while the content of TiC and Ti_5Si_3 decreased, indicating a more completed reaction from bottom to top, and demonstrating that TiC and Ti_5Si_3 are the main intermediate phases during the synthesis process of Ti_3SiC_2 from elemental powders. For Cr_2AlC prepared from 2Cr:1.2Al:1C powders by

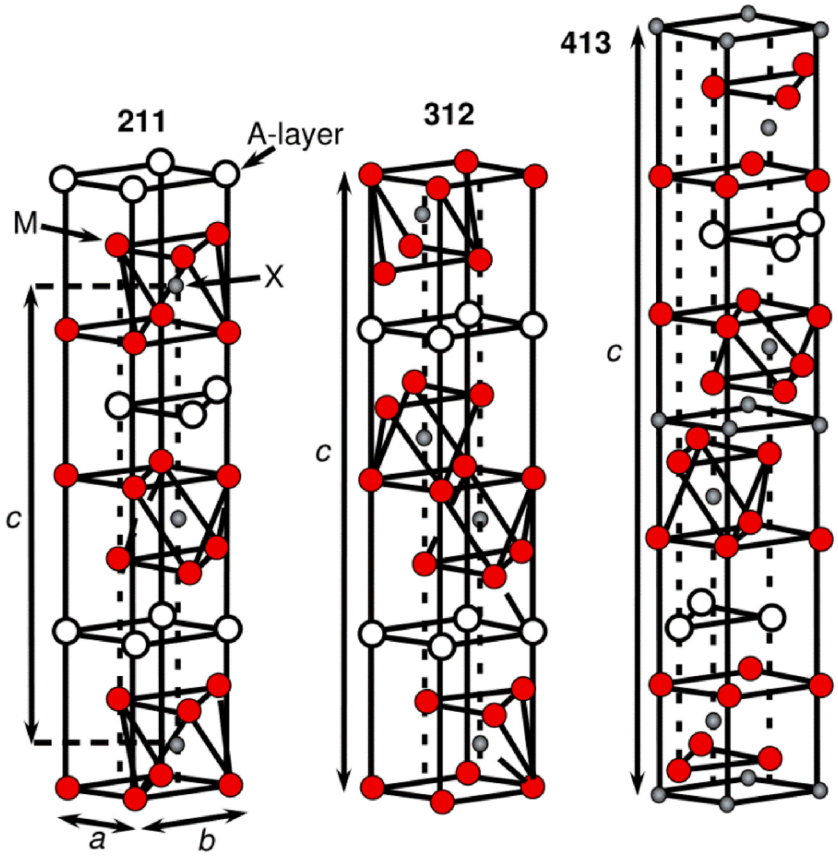

Fig. 1. Schematic diagram of the crystal structures of $M_{n+1}AX_n$ phases with different n values. Reproduced with permission from Ref. [7], © 2016 Elsevier B.V.

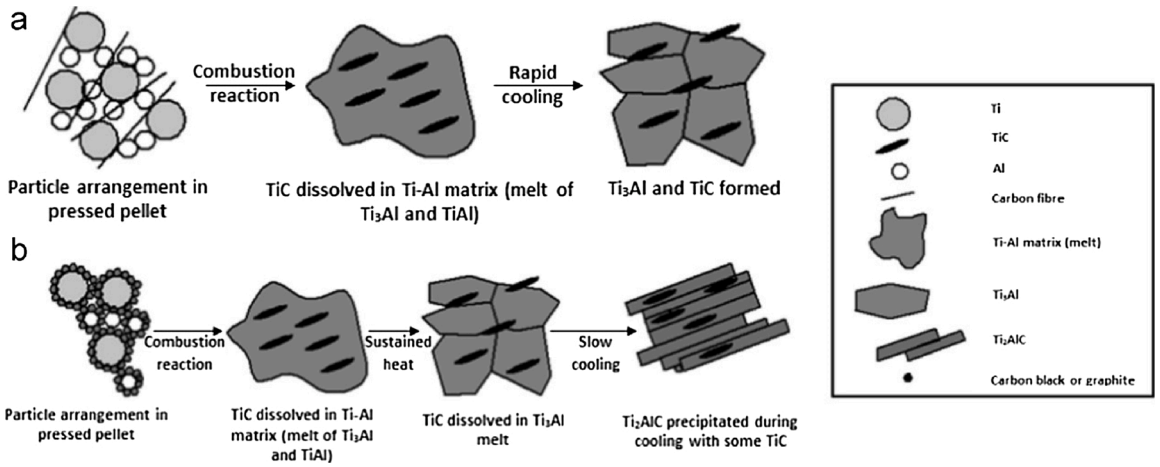

Fig. 2. Schematic diagram of the SHS process of 2Ti:1Al:1C powders with different carbon sources: (a) carbon fibers; (b) carbon black or graphite powders. Reproduced with permission from Ref. [25], © 2015 Elsevier Ltd and Techna Group S.r.l.

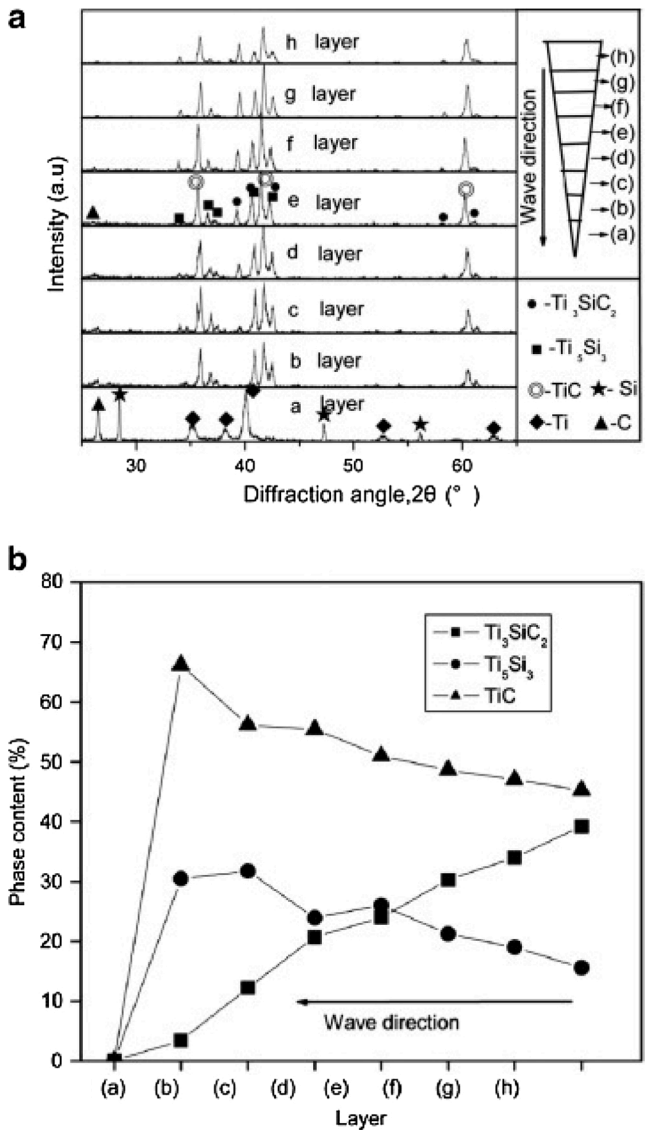

Fig. 3. (a) XRD patterns and (b) phase compositions of different sample layers prepared from mixed 3Ti:1Si:2C powders after combustion front quenching. Reproduced with permission from Ref. [26], © 2013 Elsevier Ltd.

spark plasma sintering (SPS), Cr_7C_3 and Cr-Al alloys (Al_8Cr_5, $AlCr_2$) were formed first (at 700~800 °C) and then react to form Cr_2AlC, as shown in Fig. 4 [27]. TiN and Ti-Al alloys (Ti_3Al, TiAl) were also observed to be formed first and then react to synthesize Ti_2AlN for hot pressed samples from Ti-Al-N amorphous powders [28]. For MAX phase borides Zr_2SB and Hf_2SB synthesized *via* solid-state reactions from the stoichiometric mixtures of elemental powders, 15 wt.% ZrB_2 and 1 wt.% HfB_2 were also found to exist in the final samples [29].

The reaction process from M- A-X elemental powders leading to MAX phases can be summarized as elemental powders reacting to form M_xX_y phases and M_xA_y compounds first, then M_xX_y phases are dissolved into M_xA_y compounds to form MAX phases. To improve the purity of the synthesized MAX phases, a higher elemental A content in the starting materials than in the targeted MAX product is needed to make up for the vaporization loss of the A element during the high temperature synthesis, otherwise there would be residual M_xX_y phases or MAX phases with higher *n* values in the final product. While too high an elemental A content in the starting materials could result in the residual M_xA_y compounds [30–32]. Besides this, a prolonged holding time, or a higher synthesis temperature, could lead to more vaporization of the A element and an impurity residue in the product; while too low a temperature or too short a holding time is not enough for the complete reaction to form MAX phases [33–37]. Therefore, the adjustments of the elemental A

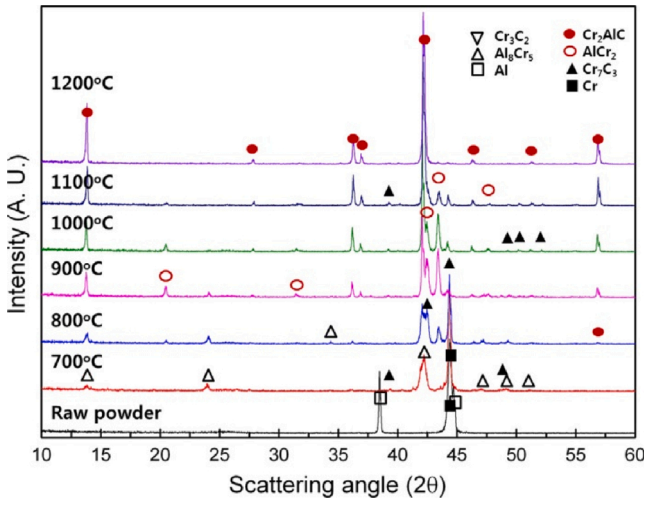

Fig. 4. XRD patters of raw 2Cr:1.2Al:1C powders and the SPS-ed samples prepared at different temperatures.
Reproduced with permission from Ref. [27], © 2013 Elsevier B.V.

content in the starting materials, the synthesis temperature and holding time are important to obtain MAX phases with a high purity.

2.2. Formation mechanisms from compound powders

As discussed in Section 2.1, M_xX_y and M_xA_y are two types of intermediate compounds during the synthesis of MAX phases from elemental powders. If the intermediate compounds are used as the starting materials, the reaction barrier to form MAX phases can be significantly reduced, thus making it possible to synthesize MAX phases with a higher purity or a decrease in their synthesis temperature.

The M—A bonds between the $M_{n+1}X_n$ layers and A layers are relatively weaker than the M—X bonds inside the $M_{n+1}X_n$ layers, which make it possible to prepare MAX phases by the intercalation of the A layers into the M_xX_y compounds with X vacancies. Riley et al. [38] first demonstrated this preparation idea by preparing SPS-ed Ti_3AlC_2 bulk samples using Al and mechanically alloyed $TiC_{0.67}$ powders. Ti_3AlC_2 bulk samples were synthesized within 1 h at 1000 °C, which is 400~600 °C lower than the temperature required for SPS using elemental powders. The *in situ* neutron diffraction patterns during SPS are shown in Fig. 5. The absorption of Al by $TiC_{0.67}$ occurred accompanied by the ordering of carbon vacancies in $TiC_{0.67}$ (point B), and Ti_3AlC_2 began to be synthesized at point C.

The synthesis temperature of MAX phases by such an intercalation method can be further decreased by long-time annealing. Wang et al. [39] successfully prepared Ti_2AlC coatings by long-time annealing the as-deposited $TiC_{0.65}$-Al alternatingly stacked multilayer coatings at a temperature as low as 550 °C. The $TiC_{0.65}$-Al layer boundaries

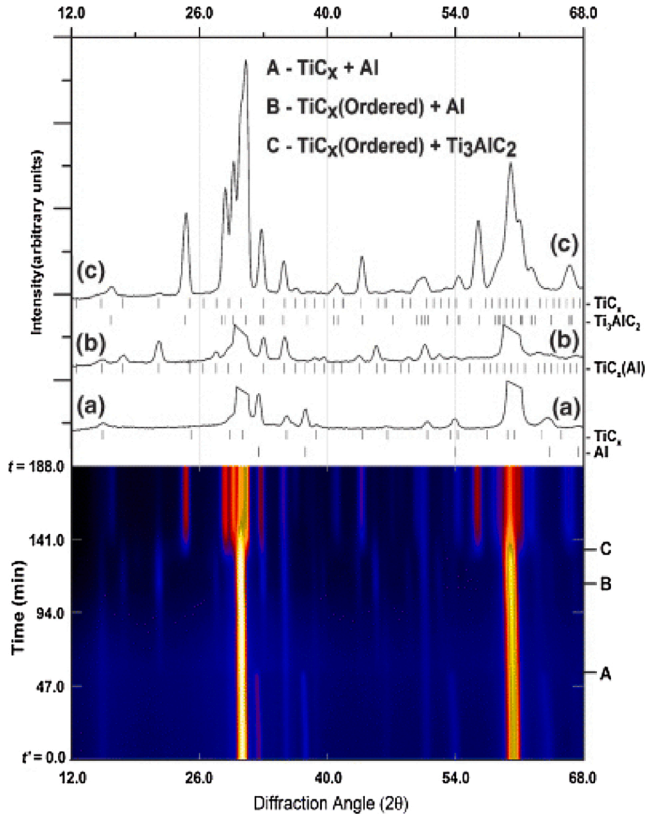

Fig. 5. Neutron diffraction intensity versus diffraction angle and time (Intensity is represented by color; letters mark significant stages during SPS) and the corresponding diffraction patterns at these stages: (a, A) The melting of Al at 660 °C; (b, B) Al absorbed by $TiC_{0.67}$ accompanied by its spontaneously ordering at 700 °C; (c, C) the beginning of Ti_3AlC_2 formation.
Reproduced with permission from Ref. [38], © 2007 The American Ceramic Society.

disappeared after annealing at 550 °C for 100 h, forming Ti_2AlC (Fig. 6 (a–f)). The content of Ti_2AlC increases with increasing the annealing temperature or prolonging the annealing time (Fig. 6(g)). It needs to be noted that a prolongation of the annealing time could be more effective than an increase in the annealing temperature, which can be seen from the sample annealed at 580 °C for 100 h, which has a much higher Ti_2AlC content than one annealed at 600 °C for 20 h. During low-temperature long-time annealing, Al atoms diffuse into $TiC_{0.65}$ and replace carbon vacancies. With the prolongation of annealing, the structure of $TiC_{0.65}$-Al solid solution becomes more ordered where perfect Ti_2C layers are intercalated by the Al layers, as shown in Fig. 6(h). It has also been proven that using $TiC_{0.6}$ and Al powders as the starting materials can lower the sintering temperature and shorten the holding time to prepare Ti_3AlC_2 bulk samples with a higher purity and an improved flexural strength [40]. The study of the crystallographic relationship between Ti_3SiC_2 and TiC also provided a theoretical support for the preparation of Ti_3SiC_2 from TiC_x and Si by such an intercalation method [41].

Even when M_xA_y compound powders and X elemental powders are used as the starting materials, MAX phases would still be formed *via* the intermediate phases M_xX_y, which themselves can be formed by the diffusion of the X element into the M_xA_y compounds. Xiao et al. [42] studied the formation mechanism of Ti_2AlC from carbon coated Ti-Al alloy slices during hot pressing (HP). Firstly, carbon atoms diffuse into the Ti-Al alloy and form a TiC_x layer between the Ti-Al alloy and carbon. Under these conditions, there are many carbon vacancies and residual Al atoms in the TiC_x region away from carbon and near to the Ti-Al alloy, which make Al atoms easily diffuse into TiC_x and replace these carbon vacancies, forming Ti_2AlC. Stacking faults and micro-twins generated in the Ti-Al alloy under the uniaxial pressure provide fast atomic diffusion channels and act as quick nucleation zones for TiC_x.

The introduction of intermediate phases M_xX_y in the starting materials is a more favorable route to improve the purity of MAX phases in the final product. Meng et al. [26] compared the phase compositions of the SHS-ed samples prepared using 3Ti:1SiC:1C powders and 1Ti:1Si:2TiC powders, as shown in Fig. 7. Samples prepared using 1Ti:1Si:2TiC powders have a higher Ti_3SiC_2 content and lower intermediate phases (TiC and Ti_5Si_3) content than those prepared using 3Ti-SiC-C powders. Using Cr_3C_2 as the carbon source (Fig. 8) is also more favorable for the Cr_2AlC phase formation as it allows a lower synthesis temperature than using elemental powders (Fig. 4) [27]. The introduction of TiC as the carbon source and the introduction of TiN as the nitrogen source were both proven to be beneficial to the purity improvement of Ti_3AlC_2 and Ti_2AlN phases, respectively [43,44].

3. Point defects in MAX phases

The natural behavior of intrinsic point defects in MAX phases has a significant and positive influence on the neutron radiation tolerance and self-healing performance of MAX phases. In this section, the research on the defective properties of MAX phases including defect formation and defect migration are reviewed. The stability of MAX phases with A vacancies, which is related to their self-healing performance, and the radiation tolerance of MAX phases, which is largely determined by their defective properties (mainly the formation of M_A-A_M anti-site pairs) are discussed in detail.

3.1. Formation and migration of point defects

The intrinsic point defects in MAX phases can be divided into vacancies, interstitial atoms and anti-site defects. For M_2AX phases, there are 3 types of vacancies (V_M, V_A, and V_X) and 6 types of anti-site defects (M_A, M_X, A_M, A_X, X_M, and X_A); while for M_nAX_{n-1} phases (n > 2), there are more types of vacancies and anti-site defects due to different chemical environments for the M atoms. For example, there are 2 types of Ti atoms for Ti_3AC_2 phases, Ti_I and Ti_{II} at 2*a* (0, 0, 0) and 4*f* (1/3, 2/3,

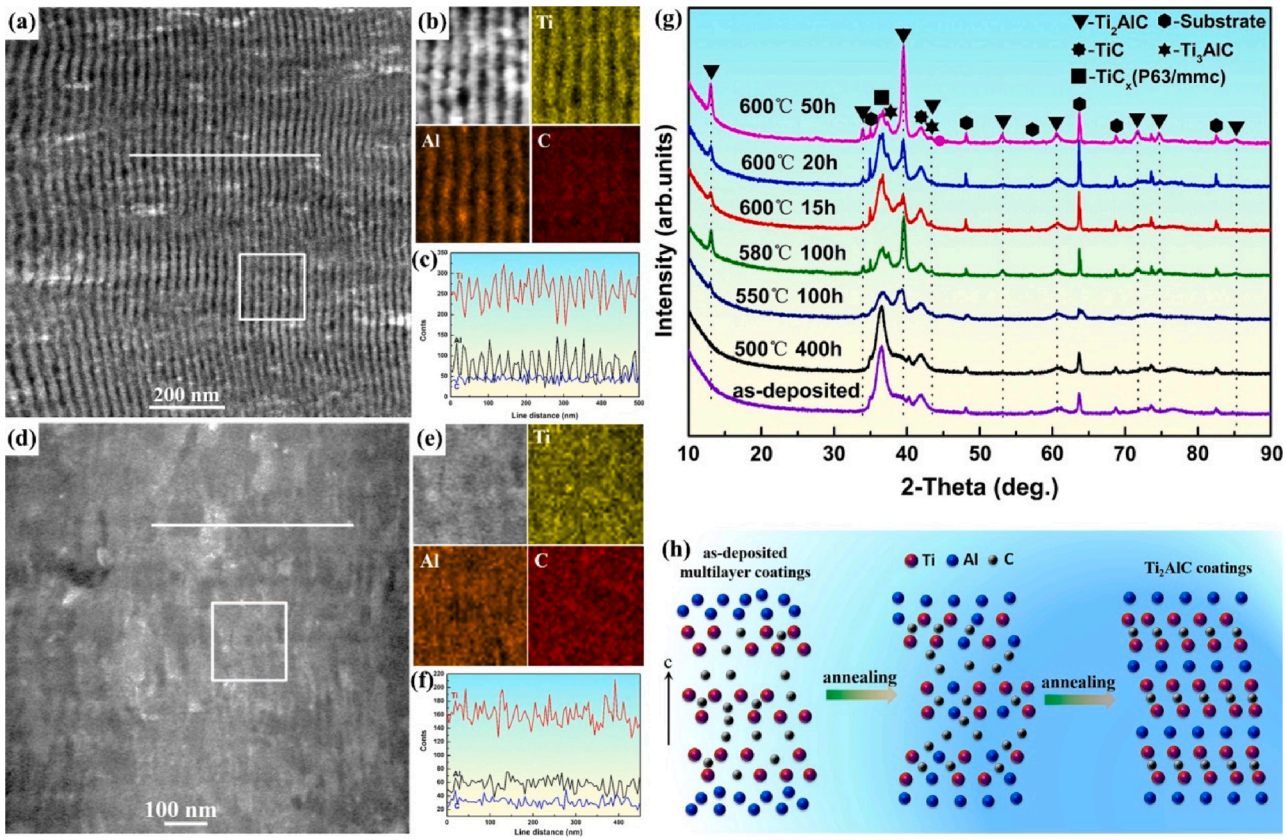

Fig. 6. Preparation of Ti_2AlC coatings by low-temperature long-time annealing: (a~c) STEM analysis of the deposited $TiC_{0.65}$/Al multilayer coatings: (a) STEM image, (b) energy dispersive X-ray spectroscopy (EDX/EDS) mapping of the square area in (a), and (c) elemental concentrations from EDS line scan along the line in (a); (d~f) STEM analysis of coatings annealed at 550 °C for 100 h: (d) STEM image, (e) EDS mapping of the square area in (d), and (f) elemental concentrations from EDS line scan along the line in (d); (g) XRD patterns of coatings annealed at different temperatures for different time; (h) Schematic diagram of the formation process of Ti_2AlC during annealing of the as-deposited $TiC_{0.65}$/Al multilayer coatings.
Reproduced with permission from Ref. [39], © 2019 Elsevier B.V.

z) Wyckoff positions, respectively, as shown in Fig. 9 [45], thus there are 4 types of vacancies and 8 types of anti-site defects. While the positions of interstitial atoms are more complex. Taking Ti_3AC_2 phases as an example (Fig. 9), its crystal structure can be divided into 2 blocks, the ATi_{II} and Ti_3C_2 blocks. The initial interstitial positions in the ATi_{II} block include the *a*, *b*, *c*, and *d* positions between the A atomic layer and Ti_{II} atomic layer, the *b*, *c*, and *d* positions in the A atomic layer, and the *a*, *c*, and *d* positions in the Ti_{II} atomic layer. The initial interstitial positions in the Ti_3C_2 block include the I-Ti_{II}C position between the Ti_{II} atomic layer and C atomic layer, the I-Ti_IC position between the Ti_I atomic layer and C atomic layer, the I-Ti_I position in the Ti_I atomic layer, and the I-C position in the C atomic layer. Interstitial atoms on different interstitial positions have different defect formation energies. Some positions, which vary depending on the compositions of MAX phases, are dynamically unstable [45,46]. The formation energies of interstitial atoms mentioned in the following text refer to those thermodynamically stable positions with the lowest formation energies. Generally, the formation energy of a point defect is lower when it is located in the $M_{n+1}A$ block than in the $M_{n+1}X_n$ block, which is attributed to the relatively weak M—A bonds between the $M_{n+1}X_n$ layers and A layers [20,45].

Upon the formation of an interstitial atom, an atom leaves its lattice position and then is embedded in an interstitial position, forming a Frenkel pair consisting of a vacancy at the original lattice position of this atom and an interstitial atom at the interstitial position. The formation of Frenkel pairs (FP) in MAX phases is related to their structural stability in some harsh external environments (*e.g.*, neutron radiation). Lower formation energies of FP indicate more persistent defects which can lead to a disordering of the structure [46]. If a vacancy is occupied by an interstitial atom near to this vacancy, the two point defects will be annihilated, which is called *i-v* recombination [47]. If the interstitial atom during this *i-v* recombination is not the same as the original atom at this vacancy, an anti-site defect will be formed. Using the Kr ö ger-Vink notation [48], the formation of anti-site defects by *i-v* recombination in MAX phases can be described as Eqs. (1–6) [49]:

$$M_i + V_X \rightarrow M_X \quad (1)$$

$$X_i + V_M \rightarrow X_M \quad (2)$$

$$A_i + V_X \rightarrow A_X \quad (3)$$

$$X_i + V_A \rightarrow X_A \quad (4)$$

$$A_i + V_M \rightarrow A_M \quad (5)$$

$$M_i + V_A \rightarrow M_A \quad (6)$$

Furthermore, an interstitial atom could also take the place of a nearby lattice atom, making the original lattice atom become a new interstitial atom. The displacement of lattice atoms by interstitial atoms can be described as Eqs. (7–12) [49]:

$$M_i + X_X \rightarrow M_X + X_i \quad (7)$$

$$X_i + M_M \rightarrow X_M + M_i \quad (8)$$

$$A_i + X_X \rightarrow A_X + X_i \quad (9)$$

$$X_i + A_A \rightarrow X_A + A_i \quad (10)$$

$$A_i + M_M \rightarrow A_M + M_i \quad (11)$$

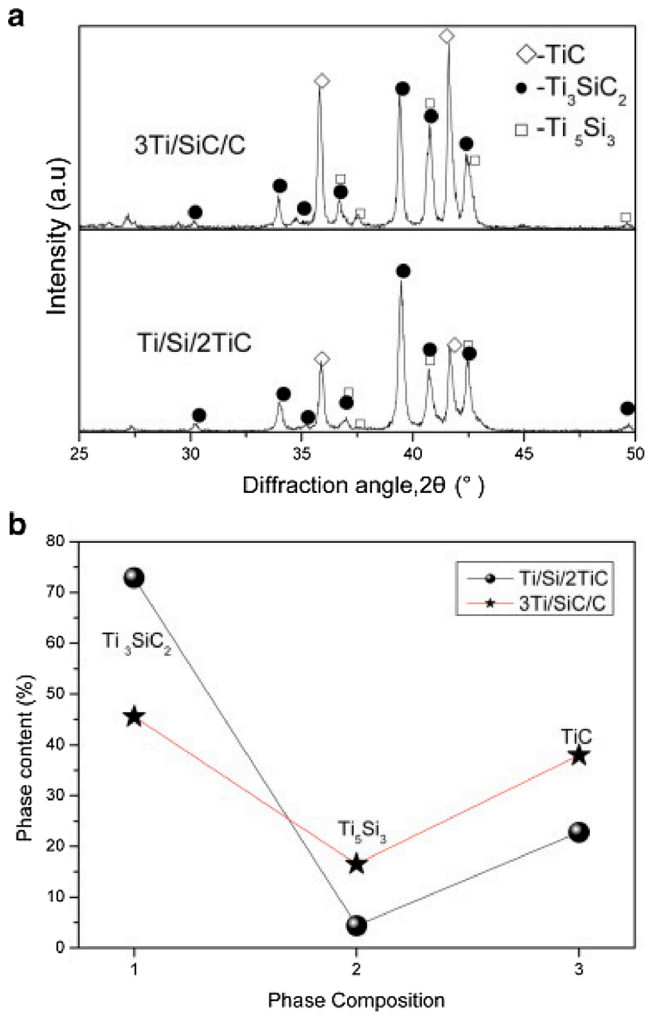

Fig. 7. (a) XRD patterns and (b) phase compositions of the SHS-ed samples prepared using 3Ti:1SiC:1C and 1Ti:1Si:2TiC.
Reproduced with permission from Ref. [26], © 2013 Elsevier Ltd.

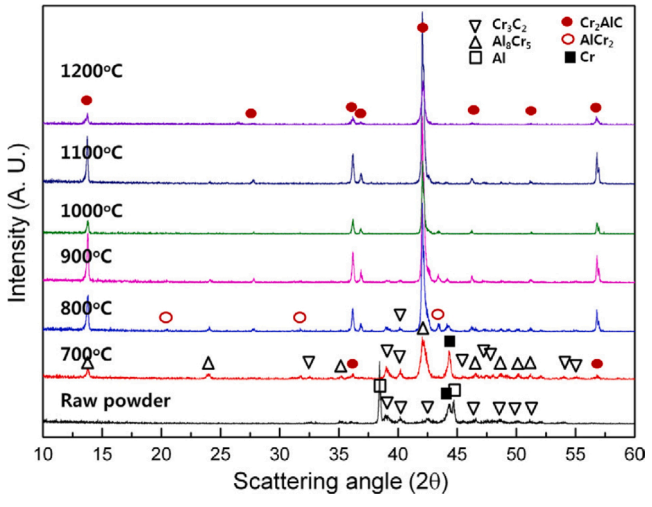

Fig. 8. XRD patters of raw 1Cr:2.4Al:1Cr_3C_2 powders and the SPS-ed samples prepared at different temperatures.
Reproduced with permission from Ref. [27], © 2013 Elsevier B.V.

$$M_i + A_A \rightarrow M_A + A_i \quad (12)$$

Table 1 gives the calculated defect formation energies of FP and anti-site pairs and corresponding reaction energy barriers in Eqs. (1–12) for some typical MAX phases. It should be noted that the reaction energy barrier of one *i-v* recombination is not the formation energy of its corresponding anti-site defect. The formation energy of an anti-site defect includes the energy barriers of all reactions required starting from the defect-free state. For example, the formation energy of the M_X-X_M anti-site pair equals the sum of the formation energies of M_{FP} and X_{FP} and the reaction energy barriers of Eqs. (1) and (2).

The formation energies of defects vary depending on the compositions of MAX phases. Overall, the formation energies of A_{FP} and X_{FP} are lower than that of M_{FP}. Some MAX phases with low magnetic moments of the M element, *e.g.*, Cr-based MAX phases having a magnetic moment of ~0.002 μB per Cr atom, could have a lower formation energy of M_{FP} than A_{FP} compared with other MAX phases [50]. The low formation energy of A_{FP} results from the relatively weak M—A bonds between the $M_{n+1}X_n$ layers and A layers, which is also consistent with the fact that the A atomic layers in MAX phases can be etched out from the layered structure, forming MXene [51–54].

The formation energies of the M_A-A_M anti-site pairs of MAX phases are much lower than those of M_X-X_M and A_X-X_A anti-site pairs, which is in correspondence with the fact that the M—A bonds are relatively weaker than the M—X bonds. Besides, the reaction energy barriers of the *i-v* recombination in Eqs. (5, 6) for all MAX phases are negative, indicating that a vacancy at an A atom lattice position and an interstitial M atom near it, or a vacancy at a M atom lattice position and an interstitial A atom near it, can recombine spontaneously at low temperatures. To some extent, the formation energies of the M_A-A_M anti-site pairs are influenced by the electronegative differences between M and A atoms, as shown in Fig. 10. The formation energy increases with the increase of the electronegative difference, which could provide important guidance on the choice of which type of MAX phase to use in neutron radiation resistant components.

Besides the formation energies of intrinsic point defects, their migration energies, which have not received widespread attention, also influence the *i-v* recombination. The lower the migration energy, the easier the point defect can be annihilated by *i-v* recombination. The lamellar structure of MAX phases makes the migration of point defects along layers much easier than that through layers. The strong M—X bonds in the $M_{n+1}X_n$ layers and the weak M—A bonds between the $M_{n+1}X_n$ layers and A layers also make the $M_{n+1}A$ block act as a defect sink and provide convenient defect migration along or near to the A layers, which has been proven by Middleburgh et al. [56] for Ti_3AlC_2 and Ti_3SiC_2 (Table 2). For Ti_3AlC_2, the migration energy barrier of V_{Ti} along the Ti_{II} atomic layers is 3.11 eV, which is lower than the 4.27 eV for migration along the Ti_I atomic layers (the configurations of Ti_{II} and Ti_I are shown in Fig. 9), because the Ti_{II} atomic layers are near to the Al atomic layers while the Ti_I atomic layers are "sandwiched" by the C atomic layers. The migration energy barriers along the Al atomic layers of V_{Al}, Al_i, Ti_i and C_i, which are located in or near to the Al atomic layers, are 0.61 eV, 0.40 eV, 1.02 eV and 0.55 eV, respectively. For Ti_3SiC_2, the migration energy barriers of V_C along and through layers are 4.13 eV and 4.71 eV, respectively. These defects located in or near to the Si atomic layers, also have lower migration energy barriers than other defects. Similar results have also been obtained by Wang et al. [45] who proved that the Ti_A anti-site defects can migrate *via* a neighboring V_A along the A layers with low energy barriers, which are 0.6 eV and 0.3 eV for Ti_3AlC_2 and Ti_3SiC_2, respectively. One difference between Ti_3AlC_2 and Ti_3SiC_2 is that one of the most preferential sites for C_i is located between the Al atomic layer and Ti_{II} atomic layer in Ti_3AlC_2, while all the preferential sites for C_i are located in the Si atomic layer in Ti_3SiC_2, which makes C_i more easily to migrate and be recombined with V_C for Ti_3AlC_2 and attributes to its better radiation tolerance than Ti_3SiC_2.

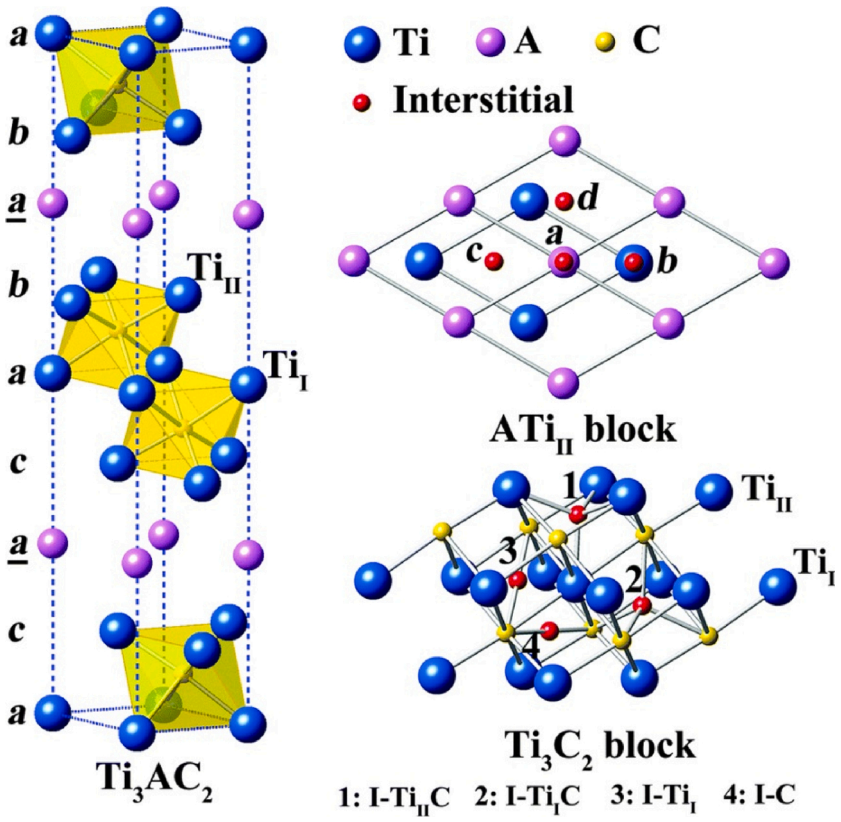

Fig. 9. Schematic diagrams of the crystal structure and initial interstitial positions of Ti_3AC_2.
Reproduced with permission from Ref. [45], © the PCCP Owner Societies 2015.

3.2. Stability of MAX phases with A vacancies

A-related defects usually have relatively low formation energies (Table 1), and migrate easily along the A layers, especially for A_i (Table 2), so the transport of A atoms is relatively fast and this is important for the self-healing behavior of MAX phases when a micro-cracked material is exposed to air or combustion gas residues at high temperatures. Furthermore, the oxidation of A atoms also results in the formation of new A vacancies in MAX phases which travel in the opposite direction as the growth direction of the oxide. The issue of the phase stability in case of a high concentration of A vacancies has not been assessed widely, but plays an important role in setting the self-healing potential of MAX phases.

It has been proven that Ti_3SiC_2 and Ti_3AlC_2 can retain their layered structure after losing some of their Si or Al atoms. Fig. 11 [57] shows the cross-sectional TEM images of a Ti_3SiC_2 film after annealing in vacuum at 1100 °C for 25 h. There is a thin protective layer of TiO_2 (a thickness of 3~4 nm), which has been typically observed on Ti_3SiC_2 films. $TiC_{0.67}$, which was decomposed from Ti_3SiC_2, is between the protective layer and the Ti_3SiC_2 matrix. A residual amount of Si still exists in the form of locally remaining Si layers (white arrowheads) in the $TiC_{0.67}$ layer, indicating that $TiC_{0.67}$ is formed by diffusion and oxidation of Si in the Ti_3SiC_2 matrix. The elemental concentrations from EDX line scan (the dash line corresponds to the interface between the $TiC_{0.67}$ layer and the Ti_3SiC_2 matrix) shows that there is less Si content in the Ti_3SiC_2 area near to the $TiC_{0.67}$ layer, indicating that Ti_3SiC_2 can retain its layered structure after partial loss of Si. Fig. 12 [58] shows the high-resolution TEM (HRTEM) images and EDX spectra of Ti_3AlC_2-Cu composites HP-ed at 950 °C. Al diffused from Ti_3AlC_2 into the Cu, forming the Cu (Al) solid solution and TiC. EDX spectra demonstrate the partial loss of Al in the defective Ti_3AlC_2 after HP, and the HRTEM images prove the structural stability of the defective Ti_3AlC_2.

Calculations by Wang et al. [59] demonstrated that Ti_2AlC can maintain its lamellar structure after losing as many as half of its Al atoms, as shown in Fig. 13. A positive cohesive energy difference ΔE_{coh} between the defective Ti_2Al_xC and its decomposition products (Ti_2C--xAl) means that the defective Ti_2Al_xC is stable relative to Ti_2C and Al, while a negative ΔE_{coh} means that the defective Ti_2Al_xC will decompose into Ti_2C and Al (Fig. 13(a)). Therefore, the defective Ti_2Al_xC with $x >$ 0.5 would not decompose. Fig. 13(b) reflects that the lattice parameters of Ti_2Al_xC change only marginally for $0.5 < x < 1.0$, while the lattice parameter c decreases dramatically with the decrease of x from 0.5 to 0, indicating that the Ti—Al bonds between the Ti_2C layers and Al_x layers are strong enough to maintain the phase stability of Ti_2Al_xC with $x >$ 0.5, while the further loss of Al will result in a rapid structure shrinkage along the c-axis, that is, the collapse of the layered structure of Ti_2AlC.

3.3. Effect of defective properties on radiation tolerance

Due to their unique properties combining those of metals and ceramics, their good high temperature stability and their lower neutron absorption cross-section than refractory metals, MAX phases have been proposed as candidate structural materials for components to be exposed to extreme radiation conditions as in future nuclear reactors [60–63]. Therefore, research on the radiation tolerance of MAX phases is important to screen out ideal MAX phases suitable for this field. Neutron or ion radiation can result in the accumulation of Frenkel defects (vacancies and interstitial atoms) caused by displacement cascades in materials, which would lead to amorphization if materials cannot accommodate these point defects [47,64]. As discussed in Section 3.1, vacancies and interstitial atoms can be annihilated by the *i-v* recombination, which would form anti-site defects if the interstitial atom during the *i-v* recombination is not the same as the original atom at this vacancy. Therefore, the formation of anti-site defects can accommodate significant concentrations of point defects, among which the M_A-A_M anti-site pairs have the lowest formation energy, as shown in Table 1,

Table 1
Calculated defect formation energies and reaction energy barriers (eV) of some typical MAX phases.

Researcher	Xiao et al. [20]				Christopoulos et al. [46]			Hadi et al. [55]			Christopoulos et al. [49]			
MAX phase	Cr_2AlC	Cr_2GeC	Ti_2AlC	Ti_2AlN	Ti_3SiC_2	Ti_3GaC_2	Ti_3GeC_2	Ti_3InC_2	Ti_3SnC_2	Zr_3SnC_2	Hf_3SnC_2	V_3AlC_2	Zr_3AlC_2	Ta_3AlC_2	Ti_3AlC_2
M_{FP}	7.05	5.70	7.57	7.21	7.30	7.43	7.82	9.71	9.40	8.74	9.20	7.40	6.12	7.43	7.32
A_{FP}	7.26	6.84	3.67	5.42	3.19	3.31	4.95	7.23	9.41	6.48	7.29	6.31	1.46	5.84	3.40
X_{FP}	3.14	3.23	4.01	3.56	3.09	4.27	4.38	5.15	5.50	4.97	5.31	2.73	3.47	2.87	3.17
M_X-X_M	7.53	6.44	11.78	11.71	13.44	11.76	12.82	12.97	12.13	14.92	15.10	9.80	10.60	17.36	10.52
A_X-X_A	8.86	5.71	9.41	10.57	6.28	8.24	7.05	11.14	10.18	10.09	10.63	9.36	8.43	10.67	9.26
M_A-A_M	2.40	4.04	2.96	2.52	4.65	5.03	5.80	5.33	5.38	5.15	5.21	2.71	3.46	3.85	3.27
$M_i + V_X \rightarrow M_X$					3.45	1.51	1.77	−0.05	−1.02	1.79	0.72	−0.63	0.86	5.72	0.51
$X_i + V_M \rightarrow X_M$					−0.41	−1.45	−1.14	−1.84	−1.75	−0.58	−0.13	−1.15	0.14	1.35	−0.48
$A_i + V_X \rightarrow A_X$					−0.06	1.41	−1.83	−1.14	−4.65	−1.67	−2.10	0.12	3.04	1.39	2.39
$X_i + V_A \rightarrow X_A$					0.06	−0.75	−0.45	−0.10	−0.07	0.31	0.12	0.21	0.46	0.58	0.31
$A_i + V_M \rightarrow A_M$					−3.15	−2.94	−3.09	−6.39	−7.36	−4.44	−4.86	−5.38	−2.39	−4.44	−4.20
$M_i + V_A \rightarrow M_A$					−2.69	−2.78	−3.88	−5.22	−6.07	−5.63	−6.42	−5.62	−1.72	−4.97	−3.25
$M_i + X_X \rightarrow M_X + X_i$					6.54	5.78	6.15	5.10	4.48	6.76	6.04	2.10	4.33	8.58	3.68
$X_i + M_M \rightarrow X_M + M_i$					6.89	5.98	6.68	7.87	7.65	8.16	9.07	7.70	6.26	8.78	6.84
$A_i + X_X \rightarrow A_X + X_i$					3.03	5.68	2.55	4.01	0.85	3.30	3.22	2.85	6.51	4.25	5.55
$X_i + A_A \rightarrow X_A + A_i$					3.25	2.56	4.50	7.13	9.34	6.79	7.41	6.51	1.92	6.42	3.71
$A_i + M_M \rightarrow A_M + M_i$					4.16	4.49	4.73	3.32	2.04	4.30	4.33	2.03	3.73	2.99	3.12
$M_i + A_A \rightarrow M_A + A_i$					0.50	0.54	1.07	2.01	3.34	0.85	0.88	0.68	−0.27	0.87	0.15

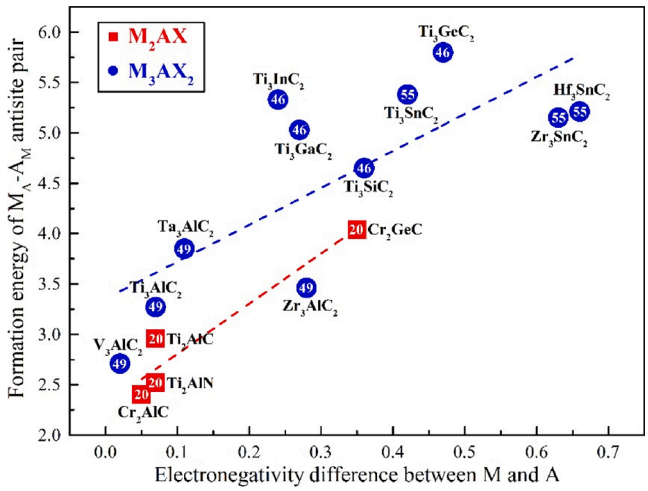

Fig. 10. The relationship between the formation energies of the M_A-A_M anti-site pairs and the electronegative differences (from the periodic table of electronegativity by Pauling scale) between M and A atoms of some typical MAX phases. (Reference numbers are shown in the circles or squares).

Table 2
Calculated migration energy barriers (eV) of intrinsic point defects in Ti_3AlC_2 and Ti_3SiC_2.

	V_{Ti}	V_C	V_A	A_i	Ti_i	C_i	Ti_A
Ti_3AlC_2	3.11[a] (Ti_{II}) 4.27[a] (Ti_I)	3.50[b]	0.61[a] 0.90[b]	0.40[a]	1.02[a]	0.55[a] 1.00[b]	0.60[b]
Ti_3SiC_2	3.51[a] (Ti_{II})	4.13[a], 3.60[b] (//) 4.71[a] (⊥)	0.61[a] 0.90[b]	0.02[a]	0.99[a]	0.45[a] 1.40[b]	0.30[b]

[a]Ref [56]; [b]Ref [45]; //: migration along layers; ⊥: migration through layers; Energy barriers without notes indicate migration along layers.

making the formation of the M_A-A_M anti-site pairs an effective way to annihilate point defects.

As TiC and TiN ceramics both possess a high radiation tolerance, it is reasonable to speculate that $Ti_{n+1}AC_n$ and $Ti_{n+1}AN_n$, which have similar Ti—C and TiN— bonds to those in TiC and TiN, could also have a good radiation tolerance [65,66]. Therefore, out of all MAX phases, $Ti_{n+1}AC_n$ and $Ti_{n+1}AN_n$ are the most studied ones for their radiation tolerance. It has been observed that Ti_3AlC_2 possesses a better structural stability than Ti_3SiC_2 under radiation, as shown in Fig. 14(a–l) [67]. The lamellar structure of Ti_3AlC_2 is well maintained upon radiation leading to 10 displacements per atom (dpa) at room temperature, while the nano-lamellar structure of Ti_3SiC_2 is heavily damaged. As indicated by the white arrows in Fig. 14(e, k), for both Ti_3AlC_2 and Ti_3SiC_2, the (000l) ($l = 8n$) diffraction spots get stronger while the ($\bar{1}$10l) ($l = 8n$ and $8n \pm 1$) diffraction spots get weaker upon radiation leading to 5 dpa, which is attributed to the increase of symmetry caused by the phase transformation from α-Ti_3AC_2 to β-Ti_3AC_2 (A = Al or Si) leading to a change in the stacking sequence of ABABACAC in α-Ti_3AC_2 to a sequence of ABCBACBC in β-Ti_3AC_2. However, the simulated electron diffraction pattern of traditional β-Ti_3AlC_2 (Fig. 14(m)) is still not in agreement with the observed pattern (Fig. 14(e)) due to the formation of Ti_{Al}-Al_{Ti} anti-site defects which lead to the mixture of the Ti atomic layers and Al atomic layers and the rearrangement of C atoms. The simulated electron diffraction pattern of modified β-Ti_3AlC_2 after mixing Ti and Al atoms and rearranging C atoms (Fig. 14(n)) is well consistent with the observed pattern. For Ti_3SiC_2, dislocation loops and stacking faults are observed upon radiation leading to 5 dpa (Fig. 14(h)), and a further increase of dpa results in the formation of nanodomains with different stacking

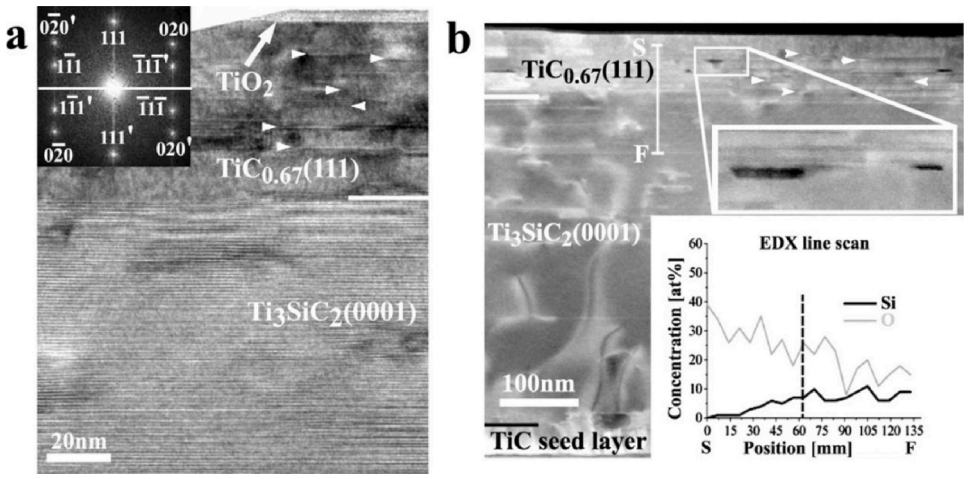

Fig. 11. Cross-sectional TEM images of a Ti_3SiC_2 film after annealing in vacuum at 1100 °C for 25 h: (a) TEM image with a fast Fourier transformation (FFT) from $TiC_{0.67}$; (b) Scanning TEM image with the elemental concentrations from EDX line scan along S-F.
Reproduced with permission from Ref. [57], © 2006 Acta Materialia Inc. Published by Elsevier Ltd.

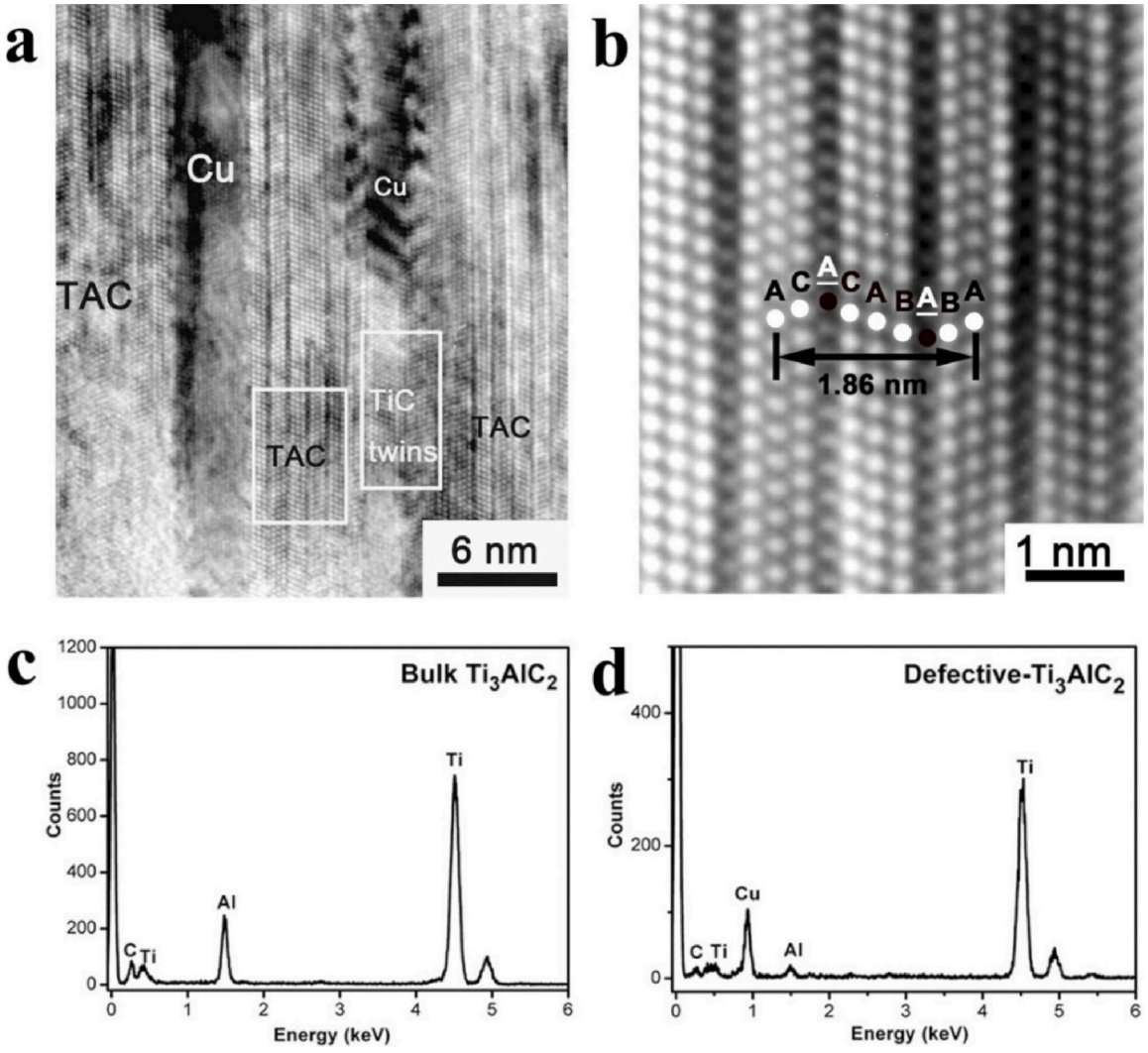

Fig. 12. HRTEM images and EDX spectra of HP-ed Ti_3AlC_2-Cu composites: (a) HRTEM image contains Ti_3AlC_2, Cu and TiC; (b) HRTEM image of the defective Ti_3AlC_2 after losing partial Al; (c) EDX spectrum of the bulk Ti_3AlC_2; (d) EDX spectrum of the defective Ti_3AlC_2.
Reproduced with permission from Ref. [58], © 2007 Acta Materialia Inc. Published by Elsevier Ltd.

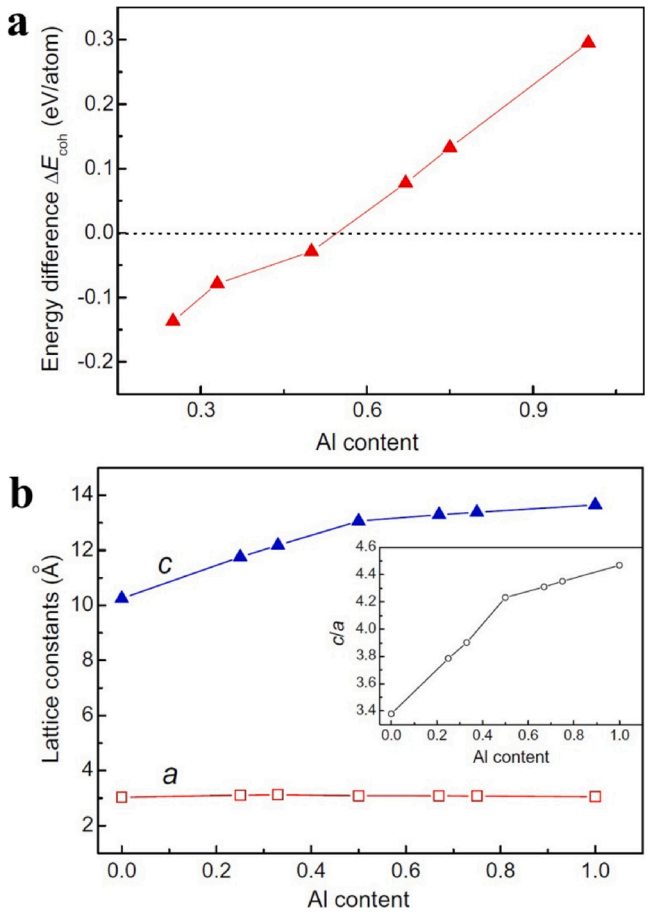

Fig. 13. Dependence of (a) cohesive energy difference ΔE_{coh} between the defective Ti_2Al_xC and Ti_2C-xAl, and (b) lattice constants c, a and c/a on Al content.
Reproduced with permission from Ref. [59], © 2007 Acta Materialia Inc. Published by Elsevier Ltd. on behalf of Acta Materialia Inc.

sequences (Fig. 14(i)). The arc-shaped diffraction spots also indicate the presence of polygonization (Fig. 14(l)). Fig. 14(o) shows a possible formation process of nanograins with different stacking sequences during radiation, where a symmetry plane B is removed by displacement collision, followed by the lamellar collapse along the c-axis and the movement of one of the two face-to-face C planes, forming two fcc-structured stacking sequences (ABCABC and CBACBA) having a twinning relationship. Such fcc-structured stacking sequences with a twinning relationship has also been found in Ti_3AlC_2 where they expanded to form nanotwins [68,69]. Fig. 14(p) shows the simulated electron diffraction pattern of a {111} twinned fcc structure, which is inconsistent with Fig. 14(l), indicating that nanotwins with the fcc structure in Ti_3SiC_2 can be formed upon radiation leading to 10 dpa. The growth of twinned stacking sequences with the fcc structure can form nanotwins with either regular, coherent twin boundaries (CTB) or irregular, incoherent twin boundaries (ITB), in which the CTB can be either a cation layer (Ti and Al/Si) or an anion layer (C), as shown in Fig. 14(q–s). The nanotwins with the fcc structure can also be formed in radiated Ti_2AlC and Ti_2AlN [70,71]. Unlike the formation process of nanotwins in M_3AX_2, nanotwins in M_2AX are formed by inserting an extra B plane into the γ-M_2AX with a stacking sequence of ABCACB.

The nanotwins in Ti_3AlC_2 can maintain crystalline order upon radiation by Au ions leading to 150 dpa, showing an excellent radiation tolerance [69]. For Ti_3SiC_2, radiation by Xe ions leading to 25~30 dpa could lead to amorphization [72]. The difference between the structural stability of Ti_3AlC_2 and Ti_3SiC_2 probably results from the difference in their A-X interaction. There is a remarkable overlap between C 2p and Si 3p states in Ti_3SiC_2, while such a strong overlap is not observed in in Ti_3AlC_2. The weak Al-C interaction in Ti_3AlC_2 benefits the i-v recombination, giving it a high structural stability under radiation. In contrast, the strong overlap between Si-C states in Ti_3SiC_2 increases the possibility of forming amorphous SiC on a nanoscale, as the calculated Si—C bond length with the introduction of point defects in Ti_3SiC_2 is 0.188 nm, which is consistent with the Si—C bond length in amorphous SiC [20, 73]. Besides, the lower formation energy of the Ti_{Al}-Al_{Ti} anti-site defect than the Ti_{Si}-Al_{Si} anti-site defect (Table 1) also gives Ti_3AlC_2 a better Frenkel defect annihilation ability by i-v recombination.

Although the crystalline structure of Ti_3AlC_2 is more stable than Ti_3SiC_2 under radiation, under low temperature radiation cracks form more easily in Ti_3AlC_2 bulk materials, which is probably due to its more significantly anisotropic lattice swelling caused by an accumulation of point defects and a higher β-phase content. The lattice swelling of Ti_3SiC_2 under low temperature radiation is not that significant, which always leads to good anti-cracking under low or high temperature radiation (Fig. 15(a, b)). For Ti_3AlC_2, high temperatures can accelerate the i-v recombination process, preventing the lattice swelling and crack initiation (Fig. 15(c, d)) [67]. The crack initiation due to anisotropic lattice swelling at low radiation temperatures has also been observed in Ti_2AlC [62].

The lattice swelling caused by point defects under radiation at different temperatures is also reflected in the change of hardness values. Hardening after low temperature (400 °C) radiation by Ni ions leading to 10 dpa has been observed in Ti_3AlC_2, Ti_2AlC and Ti_3SiC_2, among which the hardening effect in Ti_3AlC_2 is the most significant (1.9 times of that before radiation). Due to the spontaneous annihilation of point defects, the radiation hardening caused by high temperature (700 °C) radiation leading to the same dpa is much weaker [62]. The hardening can also be undone by high temperature annealing after low temperature radiation [74]. The hardening after low temperature radiation has also been observed in some MAX phase solid solutions such as $Ti_3Si_{0.9}Al_{0.1}C_2$, $Ti_3Si_{0.95}Al_{0.05}C_2$ and $(Ti_{0.95}Zr_{0.05})_3Si_{0.9}Al_{0.1}C_2$ [75].

In conclusion, the defect population in MAX phases determines their phase stability in some harsh external environments, among which the formation processes of intrinsic point defects have been widely studied and confirmed to have an important effect on their self-healing performance and radiation tolerance. Defect migration and phase stability of defective MAX phases need to be further studied. Generally, defects are more easily formed in the $M_{n+1}A$ block and migrate along the A layers, making the $M_{n+1}A$ block perform as a defect sink where defect formation, migration and recombination occur, and inducing disorder accommodation and defect recovery.

4. Solid solutions

Different MAX phases, having the same structure but a difference in one of the three components can possess significantly different properties. For example, the electrical conductivities of hot isostatic pressed Hf_2SnC and Hf_2PbC bulk samples are 2.2×10^6 (Ω m^{-1} and 13.4×10^6 (Ω m^{-1}, respectively [76]; the thermal conductivities at room temperature of HP-ed Ta_4AlC_3 and Nb_4AlC_3 are 38.4 W/(m K and 13.5 W/(m K, respectively, and their Vickers hardnesses are 5.1 GPa and 2.6 GPa, respectively [77,78]. Adjusting the compositions of MAX phases to create solid solutions could be a possible method to tailor their properties to meet specific requirements.

Interestingly, for some MAX phase solid solutions, solid solutions with a quite high solid solubility can be obtained, while it is impossible to synthesize their pure parent phases. For example, $(V_{0.5}Cr_{0.5})_3AlC_2$ was successfully synthesized by reactive HP from elemental powders, while Cr_3AlC_2 has never been experimentally reported [79]. Similarly, Mn has been used as an alloying element for the M-site atoms in Cr_2AlC, forming $(Cr_{1-x}Mn_x)_2AlC$ to tailor its magnetic properties, although Mn_2AlC does not exist [80,81]. In this section, the ordered or disordered structures of M alloyed $M_{n+1}AX_n$ phases are presented, and the

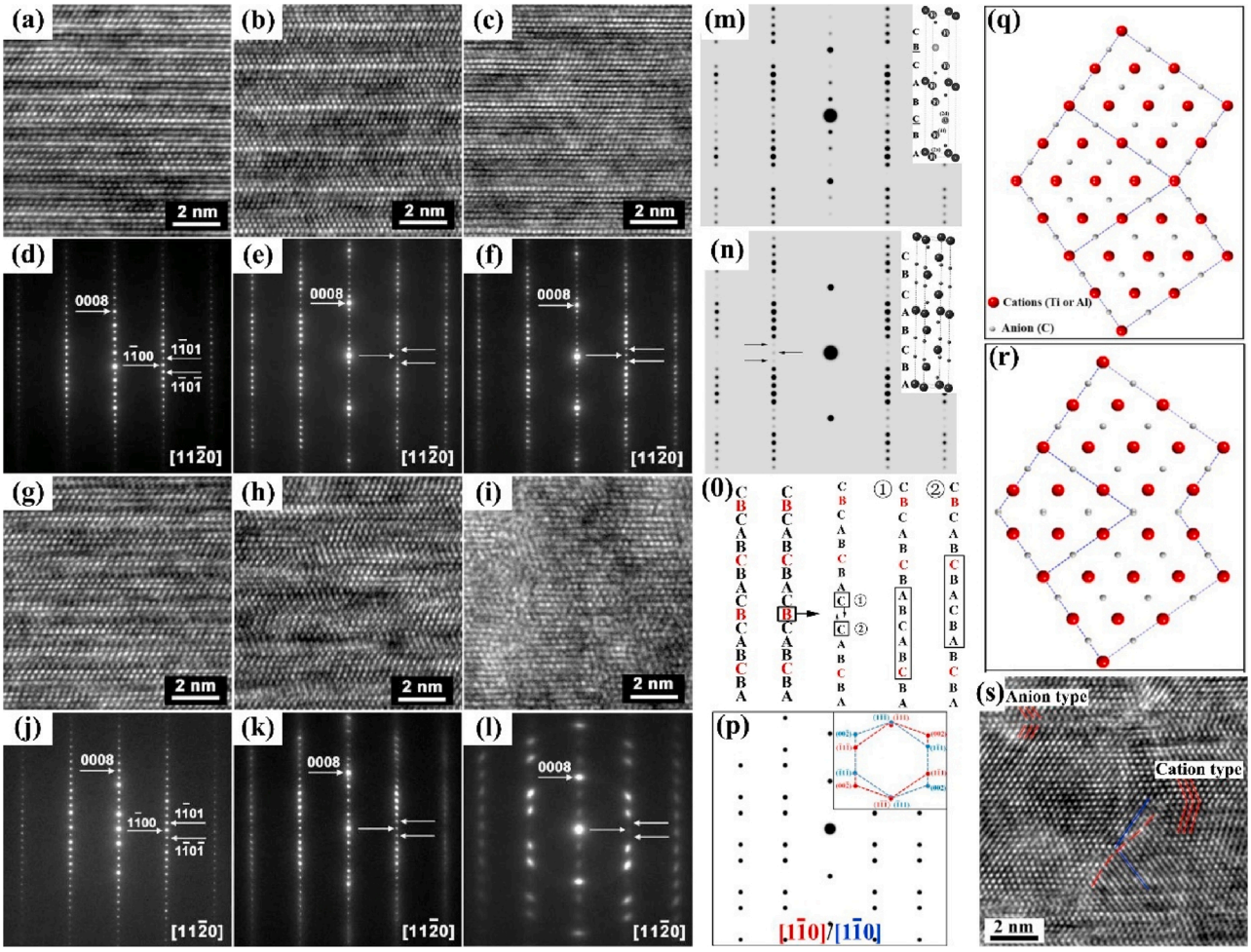

Fig. 14. Characterization of radiated Ti_3AlC_2 and Ti_3SiC_2: (a~c) HRTEM images of Ti_3AlC_2 radiated by Xe ions at room temperature leading to dpa values of (a) 0, (b) 5, and (c) 10, respectively; (d~f) corresponding selected-area electron diffraction (SAED) patterns of (a~c); (g~i) HRTEM images of Ti_3SiC_2 radiated at room temperature leading to dpa values of (g) 0, (h) 5, and (i) 10, respectively; (j~l) corresponding SAED patterns of (g~i); (m) and (n) simulated electron diffraction patterns of traditional and modified β-Ti_3AlC_2, respectively; (o) schematic diagram of a possible formation process of nanograins with two different stacking sequences with a twinning relationship; (p) simulated electron diffraction pattern of {111} twinned fcc structure; (q) and (r) two types of CTB in twinned fcc-structured $(TiAl_{0.33})C_{0.66}$ with a cation layer and an anion layer as twin boundaries, respectively; (s) HRTEM image shows an irregular ITB (red dash line) and two types of CTB in radiated Ti_3AlC_2.

(a~l): Reproduced with permission from Ref. [67], © 2015 Elsevier B.V.; (m~o): Reproduced with permission from Ref. [68], © 2013 Acta Materialia Inc. Published by Elsevier Ltd.; (p~s): Reproduced with permission from Ref. [69], © Elsevier Ltd on behalf of Acta Materialia Inc (For interpretation of the references to colour in this figure legend, the reader is referred to the web version of this article).

properties of MAX phase solid solutions are discussed.

4.1. Occupied positions of alloying M atoms

M alloyed $M_{n+1}AX_n$ phases being the most widely studied MAX phase solid solutions system, possess more than one type of Wyckoff positions of M atoms when $n > 1$. For M_3AX_2, the Wyckoff positions of M atoms in one M_3X_2 block include one inner 2*a* (0, 0, 0) positions and two outer 4*f* (1/3, 2/3, *z*) position. For M_3AX_2, the Wyckoff positions of M atoms in one M_4X_3 block include two inner 4*f* (1/3, 2/3, *z*) positions and two outer 4*e* (0, 0, *z*) positions. Thus, the alloying M atoms could orderly occupy some Wyckoff positions.

In 2014, Liu et al. [82] reported two new MAX phase solid solutions, $(Cr_{2/3}Ti_{1/3})_3AlC_2$ and $(Cr_{5/8}Ti_{3/8})_4AlC_3$ prepared by hot pressing elemental powders, and speculated that it could be possible to synthesize $(Cr_{2/3}Ti_{1/3})_3AlC_2$ where Cr and Ti atoms occupy 4*f* and 2*a* Wyckoff positions, respectively. Soon after, Liu et al. [83] synthesized the first M-ordered MAX phase solid solution, $(Cr_{2/3}Ti_{1/3})_3AlC_2$ by heating mixed 1TiC:1Cr_2AlC powders at 1500 °C for 30 min under flowing Ar. They proved that Ti atoms occupy 2*a* Wyckoff positions, which are sandwiched by 4*f* Wyckoff positions occupied by Cr atoms as deduced *via* combined ND and XRD Rietveld refinement methods. They speculated that such an ordered structure could be formed by the insertion of a single TiC layer into the Cr_2AlC unit cell. Caspi et al. [84] synthesized M-ordered $(Cr_{0.5}V_{0.5})_{n+1}AlC_n$ by heating mixed 0.5(*n*+1)Cr:0.5(*n*+1)V:1.1Al:*n*C elemental powders. This is the first reported M-ordered MAX phase solid solution synthesized from mixed elemental powders. By ND Rietveld refinement, it was proved that for $n = 1$, Cr and V atoms are completely disordered; for $n = 2$, 2*a* positions are fully occupied by V atoms and 4*f* positions are occupied by Cr atoms and remaining V atoms; for $n = 3$, V and Cr atoms occupy 84 % and 16 % of 4*f* positions, respectively, and remaining V and Cr atoms occupy 32 % and 68 % of 4*e* positions, respectively (not fully ordered but somehow mixed).

Anasori et al. [85] firstly observed such M-ordered structure in Mo_2TiAlC_2 prepared by heating mixed 2Mo:1Ti:1.1Al:2C elemental powders at 1600 °C for 4 h under flowing Ar, as shown in Fig. 16, where Ti and Mo atoms occupy 2*a* and 4*f* Wyckoff positions, respectively. Then they synthesized M-ordered $Mo_2Ti_2AlC_3$ using mixed 2Mo:2Ti:1.1Al:2.7C elemental powders [86]. The formation enthalpies of M-ordered Mo_2TiAlC_2 and $Mo_2Ti_2AlC_3$ at 0 K were calculated to be

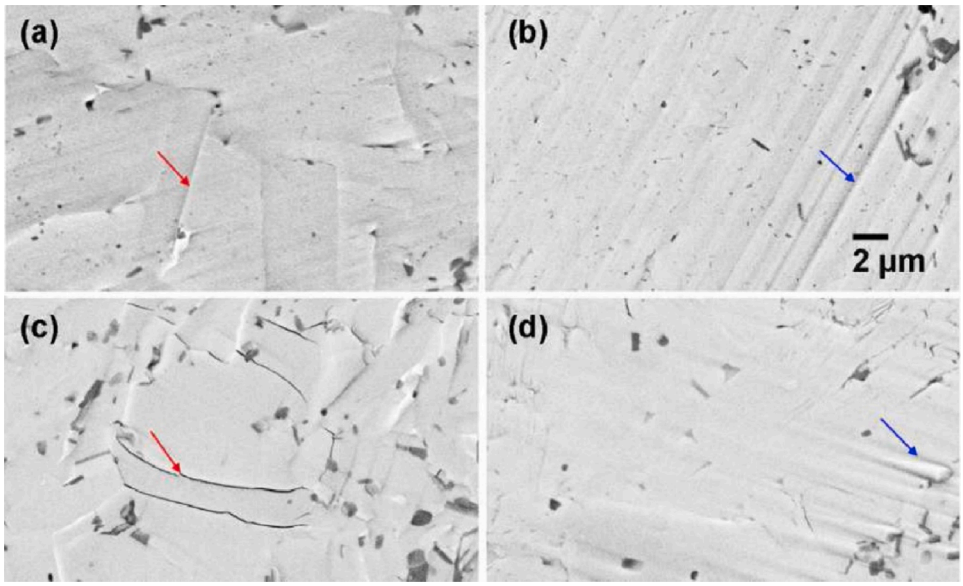

Fig. 15. Surface morphologies of Ti_3SiC_2 and Ti_3AlC_2 bulk samples radiated by Xe ions leading to 5 dpa at different temperatures: (a) Ti_3SiC_2 radiated at room temperature; (b) Ti_3SiC_2 radiated at 600 °C; (c) Ti_3AlC_2 radiated at room temperature; (d) Ti_3AlC_2 radiated at 600 °C. (Red arrows indicate cracks; blue arrows indicate polishing scratches) (For interpretation of the references to colour in this figure legend, the reader is referred to the web version of this article).
Reproduced with permission from Ref. [67], © 2015 Elsevier B.V.

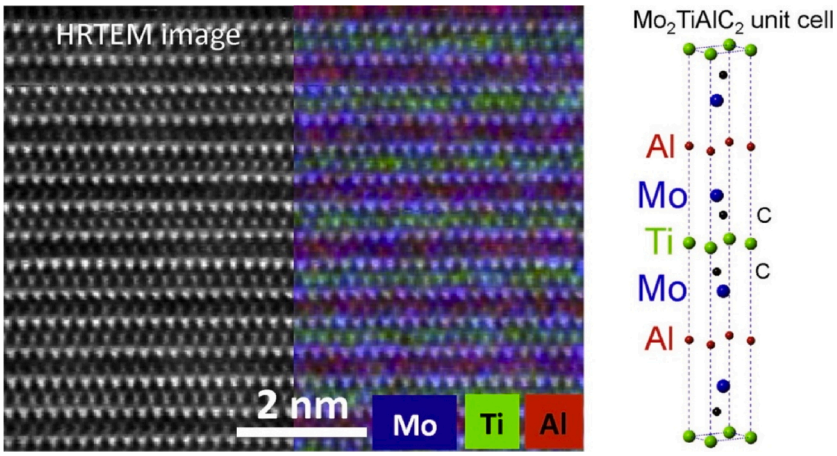

Fig. 16. HRTEM image, high-resolution EDX map and schematic diagram of the crystal structure of Mo_2TiAlC_2.
Reproduced with permission from Ref. [85], © 2015 Acta Materialia Inc. Published by Elsevier Ltd. on behalf of Acta Materialia Inc.

−18 meV/atom and −17 meV/atom, respectively, while those of Mo_3AlC_2 and Mo_4AlC_3 are both positive. Compared with Mo_2TiAlC_2 in which 2*a* Wyckoff positions are fully occupied by Ti atoms, the order degree of $Mo_2Ti_2AlC_3$ in which 14 % of 4*f* Wyckoff positions are occupied by Mo atoms is a little lower. This phenomenon is the similar to the research of Caspi et al. [84], and indicates that the higher configurational entropy of $M_{n+1}AX_n$ phases with higher *n* values stabilizes their disordered structures to some extent.

Meshkian *et al.* [87] synthesized M-ordered Mo_2ScAlC_2 in which the Sc atomic layers are sandwiched by the Mo atomic layers and calculated its formation enthalpy to be −24 meV/atom, although its parent phases Mo_3AlC_2 and Sc_3AlC_2 are both dynamically unstable. They also prepared the first Sc-containing MXene with a sandwiched structure by selective etching of Al.

Dahlqvist et al. [88] calculated the formation enthalpies of ordered and disordered $(M, Ti)_{n+1}AlC_n$, where M = Zr, Hf (group IV); V, Ta, Nb (group V); Cr, Mo, W (group VI). For TiM_2AlC_2, the M-ordered structure where the Ti atomic layers are sandwiched by the M atomic layers is thermodynamically stable for all M atoms from group IV and V. For $Ti_2M_2AlC_3$, the sandwiched structure is thermodynamically stable for M = Nb, Mo, W. At higher temperatures, an order-disorder transformation temperature $T_{disorder}$ was predicted taking configurational entropy into account. For M_2TiAlC_2 (M = Cr, Mo, W) and $M_2Ti_2AlC_3$ (M = Mo, W), $T_{disorder} > 1773$ K, which is higher than the usual temperature for the synthesis of bulk MAX phases, thus they can be prepared with ordered structures where M atoms preferentially occupy the outer 4*f* (for M_2TiAlC_2) or 4*e* (for $M_2Ti_2AlC_3$) Wyckoff positions which are near to the Al layers. The stability of these ordered structures was attributed to the presence of the Ti atomic layers which break the energetically unfavorable stacking of M and C and a larger electronegativity of M than Al. More recently, Dahlqvist et al. [89] did a theoretical screening of the phase stability for M-ordered or disordered M_3AlC_2 and M_4AlC_3 phase solid solutions, where M comes from groups III to VI (Sc, Y, Ti, Zr, Hf, V, Nb, Ta, Cr, Mo, W). They found that the M atomic layer near to the Al layer that does not form a rock-salt MC structure, a small size difference between the two M elements and a large electronegativity difference between Al and the M element near to Al are favorable for the formation of M-ordered MAX phase solid solutions. Based on these criteria, they predicted 7 M-ordered and 38 disordered MAX phase solid solutions.

As these M-ordered $M_{n+1}AX_n$ ($n > 2$) phase solid solutions mentioned above all have an out-of-plane ordered structure where different M atoms orderly occupy different Wyckoff positions located at different layers, they are also called *o*-MAX phases [90]. For M_2AX, there is only one type of Wyckoff positions, 4*f* (2/3, 1/3, 1/12), of M atoms, thus it is

much more difficult to synthesize M_2AX phases with the out-of-plane ordered structure. Dahlqvist et al. [88] calculated the formation enthalpies and $T_{disorder}$ for ordered and disordered TiMAlC (M = Zr, Hf, V, Nb, Ta, Cr, Mo and W), and found that only TiVAlC, TiNbAlC and TiTaAlC have a thermodynamically stable ordered structure with Ti and M atomic layers alternatively appearing along the *c*-axis at 0 K. However, for all of them, $T_{disorder} < 650$ K, which means that these materials cannot be prepared under the usual synthesis temperature of bulk MAX phases. Ingason et al. [91] predicted from theory that the out-of-plane ordered $(Cr_{0.75}Mn_{0.25})_2GeC$ with one Mn_2GeC unit existing after every three Cr_2GeC units can only be prepared at a temperature lower than 600 K, and they prepared a $(Cr_{0.75}Mn_{0.25})_2GeC$ film with a disordered occupation by UHV magnetron sputtering at a deposition temperature of 600 °C. HRTEM observations (Fig. 17) show that Cr and Mn atoms are completely mixed in the $M_{n+1}X_n$ layers and Ge atoms occupy the A layers. Dahlqvist et al. [92] calculated the formation enthalpy of $(Cr_{1-x}Mn_x)_2AlC$ by *ab initio* calculations and found that the out-of-plane ordered $(Cr_{1-x}Mn_x)_2AlC$ with the Mn_2AlC and Cr_2AlC units alternatively stacked is thermodynamically stable at 0 K. However, it has been proven by Mockute et al. [93] *via ab initio* calculations that $(Cr_{1-x}Mn_x)_2AlC$ with a disordered occupation is thermodynamically stable after synthesized at a temperature higher than 600 K when taking the configurational entropy into account. They also successfully prepared a $(Cr_{0.84}Mn_{0.16})_2AlC$ film with Cr and Mn completely intermixed by magnetron sputtering at 600 °C.

Although no experimentally produced out-of-plane ordered M_2AX phase solid solutions has been reported, M_2AX phase solid solutions with in-plane order, which are called "*i*-MAX phases", have attracted much attention since Tao et al. [94] synthesized the first *i*-MAX phase $(Mo_{2/3}Sc_{1/3})_2AlC$ by heating stoichiometric mixed elemental powders at 1500 °C for 20 h under flowing Ar and prepared $Mo_{1.33}C$ MXene with d i-v acancy ordering by selectively etching Al and Sc atoms in 2017. The $(Mo_{2/3}Sc_{1/3})_2AlC$ crystallized in the monoclinic *C2/c* structure, which is the first synthesized MAX phase not belonging to the hexagonal

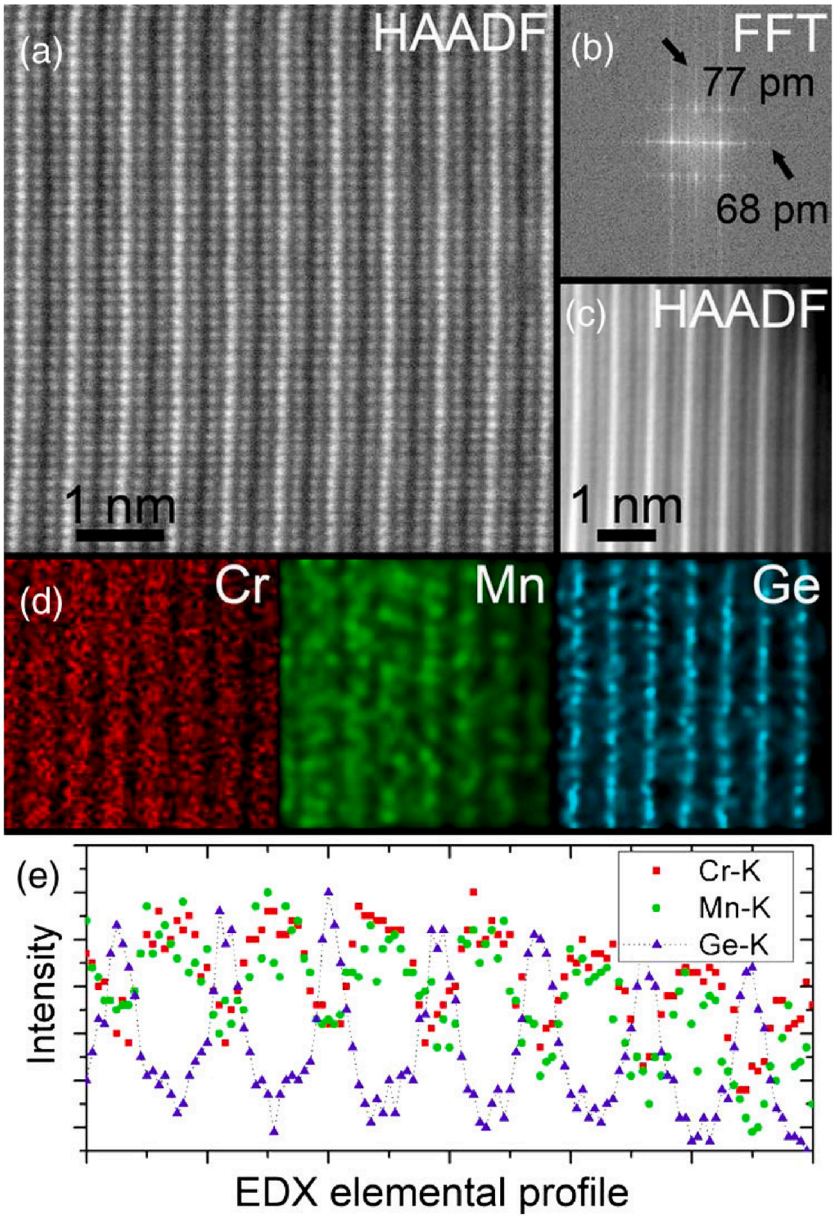

Fig. 17. TEM analysis of $(Cr_{0.75}Mn_{0.25})_2GeC$: (a) high-resolution scanning TEM image; (b) FFT from (a); (c) an area from (a); (d) high resolution EDX maps corresponding to (c); (e) elemental concentrations from EDX line scan across layers in (c).
Reproduced with permission from Ref. [91] https://doi.org/10.1103/PhysRevLett.110.195502, © 2013 American Physical Society.

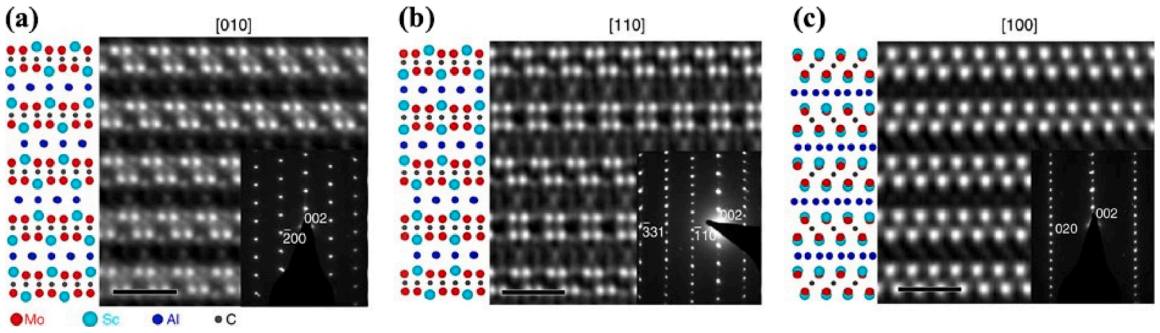

Fig. 18. STEM images, SAED patterns and schematic diagram of the crystal structure of $(Mo_{2/3}Sc_{1/3})_2AlC$ along different directions: (a) [010]; (b) [110]; (c) [100]. Reproduced with permission from Ref. [94], © 2017 The Author(s).

P6₃/mmc structure. Fig. 18 shows the STEM images, SAED patterns and schematic diagram of the crystal structure of $(Mo_{2/3}Sc_{1/3})_2AlC$ along different directions. In the M atomic layers, the Sc atoms are located at the centers of the Mo atomic hexagons and extend out of the M atomic layers to Al layers to some extent. It has been proven that the Al atoms are arranged on a Kagomé-like lattice, which deviates slightly from the ideal Kagomé lattice, in many synthesized *i*-MAX phases such as $(V_{2/3}Zr_{1/3})_2AlC$, $(Mo_{2/3}Y_{1/3})_2AlC$ and $(Mo_{2/3}Sc_{1/3})_2AlC$ in the *C2/c* structure, and $(Mo_{2/3}Sc_{1/3})_2GaC$ and $(Mo_{2/3}Y_{1/3})_2GaC$ in the *Cmcm* structure [95,96].

Tao et al. [97] discovered a class of rare-earth containing *i*-MAX phases, $(Mo_{2/3}RE_{1/3})_2AlC$ (RE = Ce, Pr, Nd, Sm, Gd, Tb, Dy, Ho, Er, Tm, and Lu). Most of $(Mo_{2/3}RE_{1/3})_2AlC$ (RE = Tb, Nd, Gd, Dy, Ho, Er, and Tm) crystallized in the monoclinic *C2/c* structure; $(Mo_{2/3}Ce_{1/3})_2AlC$ and $(Mo_{2/3}Pr_{1/3})_2AlC$ crystallized in the monoclinic *C2/m* structure; $(Mo_{2/3}Sm_{1/3})_2AlC$ crystallized in both the monoclinic *C2/m* and *C2/c* structures; $(Mo_{2/3}Gd_{1/3})_2AlC$ crystallized in both the orthorhombic *Cmcm* and the monoclinic *C2/c* structures, as shown in Fig. 19.

Dahlqvist et al. [96] calculated the formation enthalpies and $T_{disorder}$ of 12 *i*-MAX phases, $(Mo_{2/3}M^2_{1/3})_2AC$ (M^2 = Sc, Y and A = Al, Ga, In, Si, Ge, In) in the *C2/c* and *Cmcm* structures, among which 7 phases (M^2 = Sc, A = Al, Ga and M^2 = Y, A = Al, Ga, In) were predicted to be thermodynamically stable at 0 K and 5 phases (M^2 = Sc, A = Al, Ga, In, Sn and M^2 = Y, A = Al, Ga, In) could retain the in-plane ordered structure up to 1773 K. They synthesized $(Mo_{2/3}Sc_{1/3})_2GaC$ and $(Mo_{2/3}Y_{1/3})_2GaC$ in the *Cmcm* structure by solid-state reaction from elemental powders. Based on their theoretical analysis results, it was predicted that a bigger size difference between the two M metals, a smaller size of the A element and fewer electrons populating antibonding orbitals are favorable for the formation of *i*-MAX phases.

During the past three years, the family of *i*-MAX phases has expanded rapidly. Other experimentally reported *i*-MAX phases include $(Cr_{2/3}Zr_{1/3})_2AlC$ [98], $(W_{2/3}Sc_{1/3})_2AlC$ and $(W_{2/3}Y_{1/3})_2AlC$ [99], $(Cr_{2/3}Sc_{1/3})_2AlC$ and $(Cr_{2/3}Y_{1/3})_2AlC$ [100], $(Cr_{2/3}Sc_{1/3})_2GaC$ and $(Mn_{2/3}Sc_{1/3})_2GaC$ [101], $(Mo_{2/3}RE_{1/3})_2GaC$ (RE = Gd, Tb, Dy, Ho, Er, Tm, Yb, and Lu) [102], $(V_{2/3}Sc_{1/3})_2AlC$ [103], *etc*. The discovery of such a huge family of *i*-MAX phases provides a method to tailor the structure and properties of MXenes [104,105].

4.2. Properties of MAX phase solid solutions

MAX phase solid solutions have been widely studied to improve their mechanical properties by solid solution strengthening and hardening. Physical properties such as the thermal expansion, electrical conductivity, and magnetic properties of MAX phases can also be tailored by creating solid solutions. Table 3 lists the lattice parameters and mechanical and physical properties of some typical Ti-based MAX phase solid solutions.

(1) Mechanical properties

Compressive strength, flexural strength and Vickers hardness can be improved by solid solution strengthening and hardening. The strengthening effect seems to be more significant for MAX phases with larger grain sizes, which has been proven by Gao et al. [109] who studied the mechanical properties of reactive sintered $Ti_3Al_{1-x}Si_xC_2$ bulk samples with and without heat-treatment. The grain size of the as-sintered $Ti_3Al_{1-x}Si_xC_2$ samples is around 7 μm (12.5 μm for x = 0.2), while that of the heat-treated samples is around 25 μm, as shown in Table 3. Compared with the highest values of Ti_3AlC_2 and Ti_3SiC_2, the compressive strengths of the $Ti_3Al_{1-x}Si_xC_2$ solid solutions increase 7.4 % (x = 0.4) and 30.2 % (x = 0.6) for the as-sintered and heat-treated

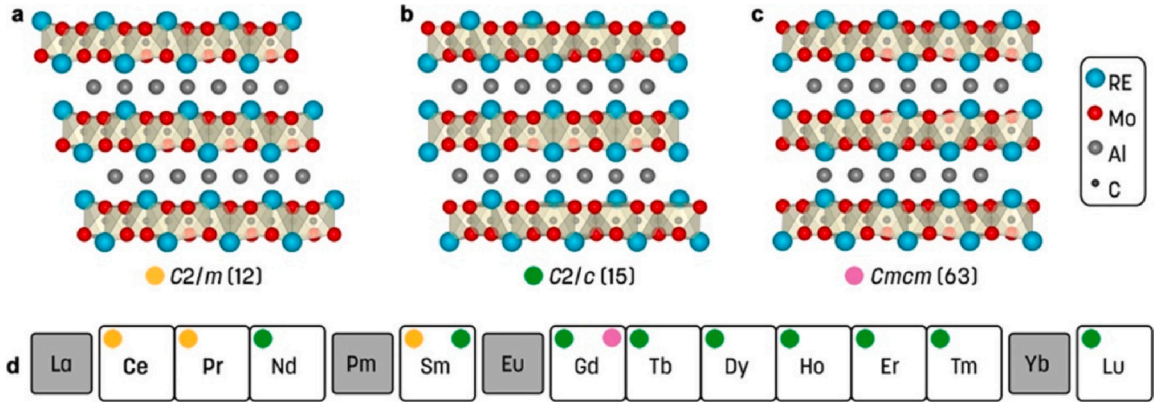

Fig. 19. Schematic diagrams of the crystal structure of *i*-MAX phases $(Mo_{2/3}RE_{1/3})_2AlC$ crystallizing in different structures: (a) monoclinic *C2/m*; (b) monoclinic *C2/c*; (c) orthorhombic *Cmcm*.
Reproduced with permission from Ref. [97] https://doi.org/10.1021/acs.chemmater.8b05298, © 2019 American Chemical Society.

Table 3
Lattice parameters and properties of some typical Ti-based MAX phase solid solutions.

Material		Lattice parameters (nm)		Compressive strength (or flexural strength) (MPa)		Vickers hardness$_{10N}$ (GPa)		CTE (10^{-6} K^{-1})		Electrical conductivity$_{25°C}$ (10^6·Ω^{-1} m^{-1})
		a	*c*							
	$x = 0$	0.3051	1.362	261_{fle}		3.5				
	$x = 0.05$	0.3049	1.361	325_{fle}		3.9				
$(Ti_{1-x}V_x)_2AlC$ [106]	$x = 0.10$	0.3039	1.358	345_{fle}	(40 μm)	4.0	(40 μm)			
	$x = 0.15$	0.3031	1.355	350_{fle}		4.2				
	$x = 0.20$	0.3022	1.353	356_{fle}		4.5				
$(Ti_{1-x}V_x)_2AlC$ [107]	$x = 1$	0.2914	1.313	263_{fle}	(49 μm)	3.4	(49 μm)			
	$x = 0$	0.3072	1.854	671_{com}, 360_{fle}		3.1				2.83
	$x = 0.05$	0.3073	1.850	783_{com}, 362_{fle}		3.2				2.75
$Ti_3Al_{1-x}Si_xC_2$ [108]	$x = 0.10$	0.3073	1.846	816_{com}, 369_{fle}	(20 μm)	3.3	(20 μm)			2.73
	$x = 0.15$	0.3073	1.842	809_{com}, 405_{fle}		3.7				2.72
	$x = 0.20$	0.3070	1.837	895_{com}, 408_{fle}		3.8				2.70
	$x = 0.25$	0.3069	1.832	911_{com}, 409_{fle}		3.9				2.69
	$x = 0$	0.3072	1.854	1309_{com} (7 μm) 835_{com} (25 μm)		4.1 (7 μm) 4.1 (25 μm)		7.66 (25 °C)		
	$x = 0.2$	0.3071	1.829	1012_{com} (12.5 μm)		4.8 (12.5 μm)				
	$x = 0.4$	0.3070	1.808	1406_{com} (7 μm) 1052_{com} (25 μm)		5.0 (7 μm) 5.2 (25 μm)		7.54 (25 °C)		
$Ti_3Al_{1-x}Si_xC_2$ [109]	$x = 0.6$	0.3070	1.788	1312_{com} (7 μm) 1087_{com} (25 μm)		5.6 (7 μm) 5.1 (25 μm)				
	$x = 0.8$	0.3067	1.773	1285_{com} (7 μm)		4.9 (7 μm)				
	$x = 1$	0.3065	1.767	1292_{com} (7 μm) 740_{com} (25 μm)		4.2 (7 μm) 4.1 (25 μm)		7.88 (25 °C)		
	$x = 0$	0.3051	1.364	540_{com} (25 μm)		4.5 (25 μm)		8.2		2.7
$Ti_2AlC_{1-x}N_x$ [110]	$x = 0.5$	0.3021	1.361	810_{com} (25 μm)		5.5 (25 μm)		10.5	(25~1300 °C)	3.1
	$x = 1$	0.2989	1.361	381_{com} (100 μm)		4.0 (100 μm)		8.8		4.0

All the listed Vickers hardnesses were measured under a load of 10 N; flexural strength: $_{fle}$; compressive strength: $_{com}$; the grain size is shown in the bracket next to the strength or hardness; the testing temperature of the coefficient of thermal expansion (CTE) is shown in the bracket next to the CTE.

samples, respectively. The actual hardening effect has only a weak relationship with the grain size, as both the as-sintered and heat-treated samples show an ideal hardening effect around $x = 0.5$. Such solid solution strengthening/hardening phenomena were also observed by experiments or proven by calculation for other MAX phase solid solutions such as $(Ti_{1-x}V_x)_2AlC$ [106], $(Ti_{1-x}Zr_x)_3SiC_2$ [111], $(Cr_{1-x}V_x)_2AlC$ [112], $(Nb_{1-x}Ti_x)_4AlC_3$ [113], *etc*. There are also some MAX phase solid solutions, such as $Ti_3Si_xGe_{1-x}C_2$ [114], $Ti_3Al_xSn_{1-x}C_2$ [115,116], $(Ti_{1-x}Nb_x)_2AlC$ [117], whose mechanical properties are between their end members yet show no solid solution strengthening or hardening effect. Although $Ti_2AlC_{0.5}N_{0.5}$ in Table 3 has higher mechanical properties than both Ti_2AlC and Ti_2AlN, the grain size of Ti_2AlN was much larger than those of Ti_2AlC and $Ti_2AlC_{0.5}N_{0.5}$ [110]. It has been reported that the Vickers hardness of the HP-ed Ti_2AlN bulk samples using SHS-ed Ti_2AlN powders with a size of 17 μm reaches 5.8 GPa [118]. The SPS-ed Ti_2AlN bulk samples with a grain size of 5~10 μm has a Vickers hardness higher than 6 GPa [119]. Therefore, the higher mechanical properties of $Ti_2AlC_{0.5}N_{0.5}$ than its end members in the work of Barsoum et al. [110] should be attributed to more valence electrons in a N atom than in a C atom and the larger grain size of the Ti_2AlN sample, but not the solid solution strengthening/hardening effect.

As solid solution strengthening/hardening is attributed to the lattice distortion caused by alloying atoms, it is reasonable to speculate that whether solid solution strengthening/hardening works or not depends on the degree of lattice distortion caused by alloying atoms. Therefore, we define the change rates of lattice parameters *a* and *c* (a_{CR} and c_{CR}) with the change of the content of alloying atoms in MAX phase solid solutions, which are calculated according to Eq. (13):

$$l_{CR} = \left| \frac{l_{x_2} - l_{x_1}}{\min(l_{x_2},\ l_{x_1}) \times (x_2 - x_1)} \right| \tag{13}$$

where *l* is the lattice parameter *a* or *c*; x_1 and x_2 are two different content values with the changing of the content of the alloying atoms in the solid solutions; l_x is the lattice parameter corresponding to a specific content *x* of the alloying atoms.

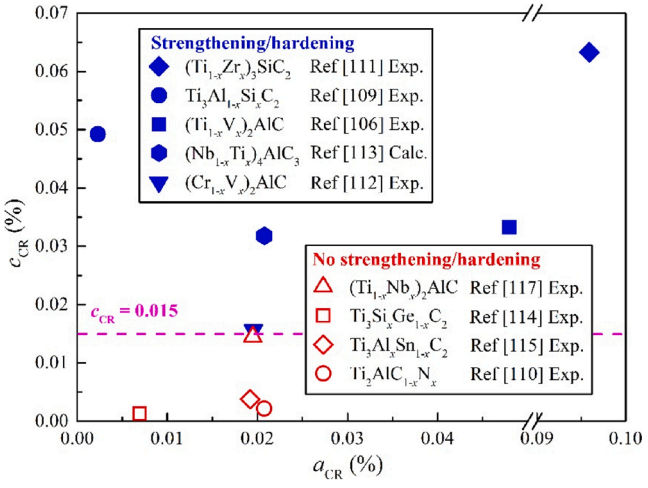

Fig. 20. a_{CR} and c_{CR} in MAX phase solid solutions with or without solid solution strengthening/hardening. (Exp. means data comes from experiments, Calc. means data comes from theoretical calculations).

Fig. 20 shows a_{CR} and c_{CR} values either obtained from the lattice parameters of synthesized MAX phase solid solutions or theoretical calculations. These solid solutions are either proven by experiments or speculated by calculation to be with or without solid solution strengthening/hardening. These a_{CR} and c_{CR} values in Fig. 20 were obtained from two solid solutions with the largest difference in the content of the alloying atoms in corresponding references. Obviously, solid solutions with higher c_{CR} values ($c_{CR} > 0.015$) are more likely to show solid solution strengthening/hardening. As MAX phases have a layered structure, and the attractive force between layers is relatively weak, a higher c_{CR}, which means a more significant lattice distortion through layers, would probably result in a higher deformation resistance along layers. Although this speculation needs further experimental

verification, the hypothesis might guide the readers to select suitable alloying elements to improve mechanical properties of MAX phases by solid solution strengthening/hardening.

The high temperature strength of MAX phases can also be improved by alloying. By replacing 5% of Ti atoms with Zr atoms, the flexural strength at 1200 °C of $(Ti_{0.95}Zr_{0.05})_3Si_{0.95}Al_{0.05}C_2$ can be kept up to 331 MPa, which is 74 % of its strength at room temperature (447 MPa). While the flexural strength at 1100 °C of $Ti_3Si_{0.95}Al_{0.05}C_2$ already decreases to 245 MPa, although its strength at room temperature (475 MPa) is a little higher than $(Ti_{0.95}Zr_{0.05})_3Si_{0.95}Al_{0.05}C_2$ [120].

(2) Thermal expansion

Just as for the mechanical properties, no simple linear relationship exists for the coefficients of thermal expansion (CTEs) of MAX phase solid solutions and their end members. CTEs reflect the average bonding strength in materials. The CTE of $Ti_2AlC_{0.5}N_{0.5}$ in the temperature range between 25~1300 °C is higher than both Ti_2AlC and Ti_2AlN, as shown in Table 3, indicating that $Ti_2AlC_{0.5}N_{0.5}$ has weaker bonds than its two end members [110]. Similar results have been obtained for $Ti_3Si_{1-x}Ge_xC_2$ and $(Ti_{1-x}Nb_x)_2AlC$. The CTE between 50~1200 °C of $Ti_3Si_{0.5}Ge_{0.5}C_2$ (9.3×10^{-6} K^{-1}) is slightly higher than those of Ti_3SiC_2 (8.9×10^{-6} K^{-1}) and Ti_3GeC_2 (7.8×10^{-6} K^{-1}) [121]. The CTE between 25~1200 °C of $(Ti_{0.5}Nb_{0.5})_2AlC$ is 8.9×10^{-6} K^{-1}, while those of Ti_2AlC and Nb_2AlC are both 8.7×10^{-6} K^{-1} [122].

The CTE of $Ti_3Al_{0.6}Si_{0.4}C_2$ at room temperature was measured to be 7.54×10^{-6} K^{-1}, which is lower than those of Ti_3AlC_2 (7.66×10^{-6} K^{-1}) and Ti_3SiC_2 (7.88×10^{-6} K^{-1}), indicating a higher bonding strength in $Ti_3Al_{0.6}Si_{0.4}C_2$ solid solutions than those in the two end members [109], as reported in Table 3. Similar results have been obtained by Chen et al. [123], who attributed the lower CTE of $Ti_3Al_{1-x}Si_xC_2$ to the occupation of Ti *d*–Si *p* and Ti *d*–Al *p* covalent bonding states by the additional valence electron of Si, which results in the strengthening of the attractive force between layers.

It should be noted that none of above known MAX phase solid solutions with higher CTEs than their end members, $Ti_2AlC_{0.5}N_{0.5}$, $Ti_3Si_{0.5}Ge_{0.5}C_2$ and $(Ti_{0.5}Nb_{0.5})_2AlC$, show solid solution strengthening/hardening, as shown in Fig. 20. On the other hand, $Ti_3Al_{0.6}Si_{0.4}C_2$, which shows solid solution strengthening/hardening, possesses a CTE lower than its two end members. This is reasonable as both the CTE and mechanical properties are related to the average bonding strength.

There is also some research about the thermal expansion along different crystal directions of MAX phase solid solutions. For $Cr_2Al_xGe_{1-x}C$, it was observed by *in situ* XRD that with increasing the Al content from 0 to 1, the CTE along the *a* and *b*-axes (along layers) changed only a little and remained in the range from 13.3×10^{-6} K^{-1} to 14.8×10^{-6} K^{-1}, while the CTE along the *c*-axis (through layers) decreases from 17.2×10^{-6} K^{-1} to 11.7×10^{-6} K^{-1} and is equal to the CTE along the *a* and *b*-axes around $x = 0.75$ [124], which means that $Cr_2Al_xGe_{1-x}C$ solid solutions show different thermal expansion anisotropy with different Al contents. Therefore, the CTEs of $Cr_2Al_xGe_{1-x}C$ bulk materials should be between the two end members, unless there is preferential orientation of grains. For $(Cr_{1-x}Ti_x)_2AlC$, it was calculated that with increasing *x* from 0.167 to 0.667, the CTE along the *a* and *b*-axes increases from 12.6×10^{-6} K^{-1} to 14.7×10^{-6} K^{-1}, while that along the *c*-axis decreases from 9.6×10^{-6} K^{-1} to 8.7×10^{-6} K^{-1} [125]. These results provide groundlevel guidelines for tailoring the thermal expansion properties of MAX phase solid solutions by adjusting the contents of alloying atoms.

(3) Electrical conductivity

The alloying atoms in MAX phase solid solutions usually cause solid solution scattering during electron transport, leading to the decrease of the electrical conductivity. It has been reported that the electrical conductivity at room temperature of $(Ti_{0.5}Nb_{0.5})_2AlC$ is $1.28 \times 10^6 \cdot \Omega^{-1}$ m^{-1}, which is much lower than those of Ti_2AlC ($2.78 \times 10^6 \cdot \Omega^{-1}$ m^{-1}) and Nb_2AlC ($3.57 \times 10^6 \cdot \Omega^{-1}$ m^{-1}) [122]. However, the electrical conductivity of $Ti_2AlC_{0.5}N_{0.5}$ ($3.1 \times 10^6 \cdot \Omega^{-1}$ m^{-1}) is between those of Ti_2AlC ($2.7 \times 10^6 \cdot \Omega^{-1}$ m^{-1}) and Ti_2AlN ($4.0 \times 10^6 \cdot \Omega^{-1}$ m^{-1}) [110]. The same is true for $Ti_3Si_{1-x}Ge_xC_2$, whose electrical conductivities at $x = 0$, 0.25, 0.5 and 1 are $3.94 \times 10^6 \cdot \Omega^{-1}$ m^{-1}, $3,75 \times 10^6 \cdot \Omega^{-1}$ m^{-1}, $3.67 \times 10^6 \cdot \Omega^{-1}$ m^{-1} and $3.60 \times 10^6 \cdot \Omega^{-1}$ m^{-1}, respectively [121]. The change of the electrical conductivity of $Ti_3Al_{1-x}Si_xC_2$ with the change of *x* is also not much, which decreases from $2.83 \times 10^6 \cdot \Omega^{-1}$ m^{-1} to $2.69 \times 10^6 \cdot \Omega^{-1}$ m^{-1} with increasing *x* from 0 to 0.25 [108].

It was reported that the electrical conductivities of polycrystalline Nb_2SC, $Nb_2SC_{0.4}B_{0.6}$ and Nb_2SB samples at room temperature are $0.27 \times 10^6 \cdot \Omega^{-1}$ m^{-1}, $0.22 \times 10^6 \cdot \Omega^{-1}$ m^{-1} and $0.77 \times 10^6 \cdot \Omega^{-1}$ m^{-1}, respectively [126]. Although Nb_2SC has a relatively lower electrical conductivity than most MAX phases, it is one of the nine MAX phases showing superconductivity below critical temperatures [127], and $Nb_2SC_{1-x}B_x$ ($0 \leq x \leq 0.6$) could maintain the superconductivity while the critical temperature decreased from 4.8 K ($x = 0$) to 2.6 K ($x = 0.6$).

It seems that alloying atoms on the M-site (*e.g.*, $(Ti_{0.5}Nb_{0.5})_2AlC$) have a more significant solid solution scattering effect, while alloying atoms on the A-site (*e.g.*, $Ti_3Si_{1-x}Ge_xC_2$, $Ti_3Al_{1-x}Si_xC_2$) or X-site ($Ti_2AlC_{0.5}N_{0.5}$) only lead to weak additional scattering. This is probably related to the fact that the density of states (DOS) at the Fermi level (E_F) of MAX phases is dominated by the *d-d* orbitals of M atoms [128]. It has been proven by Magnuson et al. [7] that for several M_2AX phases (Ti_2AlN, Ti_2AlN, V_2GeC and Cr_2GeC), M_3AX_2 (Ti_3AlC_2, Ti_3SiC_2 and Ti_3GeC_2) and their parent binary phases (TiC, TiN and VC), a high DOS at E_F could lead to a high electrical conductivity. Therefore, it seems reasonable to speculate that alloying atoms on the M-site can result in much more carrier scattering than alloying atoms on other sites. As the *d-d* orbitals of M atoms contribute most to the DOS at E_F which could largely affect the electrical conductivity, the change of M atoms could result in a significant change of their electrical conductivity. For example, the electrical conductivity of M_3SnC_2 (M = Ti, Zr, Hf) increases as the location of the M-element in the periodic table moves down [55]. As a result, the electrical conductivity at room temperature of Cr_2AlC is lower than $1.4 \times 10^6 \cdot \Omega^{-1}$ m^{-1}, while that of V_2AlC reaches $4.0 \times 10^6 \cdot \Omega^{-1}$ m^{-1} [128].

(4) Magnetic properties

Most existing ternary MAX phases do not show magnetic properties, yet there have been some calculations on possible magnetic MAX phases, especially those with Mn as the M element. Mn_2AlC and Mn_2GeC were both calculated to be magnetic in their ground states with magnetic moments of 1.86 μB and 1.80 μB per Mn atom, respectively [81]. In 2013, Ingason et al. [129] was the first to report the ferromagnetic properties of Mn_2GaC obtained from both calculations and experiments. The formation enthalpy of Mn_2GaC was calculated to be −30 meV/atom, which is the only thermodynamically stable phase among $Mn_{n+1}GaC_n$ phases and predicted to display magnetic ordering with two dynamically stable configurations, the ferromagnetic configuration where all Mn atoms have the same spin direction and the antiferromagnetic $[0001]_2^A$ configuration where the Mn atoms in two adjacent Mn_2C blocks have different spin directions. The Mn_2GaC film was prepared by magnetron sputter epitaxy and was measured to show ferromagnetic up to 230 K with a saturation magnetic moment of 0.29 μB per Mn atom, which is much lower than the theoretically calculated local Mn moment of 1.6 μB per atom, indicating that the configuration of the synthesized Mn_2GaC is more complex than that of the ideal ferromagnetic configuration. Therefore, they speculated the magnetic ground state of Mn_2GaC to be practically degenerated between the ferromagnetic and antiferromagnetic $[0001]_2^A$ configurations. Novoselova et al. [130] observed a first order magnetic phase transition at 214 K from AFM at higher temperatures to a non-collinear AFM spin structure at

lower temperatures, with the magnetostriction changing sign at this magnetic phase transition in a Mn_2GaC film prepared by magnetron sputtering. It has been theoretically proven by Dahlqvist et al. [131,132] that the magnetic states and structural parameters of Mn_2GaC can be manipulated through controlling the temperature, the magnetic field or the applied pressure. The temperature and magnetic field dependence of magnetic properties has also been studied for some solid solutions such as $(Cr_{0.5}Mn_{0.5})_2GaC$, $(Mo_{0.5}Mn_{0.5})_2GaC$, $(Cr_{0.5}Mn_{0.5})_2AuC$, *etc* [133, 134], suggesting new pathways for tuning magnetism of MAX phases.

Some magnetic solid solutions based on these ternary MAX phases predicted to be magnetic have also been proven to be synthesizable. Dahlqvist et al. [92] calculated the formation enthalpies and magnetic moments of both ordered and disordered $(Cr_{1-x}Mn_x)_2AlC$ at 0 K by *ab initio* calculation, as shown in Fig. 21(a). The ordered $(Cr_{1-x}Mn_x)_2AlC$ with a stacking sequence of Mn-C-Mn-Al-Cr-C-Cr-Al is thermodynamically stable, and the magnetic moment per M-site atom increases with increasing the Mn content. However, the magnetic state of $(Cr_{1-x}Mn_x)_2AlC$ is influenced by the atomic configuration, as shown in Fig. 21(b). Although the formation enthalpy of $(Cr_{0.5}Mn_{0.5})_2AlC$ in its most thermodynamically stable magnetic state increases with the increase of the disorder degree characterized by the ratio of the number of Cr atoms to the number of Cr plus Mn atoms in the Mn-C-Mn layers, the energy differences between the antiferromagnetic (AFM), double-layer antiferromagnetic (dAFM), disorder local moment (DLM) states and the ferromagnetic (FM) state also increase with the increase of the disorder degree, indicating that the FM state becomes more stable relative to other magnetic states with the intermixture between Cr and Mn atoms. The influence of atomic configurations on the magnetic states was also calculated for $(Cr_{1-x}Mn_x)_2GeC$, as shown in Fig. 21(c). The disordered $(Cr_{1-x}Mn_x)_2GeC$ (alloy) becomes more stable relative to FM Cr_2GeC with increasing the temperature. For $(Cr_{0.75}Mn_{0.25})_2GeC$, the magnetic moment of Cr atoms is significantly influenced by their atomic configurations, ranging from 0 to ±1.5 μB, while that of Mn atoms keeps around ±2 μB with little change. Therefore, it is possible to tailor the magnetic states through controlling the atomic configurations for both $(Cr_{1-x}Mn_x)_2AlC$ and $(Cr_{1-x}Mn_x)_2GeC$.

It has been experimentally proven that alloying Mn atoms at the M-site could introduce magnetic properties into many MAX phase solid solutions such as $(Cr_{0.5}Mn_{0.5})_2GaC$ [135], $(Cr_{1-x}Mn_x)_2GeC$ ($x \leq 0.25$) [80], $(Cr_{0.8}Mn_{0.2})_2AlC$ [136], $(Mo_{0.5}Mn_{0.5})_2GaC$ [133], $(V_{0.96}Mn_{0.04})_2AlC$ [137]. Liu et al. [80] prepared ferromagnetic $(Cr_{1-x}Mn_x)_2GeC$ ($x \leq 0.25$) polycrystalline samples *via* reaction synthesis. Alloying Mn in Cr_2GeC successfully induced ferromagnetic band polarization into the originally spin-unpolarized structure. The Curie temperature T_C and the spontaneous magnetic moment p_s per M-site atom both increase with increasing the Mn content, as shown in Fig. 21 (d). The ratio of p_{eff} (the effective moment in the paramagnetic state) to p_s decreases to a low value with increasing the Mn content, indicating

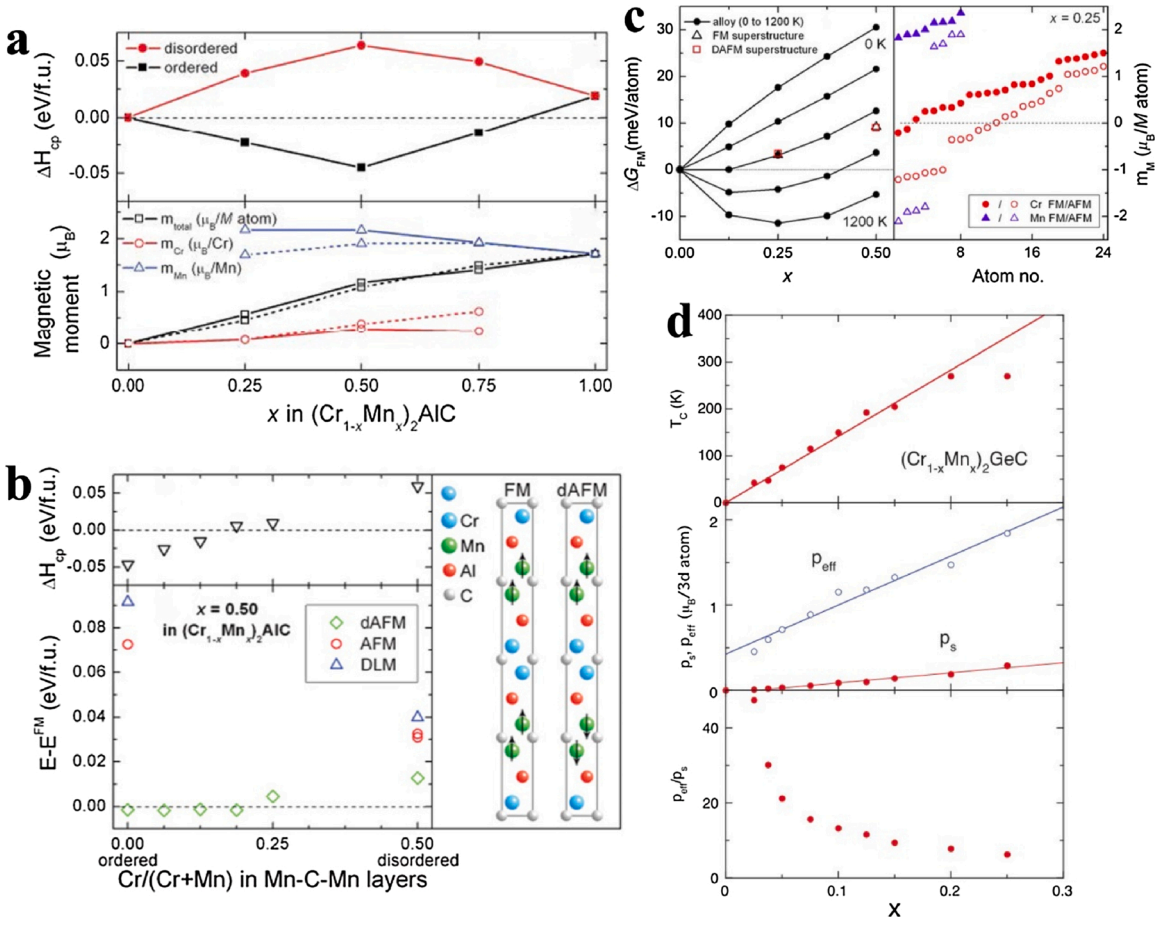

Fig. 21. Magnetic properties of $(Cr_{1-x}Mn_x)_2AlC$ and $(Cr_{1-x}Mn_x)_2GeC$: (a) Formation enthalpies of ordered and disordered FM $(Cr_{1-x}Mn_x)_2AlC$, and the magnetic moments of M-site atoms in ordered (solid lines) and disordered (dash lines) $(Cr_{1-x}Mn_x)_2AlC$; (b) Formation enthalpies and energy differences between other states and the ferromagnetic (FM) state of $(Cr_{0.5}Mn_{0.5})_2AlC$ with the change of the disorder degree; (c) Formation energies of $(Cr_{1-x}Mn_x)_2GeC$ relative to FM Cr_2GeC, and the magnetic moments of M-site atoms in FM and AFM $(Cr_{0.75}Mn_{0.25})_2GeC$ for different configurations; (d) T_C, p_s, p_{eff} and p_{eff}/p_s of $(Cr_{1-x}Mn_x)_2GeC$.
(a, b): Reproduced with permission from Ref. [92], https://doi.org/10.1103/PhysRevB.84.220403, © 2011 American Physical Society; (c): Reproduced with permission from Ref. [91] https://doi.org/10.1103/PhysRevLett.110.195502, © 2013 American Physical Society; (d): Reproduced with permission from Ref. [80], https://doi.org/10.1103/PhysRevB.89.054435, © 2013 American Physical Society.

that the ferromagnetism of $(Cr_{1-x}Mn_x)_2GeC$ is a typical itinerant-electron ferromagnetism. Mockute et al. [136] detected the magnetic response in the $(Cr_{0.8}Mn_{0.2})_2AlC$ film synthesized by cathodic arc deposition up to at least room temperature, verifying the prediction of the antiferromagnetic or ferromagnetic ground state in $(Cr_{0.8}Mn_{0.2})_2AlC$. Although Fe_3AlC_2, which was predicted to show ferromagnetic properties with a magnetic moment of 0.73 μB per Fe atom [138], has been calculated to be thermodynamically unstable [92], $(Cr_{1-x}Fe_x)_2AlC$ ($x \leq 0.017$) has been synthesized by Hamm et al. [139] which shows increasing paramagnetic magnetization with increasing the Fe content.

Recently, Li et al. [140] reported 15 inherently nano-laminated A alloying $V_2(A_xSn_{1-x})C$ phases (A = Fe, Co, Ni, Mn, and combinations thereof, with x ~ 1/3) prepared by an alloy-guided reaction method, which could tailor the magnetic properties by atomic-level control in the processing. The magnetic properties were found to be greatly enhanced for $V_2(Fe_xCo_yNi_zSn_{1-x-y-z})C$ with A layers containing multi-elements.

Related research to date is still focused on the prediction, discovery and determination of the fundamental magnetic properties of MAX phases and their solid solutions. However, the observed tunability of the magnetic properties by controlling the atomic configuration of alloying atoms on the M-site in simulations, by introducing multiple alloying elements on the A-site in experiments, and by controlling the temperature, the magnetic field or the applied pressure in both simulations and experiments, will guide the development of magnetic MAX phases and their solid solutions with promising properties for electronics, spintronics, refrigeration, *etc* [6,91,92,130–134,140].

(5) Oxidation resistance and self-healing

Due to the high diffusion rate of Al along the A layers at high temperatures and the good oxidation resistance of the well-bonded Al_2O_3 scale which forms upon oxidation, the oxidation resistance of some MAX phases can be significantly improved by partially replacing the A atoms with Al [17,109,141]. Fig. 22 shows the SEM analysis results of the oxidation resistance of $Ti_3Si_{1-x}Al_xC_2$ solid solutions. For $Ti_3Si_{0.9}Al_{0.1}C_2$, the oxide scale contains an inner continuous and dense Al_2O_3 layer and an external discontinuous TiO_2 layer after oxidation below 1200 °C for 20 h (Fig. 22(a, b)). Such a structure of the oxide scale indicates that the oxidation of Ti is realized by the out-diffusion of Ti, while the oxidation of Al is realized by the in-diffusion of oxygen to the interface between the oxide layer and the MAX phase matrix and the out-diffusion of Al atoms from the MAX phase matrix to the interface, which has also been proven by Wang et al. [142]. A higher oxidization temperature (1300 °C) triggers the reaction between Al_2O_3 and TiO_2, forming an outside Al_2TiO_5 layer on the dense Al_2O_3 layer (Fig. 22(c)). A further increase of

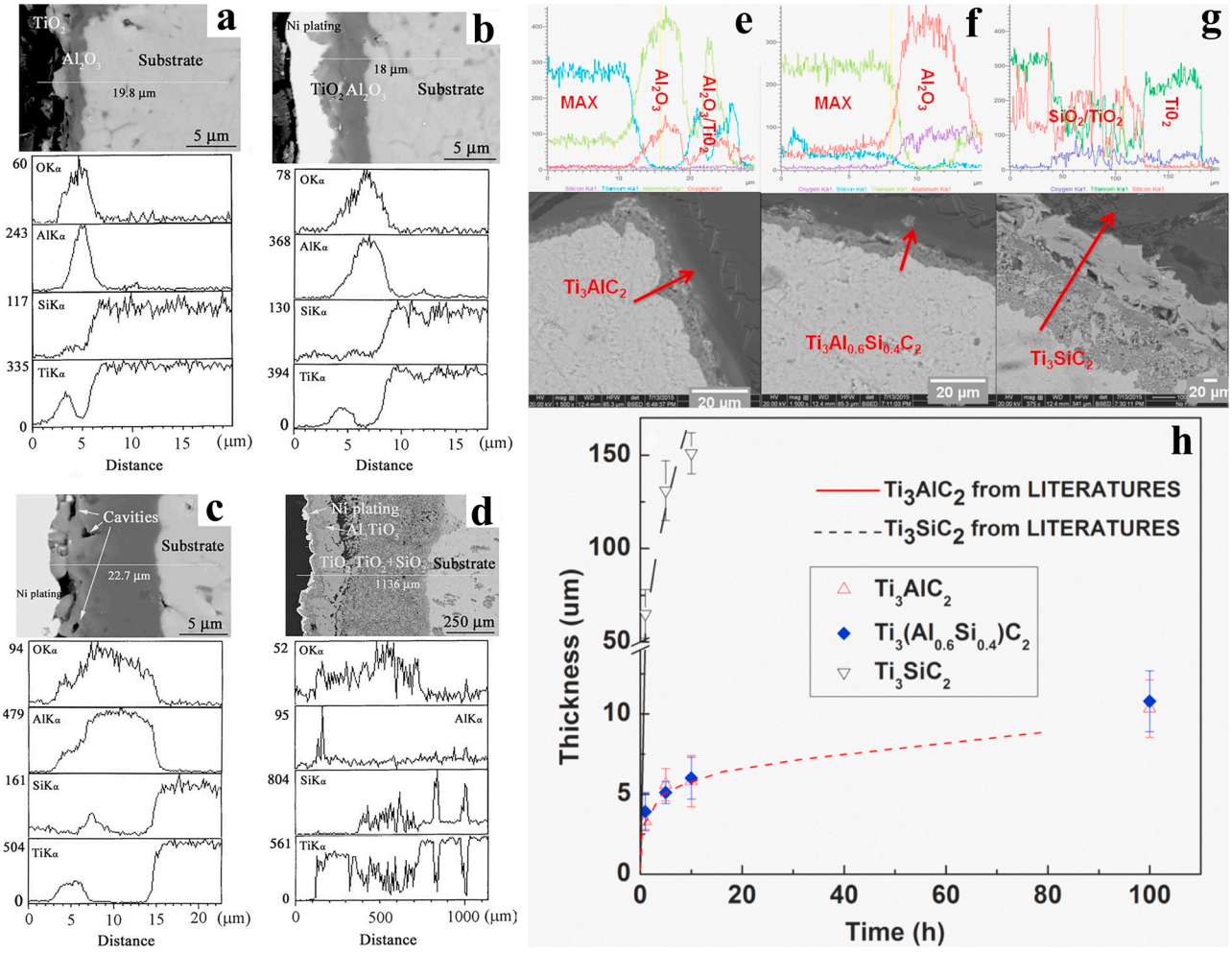

Fig. 22. SEM analysis results of the oxidation resistance of $Ti_3Si_{1-x}Al_xC_2$ solid solutions: (a~d) back-scattered electron SEM images with the elemental concentrations from EDX line scan along the white lines of cross-section for $Ti_3Si_{0.9}Al_{0.1}C_2$ oxidized at 1100 °C, 1200 °C, 1300 °C and 1350 °C for 20 h, respectively; (e~g) back-scattered electron SEM images with the elemental concentrations from EDX line scan along the red arrows of cross-section for Ti_3AlC_2,$Ti_3Si_{0.4}Al_{0.6}C_2$, and Ti_3SiC_2 oxidized at 1200 °C for 10 h, respectively; (h) Oxide layer thickness *vs.* oxidation time at 1200 °C of Ti_3AlC_2,$Ti_3Si_{0.4}Al_{0.6}C_2$, and Ti_3SiC_2.
(a~d): Reproduced with permission from Ref. [141], © 2004 Acta Materialia Inc. Published by Elsevier Ltd.; (e~h): Reproduced with permission from Ref. [109], © 2016 Elsevier B.V (For interpretation of the references to colour in this figure legend, the reader is referred to the web version of this article).

the oxidization temperature (1350 °C) leads to a depletion of the Al_2O_3 formed from only 10 at.% Al in the $Ti_3Si_{0.9}Al_{0.1}C_2$ matrix, leading to the quick in-diffusion of oxygen and oxidization of Si, forming a loose oxide layer which cannot resist further oxidation (Fig. 22(d)). By comparing the oxide compositions and thicknesses of Ti_3AlC_2, $Ti_3Si_{0.4}Al_{0.6}C_2$, and Ti_3SiC_2 (Fig. 22(e–h)), it is concluded that the dense Al_2O_3 layer, which does not exist in the Ti_3SiC_2 sample, effectively prevents the further oxidization of the MAX phase matrix and gives $Ti_3Si_{0.4}Al_{0.6}C_2$ an oxidation resistance comparable to Ti_3AlC_2. Besides, the outside oxide layer of Ti_3AlC_2 is composed of TiO_2 and Al_2O_3, while that of Ti_3SiC_2 is only composed of TiO_2, indicating that the atomic mobility for the Si sublattice is relatively low, which has also been proven by Barsoum et al. [143].

MAX phases with a good self-healing performance should have a high diffusion rate and preferential oxidation of the A element, a good bonding strength and oxidation resistance of the A oxide formed and an E-modulus and CTE of the oxide formed in the microcracks matching that of the MAX phase matrix [17]. The application of these 6 criteria identified several promising self-healing MAX phases containing Al as the A element. Given the reaction kinetics of Al_2O_3 the healing of such MAX phases has to take place at relatively high temperatures. For example, Cui et al. [144] proved by conventional Differential ThermoGravimetry (DTG) analysis that the formation temperature of Al_2O_3 is above 1000 °C for bulk Ti_2AlC materials. For the non-Al containing Ti_3SiC_2, although Si_i has a lower migration energy barrier than Ti_{Si} along the Si layers, the self-diffusion rate of Si is much lower than that of Ti [17]. Therefore, Ti is easier to diffuse out and be oxidized than the relatively immobile Si, thus the oxide layer on Ti_3SiC_2 is composed of an outside TiO_2 layer formed by the out-diffusion of Ti and an inside porous $TiO_2 + SiO_2$ mixed layer formed by the in-diffusion of oxygen (Fig. 22(g)). Such a porous oxide scale cannot prevent further oxidation of the MAX phase matrix, thus Ti_3SiC_2 is not an ideal self-healing material. Its self-healing performance can be improved somewhat by partially replacing Si with Al due to the faster diffusion and oxidation of Al and a good oxidation resistance of Al_2O_3. The oxidation temperature of Al in Ti_2AlC could be lowered to 900 °C by partially replacing Al with Sn, as reported by Bei et al. [145]. SnO_2 itself can be formed at temperatures below 600 °C in $Ti_2Al_{1-x}Sn_xC$, which could give $Ti_2Al_{1-x}Sn_xC$ an attractive crack filling potential at lower temperatures. However, due to the poor bond strength and the poor mechanical strength of the SnO_2 the recovery of the mechanical strength would only be modest.

5. Texture and anisotropy

MAX phases belong to the hexagonal crystal system and possess a lamellar crystal structure. Therefore, like other materials belonging to the hexagonal crystal system [146–150], it is possible to fabricate textured bulk MAX phases composed of plate-like grains with preferential orientation under a favorable external condition (*e.g.*, a uniaxial pressure or a magnetic field). Textured bulk MAX phases have anisotropic properties due to the lamellar crystal structure, which can improve their properties along specific directions and make them applicable to more harsh service environments. In this section, texture formation techniques and anisotropic properties of textured bulk MAX phases are discussed.

5.1. Texture formation techniques

The most widely used technique to prepare textured bulk MAX phases is pressure-assisted sintering, *e.g.*, HP and SPS. For unknown reasons, direct hot pressing or spark plasma sintering of MAX phases does not result in highly textured microstructures, which is different from other materials belonging to the hexagonal crystal system [21,151,152]. Two methods have been developed to improve the degree of texture of pressure-assisted sintered bulk MAX phases: the first one is performing ball milling treatment to the as-synthesized MAX samples with relatively coarse grains to obtain fine plate-like grains, and then using these ball milled plate-like grains to prepare textured bulk MAX phases by HP or SPS, as shown in Fig. 23(a) [23]; the other is called edge-free SPS (EFSPS), *i.e.*, there is no constraint to the lateral surfaces of the sintered sample, which can provide enough space for plate-like grains to deform and rotate under the applied uniaxial pressure, thus resulting in preferential orientation, as shown in Fig. 23(b) [153]. Fig. 23(c) and (d) shows the morphologies of the side surface parallel to the applied compression direction of textured Ti_2AlC composites prepared by HP using reactive ball milled powders, where plate-like Ti_2AlC grains are oriented with their *c*-axis parallel to the applied compression direction. The reactive ball milling process introduced some oxygen, which reacted with Al in the Ti_2AlC matrix, forming Al_2O_3 (dark particles in Fig. 23(c)).

Most MAX phases are magnetically anisotropic, *i.e.*, their magnetic susceptibilities along different crystallographic directions are different. Therefore, the preparation of so-called 'green bodies' (*i.e.* objects composed of raw powders stuck together and to be used for subsequent sintering) by slip casting or gel-casting in a magnetic field before sintering could be an effective technique to orient MAX phase grains. For MAX phases belonging to the hexagonal crystal system, the anisotropy of the magnetic susceptibilities $\Delta\chi$ is expressed as Eq. (14) [154]:

$$\Delta\chi = \chi_c - \chi_{a,b} \tag{14}$$

where χ_c and $\chi_{a,b}$ are the magnetic susceptibilities along the *c*-axis and *a* and *b*-axes, respectively.

When a MAX phase particle is placed in a magnetic field, this particle tends to rotate, making the crystallographic axis with a higher χ value align parallel to the magnetic field direction. If the driving energy of rotation ΔE is higher than the thermal motion energy U, the particle can be rotated by the magnetic field. ΔE and U are given by Eqs. (15) and (16), respectively [154,155]:

$$\Delta E = |\Delta\chi| V B^2 / 2\mu_0 \tag{15}$$

$$U = 3nN_0k_BT \tag{16}$$

where V is the volume of the particle; B is the magnetic flux density; μ_0 is the permeability in vacuum; n is the mole content of the MAX phase in the particle; N_0 is the Avogadro constant; k_B is the Boltzmann constant; T is the temperature. Ball milling of the synthesized bulk MAX phases before MA is an effective method to further improve the degree of texturing, as the rotation of fine particles in a magnetic field is more easy to achieve than that of coarse particles [156].

Due to the lamellar structure of MAX phases, their degree of texturing can be quantitively characterized by the Lotgering orientation factor f_{00l}, which is calculated according to Eqs. (17) and (18) [157]:

$$f_{00l} = \frac{P - P_0}{1 - P_0} \tag{17}$$

$$P \text{ and } P_0 = \frac{\sum I_{00l}}{\sum I_{hkl}} \tag{18}$$

where $\sum I_{00l}$ and $\sum I_{hkl}$ are the sums of the diffraction peak intensities of all (00*l*) and (*hkl*) crystal planes, respectively. P is calculated from the measured XRD data of the textured sample surfaces, and P_0 is calculated from standard JCPDS cards. For one textured MAX phase bulk sample, a higher f_{00l} for its sample surface perpendicular to the preferential orientation of the *c*-axis (*e.g.*, the surface perpendicular to the pressure direction during SPS) indicates more (00*l*) planes on this surface, *i.e.*, a higher degree of texture.

The magnetic anisotropy is different for different MAX phases. Some MAX phases possess a higher magnetic susceptibility along the *c*-axis (e.g., Nb_4AlC_3 [158]), which will be aligned with the *c*-axis parallel to the magnetic field direction; while some MAX phases (e.g., Ti_3SiC_2 [159])

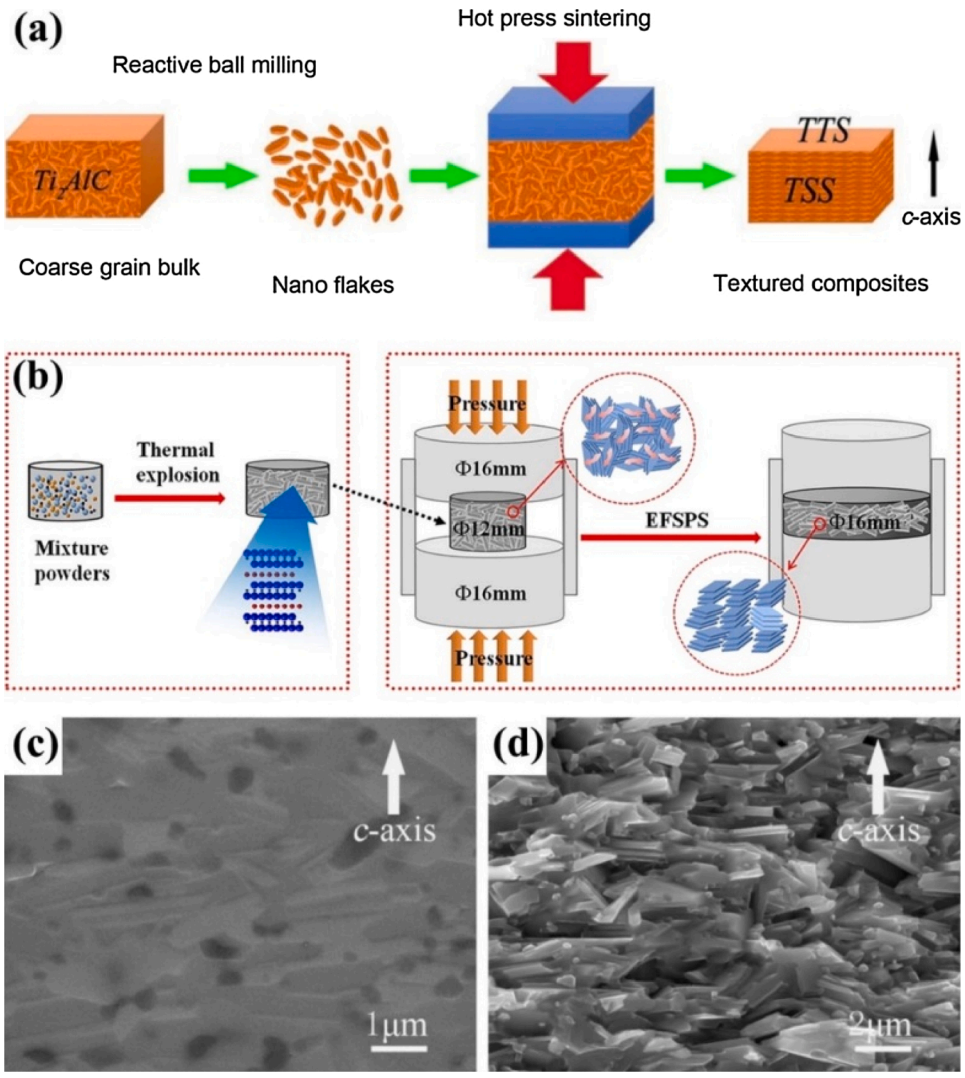

Fig. 23. Preparation processes and morphologies of textured bulk MAX phases: (a) HP using ball milled powders from the as-synthesized sample; (b) EESPS using as-synthesized sample; (c) and (d) polished morphology and fracture morphology of the side surface parallel to the applied compression direction of textured Ti_2AlC composites by the process in (a).
(a, c, d): Reproduced with permission from Ref. [23], © 2020, Elsevier; (b): Reproduced with permission from Ref. [153], © 2017 Acta Materialia Inc. Published by Elsevier Ltd.

possess a higher magnetic susceptibility along the *a* and *b*-axes, resulting in the *c*-axis becoming perpendicular to the magnetic field direction. For these MAX phases with a higher χ_c, all plate-like grains can be oriented well, forming a highly textured microstructure. However, for these MAX phases with a higher $\chi_{a,b}$, the *c*-axis of plate-like grains will be randomly oriented in the plane perpendicular to the magnetic field direction. Applying a rotation to the suspension mold in the magnetic field parallel to the horizon is an effective technique to improve the grain orientation (*i.e.*, orient the *c*-axis of anisometric grains to one direction) for MAX phases and other hexagonal materials with a higher $\chi_{a,b}$ [22,159–161].

MAX phase particles can be magnetically rotated as long as the magnetic field is strong enough. However, as the magnetic susceptibilities of most MAX phases are very low (e.g., the magnetic susceptibility of Ti_3SiC_2 was measured to be 4.1×10^{-6} [162]), a strong magnetic field (usually higher than 10 T) is needed to orient them, greatly restricting the widespread use of this technique.

For HP or SPS, the rotation under the uniaxial pressure can take place when the starting particles have anisometric shapes, yet even then the rotation process during sintering is hindered by the "house of cards" structure composed of plate-like particles, Therefore, MA by slip casting or gel-casting in a magnetic field and then sintering the textured green body can result in a higher degree of texture. Lapauw et al. [163] prepared textured Ti_3SiC_2 bulk samples with a Lotgering factor f_{00l} of 0.52 on the sample surface perpendicular to the applied compression direction by SPS at 1350 °C/30 MPa for 5 min and then edge-free deformed at 1350 °C/70 MPa, while the Ti_3SiC_2 sample prepared by Sato et al. [22] by slip casting in a magnetic field of 12 T and then pressureless sintering (PLS) at 1400 °C for 2 h possesses a higher f_{00l} of 0.97.

The two texturing methods, pressure-assisted sintering (*i.e.*, HP and SPS) and MA, can also be combined to realize the highest degree of texture. For example, Hu et al. [164] prepared textured Nb_4AlC_3 bulk samples with a high Lotgering orientation factor f_{00l} close to 1 by slip casting in a magnetic field of 12 T and subsequent SPS at 1450 °C/30 MPa for 10 min.

5.2. Anisotropic properties

Texturing of MAX phases can improve their properties along specific directions. Different deformation mechanisms and fracture modes along different directions give them anisotropic mechanical properties. The lamellar structure gives them anisotropic thermal conductivity and electrical conductivity. Table 4 lists the anisotropic properties of some typical bulk MAX phases.

(1) Mechanical properties

Grain orientation of MAX phases has a significant influence on their deformation mechanisms. Kink band formation under an external pressure is much easier for plate-like grains parallel to the sample surface [168]. Kink bands are formed by the sideward deflection of the

Table 4
Anisotropic properties of some typical textured bulk MAX phases.

Material	Preparation method	Grain size (μm)	*f*00l on TS	Vickers hardness (GPa)	Flexural strength (MPa)	Fracture toughness (MPa·m$^{1/2}$)	Thermal conductivity (W/(m·K))	Electrical conductivity ($\times 10^6\ \Omega^{-1}\cdot m^{-1}$)
Ti_2AlN [153]	EFSPS	~5	0.80	10.4 (TS, 49 N) 7.9 (SS, 49 N)	–	–	20.5 (// *c*-axis) 32.3 (⊥ *c*-axis)	4.08 (// *c*-axis) 2.47 (⊥ *c*-axis)
Ti_2AlC [23]	HP	~1	0.74	7.9 (TS, 10 N) 6.8 (SS, 10 N)	735 (// *c*-axis) 626 (⊥ *c*-axis)	8.5 (// *c*-axis) 8.2 (⊥ *c*-axis)		
Ti_3AlC_2 [165]	MA & SPS	~5	–	8.1 (TS, 1 N) 9.1 (SS, 1 N) 7.4 (TS, 100 N) 5.8 (SS, 100 N)	1261 (// *c*-axis) 1005 (⊥ *c*-axis)	13.1 (// *c*-axis) 14.6 (⊥ *c*-axis)	14.6 (// *c*-axis) 25.3 (⊥ *c*-axis)	1.01 (// *c*-axis) 0.83 (⊥ *c*-axis)
Ti_3AlC_2 [166]	SPS	~3	0.69	5.9 (TS, 10 N) 7.0 (SS, 10 N)	–	–	–	–
Ti_3SiC_2 [22]	MA & PLS	~5	0.97	–	623 (// *c*-axis)	5.9 (// *c*-axis)	–	–
Ti_3SiC_2 [167]	SPS MA & SPS	~5	0.60 0.96	–	843 (// *c*-axis) 978 (// *c*-axis)	6.6 (// *c*-axis) 7.3 (// *c*-axis)	–	–
Ti_3SiC_2 [159]	MA & SPS	~2	0.95	8.7 (TS, 9.8 N) 7.3 (SS, 9.8 N)	–	–	–	–
Nb_4AlC_3 [164]	MA & SPS	~5	~1	10.4 (TS, 0.245 N) 12.4 (SS, 0.245 N) 7.0 (TS, 49 N) 4.9 (SS, 49 N)	881 (// *c*-axis) 789 (⊥ *c*-axis)	14.1 (// *c*-axis) 9.3 (⊥ *c*-axis)	14.1 (// *c*-axis) 21.1 (⊥ *c*-axis)	0.49 (// *c*-axis) 0.81 (⊥ *c*-axis)

layers with limited constraint for plate-like grains parallel to the sample surface, as shown in Fig. 24(a). Therefore, the elastic recovery for plate-like grains perpendicular to the surface is larger than that parallel to the surface, that is, the energy consumption during the loading-unloading process is higher for plate-like grains parallel to the surface, as shown in Fig. 24(c) and (d). Plastic deformation for plate-like grains perpendicular to the surface is mainly *via* delamination, as shown in Fig. 24(e), where the delamination between plate-like grains occurs from bottom-left to top-right. Plastic deformation for plate-like grains parallel to the surface is mainly *via* kink bind formation, as shown in Fig. 24(f), where much kink band pile-up is observed around the indentation, also indicating that kink band formation is more easily to occur for plate-like grains parallel to the surface. As a result, the nano-indentation hardness for plate-like grains parallel to the surface (4.9 GPa) is lower than that for plate-like grains perpendicular to the surface (7.3 GPa).

Similar to the nano-indentation results for plate-like Ti_3SiC_2 grains with different orientations, The Vickers hardness of textured bulk MAX phases also varies greatly along different directions, as shown in Table 4. The hardness measured under a low load on the sample surface perpendicular to the *c*-axis orientation, which is called the top surface (TS), is normally lower than the hardness measured on the sample surface parallel to the *c*-axis orientation, which is called the side surface (SS) [164–166]. However, a high load can result in a higher hardness on TS than on SS, which is attributed to the irreversible plastic deformation (delamination, crack deflection, *etc.*) on SS [159,164,165].

For textured bulk MAX phases, crack formation and propagation along layers (perpendicular to the *c*-axis orientation) requires breaking

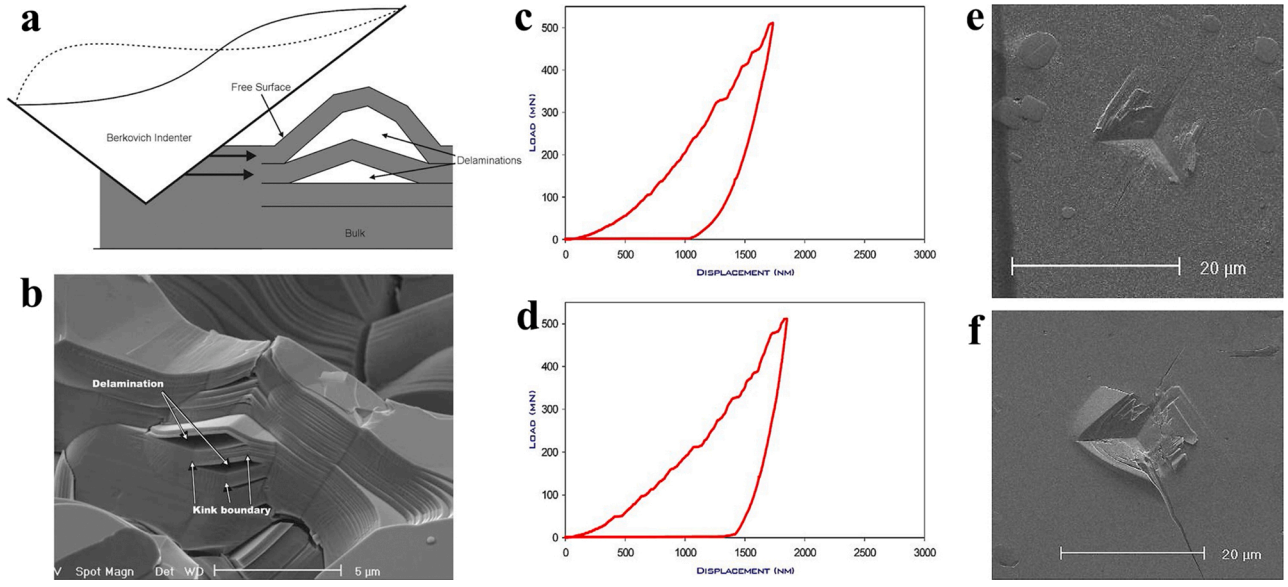

Fig. 24. (a) delamination and kink band formation caused by a nano-indentation on plate-like Ti_3SiC_2 grains parallel to the sample surface; (b) kink bands observed in a porous Ti_3SiC_2 bulk sample; (c) and (d) load-displacement curves for nano-indentations on plate-like Ti_3SiC_2 grains perpendicular and parallel to the surface, respectively; (e) and (f) morphologies of nano-indentations corresponding to (c) and (d), respectively.
(a, c~f): Reproduced with permission from Ref. [168], © 2003 Acta Materialia Inc. Published by Elsevier Ltd.; (b): Reproduced with permission from Ref. [169], © 2005 Acta Materialia Inc. Published by Elsevier Ltd.

of the weak M—A bonds, which is much easier than fracture parallel to the *c*-axis orientation which requires breaking of the stronger M—X bonds and AA— bonds, leading to a higher flexural strength and fracture toughness along the *c*-axis orientation [22,23,165,167], as shown in Table 4.

As stated in Section 5.1, ball milling of synthesized bulk MAX phases to form fine plate-like grains is needed to prepare highly textured bulk MAX phases. The ball milling process could introduce some oxygen into these plate-like grains, resulting in the formation of oxides during sintering. Such homogeneously distributed nano-sized oxide particles in the MAX phase matrix could play a role in strengthening as well as toughening by crack deflection and blunting [165,170]. Fig. 25 shows the crack propagation paths perpendicular and parallel to the *c*-axis orientation of a textured Ti_3AlC_2 bulk sample prepared by slip casting in a magnetic field using ball milled Ti_3AlC_2 powders and subsequent SPS. The white particles are Al_2O_3 formed by the oxidation of Al, which deflect and blunt cracks along both directions. The nano-laminated structure itself also leads to a zigzag crack propagation path through layers, as shown in Fig. 25(a). Due to these Al_2O_3 particles, textured Ti_3AlC_2 bulk samples possess high flexural strength (> 1000 MPa) and fracture toughness (> 13 MPa· $m^{1/2}$) along both directions, as shown in Table 4.

(2) Thermal conductivity and electrical conductivity

Due to the mixed covalent-ionic-metallic nature of chemical bonds in MAX phases, both electrons and phonons contribute to their thermal conduction. The thermal conductivity of a MAX phase can be estimated according to Eq. (19) [171,172]:

$$k = k_e + k_{ph} \tag{19}$$

where k_e and k_{ph} are the contributions of electrons and phonons to the thermal conductivity, respectively. k_e can be estimated according to the Wiedmann-Franz law [171,172]:

$$k_e = L_0 \sigma T \tag{20}$$

where L_0 is the classic Lorenz number equaling to 2.45×10^{-8} W·Ω· K^{-2}, and σ is the electrical conductivity at the temperature *T*.

The anisotropy in the electrical conductivity varies strongly between different MAX phases due to their different densities of states (DOS) around the Fermi level. For example, textured Ti_3AlC_2 has a higher electrical conductivity parallel to the *c*-axis orientation [165], while textured Nb_4AlC_3 has a higher electrical conductivity perpendicular to the *c*-axis orientation [164]. For Nb_4AlC_3, Nb *d* electrons mainly contribute to the DOS around the Fermi level, while Al electrons do not have significant contribution to the DOS around the Fermi level due to the "scooping effect" caused by Nb *d* states, resulting in a higher electrical conductivity along layers [173]. For Ti_3AlC_2, the number of Ti_{II} 3*d* states, which are around the Fermi level and mainly contribute to electrical conduction, increases significantly by the introduction of Al, thus Ti_3AlC_2 has a higher electrical conductivity along the stacking direction of Ti—Al bonds, *i.e.*, the *c*-axis orientation [174].

Unlike the electrical conductivity, the thermal conductivity parallel to the *c*-axis orientation of textured bulk MAX phases is always lower than that perpendicular to the *c*-axis orientation, even for Ti_2AlN and Ti_3AlC_2 which possess a higher electrical conductivity along the *c*-axis orientation [153,164,165], as shown in Table 4. Such phenomenon is attributed to the phonon contributions to the thermal conduction of MAX phases. For example, according to the Wiedmann-Franz law, the phonon contributions of Ti_2AlN and Ti_3AlC_2 to their total thermal conductivity are both around 50 % at room temperature [175]. Phonon conduction is faster along layers than through layers due to the strong M—X and AA— bonds in layers and the weak M—A bonds between layers. Besides, there are more grain boundaries along the *c*-axis orientation, which can cause more serious phonon scattering. Therefore, textured bulk MAX phases always possess a higher thermal conductivity perpendicular to the *c*-axis orientation.

(3) Oxidation resistance

Due to the layered structure of MAX phases, the defect migration along layers is much easier than that through layers, as discussed in Section 3.1. Therefore, the oxidation process of MAX phases is anisotropic. Song et al. [176] studied the anisotropic oxidation rates of HP-ed Ti_3AlC_2 bulk samples by oxidizing their fresh fracture surfaces containing grains with different orientations at 1373 K in air for different time. Firstly, nano oxide particles mainly containing Al_2O_3 form preferentially on the ledges of fractured plate-like Ti_3AlC_2 grains (Fig. 26(a)), which demonstrates that defect formation and migration for Al is much easier than that for Ti and defect migration along layers is much easier than that through layers, as discussed in Section 3.1. These nano Al_2O_3 particles on ledges tend to spread (Fig. 26(b)) to form an Al_2O_3 layer with a thickness of about 100 nm (Fig. 26(c)). The Al_2O_3 layer thickens with some fine faceted TiO_2 particles formed on it (Fig. 26(d)). Prolonged oxidation results in the formation of a porous layer composed of loose Al_2O_3 and TiO_2 particles between the dense Al_2O_3 layer and the Ti_3AlC_2 matrix (Fig. 26(e, f)). The compositions of the multilayer oxide film are demonstrated in the EDS line scan (Fig. 26(g, h)). The outside faceted particles are TiO_2, beneath which is the initial Al_2O_3 film with a small amount of TiO_2, and the porous layer containing Al_2O_3 and TiO_2 is adjacent to the Ti_3AlC_2 matrix. Fig. 26(i–l) shows the schematic diagrams of the oxidation process. Firstly, nano Al_2O_3 particles form on the ledges of plate-like Ti_3AlC_2 grains (Fig. 26(i)), which spread and form a dense Al_2O_3 layer with some nucleation of TiO_2 between them (Fig. 26(j)). The oxide layer grows both inwards (the oxygen diffuses through the oxide layer and reacts with Al atoms and small amount Ti atoms which have diffused outwards from the Ti_3AlC_2 matrix to the interface,

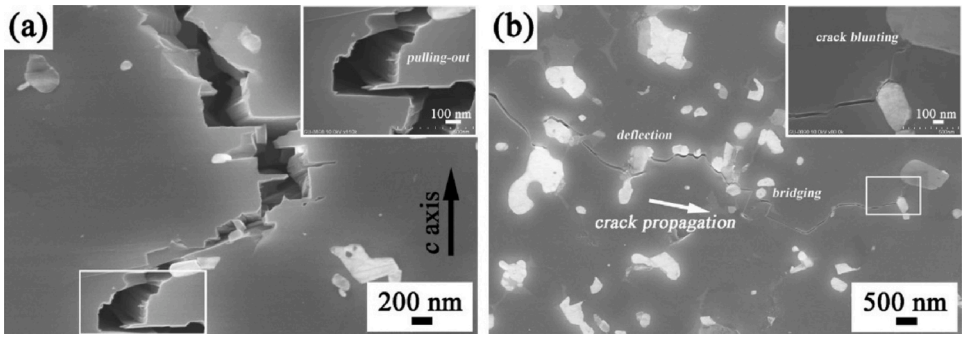

Fig. 25. Crack propagation paths along different directions of a textured Ti_3AlC_2 bulk sample containing 15 vol.% Al_2O_3: (a) parallel to the *c*-axis orientation on SS; (b) perpendicular to the *c*-axis orientation on TS.
Reproduced with permission from Ref. [165], © 2014 Elsevier Ltd.

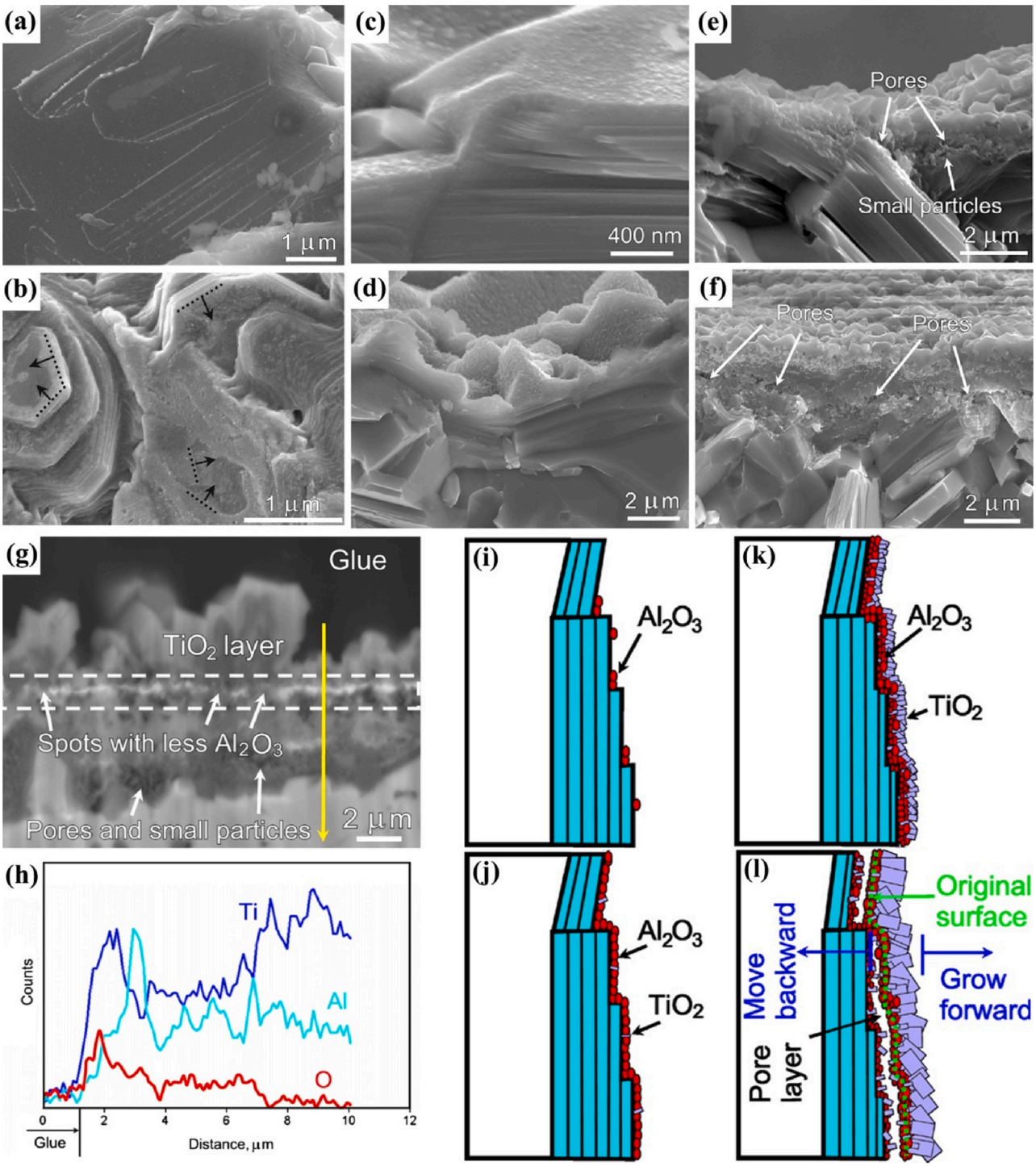

Fig. 26. Characterization of Ti_3AlC_2 bulk samples with fresh fracture surfaces oxidized at 1373 K in air for different time: (a) and (b) fracture surfaces oxidized for 20 s and 180 s, respectively; (c~f) cross-sections of fracture surfaces oxidized for (c) 180 s, (d) 360 s, (e) 600 s and (f) 900 s, respectively; (g) and (h) polished cross-sections of fracture surfaces oxidized for 900 s and the elemental concentrations from EDS line scan along the yellow line, respectively; (i~l) schematic diagrams of (i) nucleation of Al_2O_3 on the ledges of fractured plate-like Ti_3AlC_2 grains, (j) formation of the Al_2O_3 layer and nucleation of TiO_2 at Al_2O_3 grain boundaries, (k) inward growth of the Al_2O_3 layer and outward growth of the TiO_2 layer, and (d) formation of the porous oxide layer due to further volume loss caused by oxidation, respectively.
Reproduced with permission from Ref. [176], © 2008 Elsevier B.V (For interpretation of the references to colour in this figure legend, the reader is referred to the web version of this article).

forming Al_2O_3 and TiO_2) and outwards (Ti atoms diffuse outwards and react with the oxygen, forming TiO_2) (Fig. 26(k)). When the volume loss of the Ti_3AlC_2 matrix caused by oxidation cannot be compensated by these oxides growing inwards, a porous oxide layer forms between the initial dense Al_2O_3 layer and the Ti_3AlC_2 matrix (Fig. 26(l)).

As the oxidation rates along different crystal directions of MAX phases are different, the oxidation resistance of textured bulk MAX phases should be anisotropic. Xu et al. [177] studied the anisotropic oxidation resistance of textured Ti_3AlC_2 bulk samples prepared by MA and subsequent SPS. For temperatures below 1373 K, the weight gain of

both TS and SS proceeds in a parabolic manner against the oxidation time, indicating a good oxidation resistance (Fig. 25(a, b)). For temperatures higher than 1473 K, the weight gain of TS increases dramatically against the oxidation time, while the good oxidation resistance of SS is maintained. The oxide layer on TS mainly contains TiO_2 and Al_2O_3 after oxidation below 1373 K (Fig. 27(c, d)), which is similar to the research of Song et al. [176]. Although Al_2O_3 contributes to the oxidation resistance of TS below 1373 K, compared with the dense Al_2O_3 layer on SS (Fig. 27(g, h)), the porous oxide layer on TS is beneficial to the diffusion of oxygen and Al/Ti atoms, resulting in a much thicker oxide layer on TS than on SS. For TS and temperatures higher than 1473 K, Al_2O_3 almost completely reacted with TiO_2, leading to the formation of a more porous oxide layer composed of Al_2TiO_5 and TiO_2 (Fig. 27(e, f)). For SS, the dense Al_2O_3 layer can be maintained at temperatures lower than 1473 K, while a large amount of Al_2TiO_5 is formed after oxidation at 1573 K for 20 h (Fig. 27(j)). Microstructural observations prove that the oxide layer on TS after oxidation at 1373 K for 20 h is porous, while the oxide layer on SS after oxidation at 1473 K for 20 h is composed of dense Al_2O_3 grains with very few small and closed pores (Fig. 27(k–n)). The better oxidation resistance of SS than TS of textured Ti_3AlC_2 bulk samples is attributed to the faster diffusion of Al atoms along layers than that through layers, leading to the rapid formation of a dense Al_2O_3 layer on SS which significantly slow down the further oxidation of the Ti_3AlC_2 matrix under SS.

6. Summary and outlook

This review paper summarizes the formation mechanisms, the defect structure and its relation to the self-healing performance and radiation tolerance, solid solutions and how this can be used to tailor properties, texture formation and finally the anisotropy in properties of MAX phases. The following points are summarized:

(1) To obtain MAX phases with a high purity, the elemental A content in the starting materials, the synthesis temperature and holding time need to be adjusted considering the vaporization of the A element and the formation of intermediate phases during the synthesis process. Besides, the introduction of intermediate phases M_xX_y in the starting materials can lower the formation temperature of MAX phases and improve the purity.

(2) The formation energies of intrinsic point defects vary depending on the compositions of MAX phases. For most MAX phases, the formation energies of A_{FP} and X_{FP} are lower than that of M_{FP}. The formation energies of M_A-A_M anti-site pairs are much lower than those of M_X-X_M and A_X-X_A anti-site pairs, which is in correspondence with the fact that the M—A bonds are relatively weaker than the M—X bonds. The weaker MA— bonds also promote the formation and migration of defects along the A layers, making the $M_{n+1}A$ block act as a defect sink. MAX phases with higher electronegative differences between M and A atoms tend to possess higher formation energies of M_A-A_M anti-site pairs, which are strongly related to their radiation tolerance. Besides, as the self-healing performance of MAX phases depends on the oxidation of the A element, which would leave A vacancies in MAX phases, the theoretical calculation of the stability of MAX phases with A vacancies can provide important guidance on their application as self-healing materials.

(3) The configurations of M alloyed $M_{n+1}AX_n$ phase solid solutions can be either ordered or disordered, which are determined by the formation enthalpy, the relationship between the order-disorder

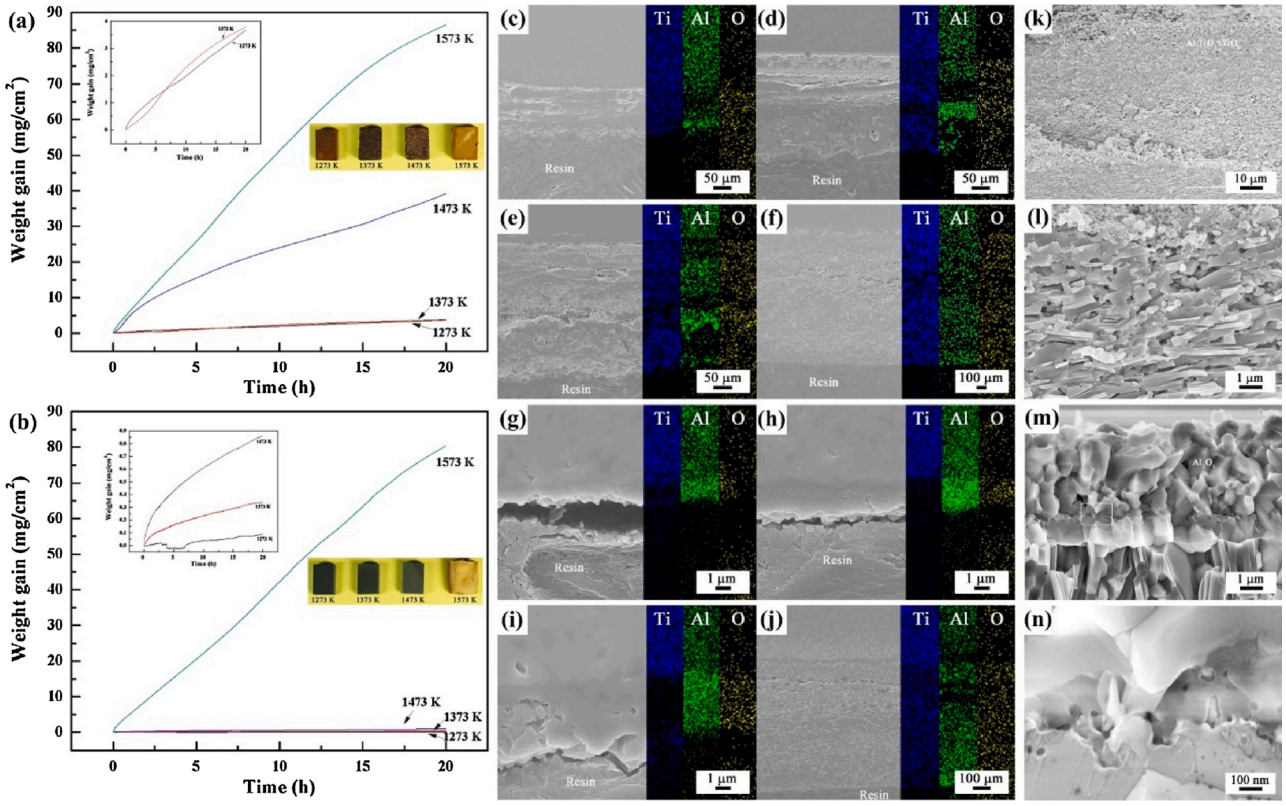

Fig. 27. Characterization of textured Ti_3AlC_2 bulk samples oxidized at different temperatures in a flowing mixture gas (N_2 and O_2 with a volume ratio of 78:22) for 20 h: (a) and (b) weight gain per unit surface area *vs*. oxidation time at different temperatures for TS and SS, respectively; (c~f) polished cross-sections of TS oxidized at (c) 1273 K, (d) 1373 K, (e) 1473 K and (f) 1573 K, respectively; (g~j) polished cross-sections of SS oxidized at (g) 1273 K, (h) 1373 K, (i) 1473 K and (j) 1573 K, respectively; (k) and (l) cross-sections of TS oxidized at 1373 K; (m) and (n) cross-sections of SS oxidized at 1473 K.
Reproduced with permission from Ref. [177], © 2018 Elsevier Ltd.

transformation temperature ($T_{disorder}$) and the synthesis temperature of solid solutions. MAX phase solid solutions can be used to tailor their mechanical properties, physical properties, oxidation resistance, *etc*. Whether a MAX phase solid solution employs solid solution strengthening/toughening or not seems like to be strongly influenced by the change rate of the lattice parameter *c* with the change of the content of alloying atoms in the MAX phase solid solution (c_{CR}), which needs to be verified by further experiments. Similar to their mechanical properties, no simple linear relationship exists for the CTEs of MAX phase solid solutions and their end members, which reflect the average bonding strength. For the electrical conductivity, alloying atoms on the M-site have a more significant solid solution scattering effect, while alloying atoms on the A-site only lead to slight scattering, which is attributed to the fact that the electrical conduction in MAX phases is mainly driven by the transition metal atoms. Some alloying atoms can introduce magnetic properties to MAX phases which do not normally show magnetic properties.

(4) Textured bulk MAX phases can be prepared by pressure-assisted sintering (HP and SPS) and magnetic alignment (MA) followed by sintering. The anisotropy in the hardness of textured MAX phases varies for different loads due to the easier kink band formation on TS under lower loads and the irreversible plastic deformation on SS under higher loads. The preferential orientation of plate-like grains in textured MAX phases results in zigzag crack propagation paths through layers, giving them a high toughness. The anisotropy in the electrical conductivity could be different for different MAX phases, which is determined by the DOS at the Fermi level. While the thermal conductivity parallel to the *c*-axis orientation of textured MAX phases is always lower than that perpendicular to the *c*-axis orientation due to the contribution of phonon conduction. For MAX phases with a good oxidation resistance (e.g., $Ti_{n+1}AlC_n$), texturing gives them a better oxidation resistance on SS due to the faster diffusion of A atoms along layers which results in the faster formation of a protective dense oxide scale on SS.

Although much research progress has been achieved in the field of MAX phase synthesis and properties, there are still some issues which need to be solved or more deeply investigated. The stability of MAX phases with A vacancies, which can provide important guidance on their application as self-healing materials, need to be widely studied. Theoretical basis needs to be given to judge whether a MAX phase solid solution employs solid solution strengthening/toughening or not (c_{CR} is proposed as a basis for judgment in this review, which needs to be verified by further experiments). The magnetic properties of MAX phases and their solid solutions are also an area to be further studied, especially tailoring magnetic properties by controlling the atomic configuration, the composition of multiple alloying elements, the temperature, the magnetic field or the applied pressure. For textured MAX phases which possess improved properties along specific directions, ball milling of synthesized bulk MAX phases, which usually introduces some oxygen into the raw powders, is usually needed to prepare highly textured MAX phases. Although the formed oxide particles usually play a role of strengthening and toughening by crack deflection and blunting, they are harmful to thermal and electrical conduction due to their scattering effect, which needs to be solved for textured MAX phases used in heat sinks or electrical parts. Therefore, more effective texturing techniques for MAX phases need to be developed.

Declaration of Competing Interest

The authors declare that they have no known competing financial interests or personal relationships that could have appeared to influence the work reported in this paper.

Acknowledgement

The authors appreciate the financial support from the China Scholarship Council (CSC) for Zhuo Zhang (No. 201906120174).

References

[1] T. Rackl, Increasing the Chemical Diversity of MAX Phases, lmu, 2020.
[2] M.A. Ali, M.M. Hossain, M.M. Uddin, M.A. Hossain, A.K.M.A. Islam, S.H. Naqib, Physical properties of new MAX phase borides M_2SB (M = Zr, Hf and Nb) in comparison with conventional MAX phase carbides M_2SC (M = Zr, Hf and Nb): comprehensive insights, Mater. Sci. (2020) p. arXiv:2009.04236.
[3] M.A. Ali, M.M. Hossain, A.K.M.A. Islam, S.H. Naqib, Recently predicted ternary boride Hf_3PB_4: insights into the physical properties of this hardest possible boride MAX phase, Mater. Sci. (2020) p. arXiv:2009.05707.
[4] Z.M. Sun, Progress in research and development on MAX phases: a family of layered ternary compounds, Int. Mater. Rev. 56 (3) (2011) 143–166.
[5] P. Naik Parrikar, R. Benitez, M. Radovic, A. Shukla, Effect of microstructure on mechanical response of MAX phases, in: W.C. Ralph, R. Singh, G. Tandon, P. R. Thakre, P. Zavattieri, Y. Zhu (Eds.), Mechanics of Composite and Multi-Functional Materials, Volume 7, Springer International Publishing, Cham, 2017, pp. 171–175.
[6] A.S. Ingason, M. Dahlqvist, J. Rosen, Magnetic MAX phases from theory and experiments; a review, J. Phys. Condens. Matter 28 (43) (2016), 433003.
[7] M. Magnuson, M. Mattesini, Chemical bonding and electronic-structure in MAX phases as viewed by X-ray spectroscopy and density functional theory, Thin Solid Films 621 (2017) 108–130.
[8] C. Hu, H. Zhang, F. Li, Q. Huang, Y. Bao, New phases' discovery in MAX family, Int. J. Refract. Met. Hard Mater. 36 (2013) 300–312.
[9] M.W. Barsoum, The $M_{N+1}AX_N$ phases: a new class of solids: thermodynamically stable nanolaminates, Prog. Solid State Chem. 28 (1) (2000) 201–281.
[10] M.W. Barsoum, M. Radovic, Elastic and mechanical properties of the MAX phases, Annu. Rev. Mater. Res. 41 (1) (2011) 195–227.
[11] W.-Y. Ching, Y. Mo, S. Aryal, P. Rulis, Intrinsic mechanical properties of 20 MAX-Phase compounds, J. Am. Ceram. Soc. 96 (7) (2013) 2292–2297.
[12] C. Lange, M.W. Barsoum, P. Schaaf, Towards the synthesis of MAX-phase functional coatings by pulsed laser deposition, Appl. Surf. Sci. 254 (4) (2007) 1232–1235.
[13] M. Radovic, M.W. Barsoum, MAX phases: bridging the gap between metals and ceramics, Am. Ceram. Soc. Bull. 92 (3) (2013) 20–27.
[14] E.N. Hoffman, D.W. Vinson, R.L. Sindelar, D.J. Tallman, G. Kohse, M.W. Barsoum, MAX phase carbides and nitrides: properties for future nuclear power plant in-core applications and neutron transmutation analysis, Nucl. Eng. Des. 244 (2012) 17–24.
[15] B. Liu, J.Y. Wang, J. Zhang, J.M. Wang, F.Z. Li, Y.C. Zhou, Theoretical investigation of A-element atom diffusion in Ti_2AC (A=Sn, Ga, Cd, In, and Pb), Appl. Phys. Lett. 94 (18) (2009), 181906.
[16] A. Farle, L. Boatemaa, L. Shen, S. Gövert, J.B.W. Kok, M. Bosch, S. Yoshioka, S. van der Zwaag, W.G. Sloof, Demonstrating the self-healing behaviour of some selected ceramics under combustion chamber conditions, Smart Mater. Struct. 25 (8) (2016), 084019.
[17] A.-S. Farle, C. Kwakernaak, S. van der Zwaag, W.G. Sloof, A conceptual study into the potential of $M_{n+1}AX_n$-phase ceramics for self-healing of crack damage, J. Eur. Ceram. Soc. 35 (1) (2015) 37–45.
[18] M. Haftani, M. Saeedi Heydari, H.R. Baharvandi, N. Ehsani, Studying the oxidation of Ti_2AlC MAX phase in atmosphere: a review, Int. J. Refract. Met. Hard Mater. 61 (2016) 51–60.
[19] T. Liao, J. Wang, Y. Zhou, First-principles investigation of intrinsic defects and (N, O) impurity atom stimulated Al vacancy in Ti_2AlC, Appl. Phys. Lett. 93 (26) (2008), 261911.
[20] J. Xiao, T. Yang, C. Wang, J. Xue, Y. Wang, S. Sinnott, Investigations on radiation tolerance of $M_{n+1}AX_n$ phases: study of Ti_3SiC_2, Ti_3AlC_2, Cr_2AlC, Cr_2GeC, Ti_2AlC, and Ti_2AlN, J. Am. Ceram. Soc. 98 (4) (2015) 1323–1331.
[21] X.M. Duan, L. Shen, D.C. Jia, Y. Zhou, S. van der Zwaag, W.G. Sloof, Synthesis of high-purity, isotropic or textured Cr_2AlC bulk ceramics by spark plasma sintering of pressure-less sintered powders, J. Eur. Ceram. Soc. 35 (5) (2015) 1393–1400.
[22] K. Sato, M. Mishra, H. Hirano, T.S. Suzuki, Y. Sakka, Fabrication of textured Ti_3SiC_2 ceramic by slip casting in a strong magnetic field and pressureless sintering, J. Ceram. Soc. Jpn. 122 (1429) (2014) 817–821.
[23] X. Xie, R. Yang, Y. Cui, Q. Jia, C. Bai, Fabrication of textured Ti_2AlC lamellar composites with improved mechanical properties, J. Mater. Sci. Technol. 38 (2020) 86–92.
[24] S. Hashimoto, N. Nishina, K. Hirao, Y. Zhou, H. Hyuga, S. Honda, Y. Iwamoto, Formation mechanism of Ti_2AlC under the self-propagating high-temperature synthesis (SHS) mode, Mater. Res. Bull. 47 (5) (2012) 1164–1168.
[25] T. Thomas, C.R. Bowen, Effect of particle size on the formation of Ti_2AlC using combustion synthesis, Ceram. Int. 42 (3) (2016) 4150–4157.
[26] F. Meng, B. Liang, M. Wang, Investigation of formation mechanism of Ti_3SiC_2 by self-propagating high-temperature synthesis, Int. J. Refract. Met. Hard Mater. 41 (2013) 152–161.
[27] H.-C. Oh, S.-H. Lee, S.-C. Choi, The reaction mechanism for the low temperature synthesis of Cr_2AlC under electronic field, J. Alloys. Compd. 587 (2014) 296–302.
[28] J.F. Zhu, N. Han, K. Wang, F. Wang, Fabrication of Ti_2AlN by mechanical alloying and hot press sintering, Adv. Mater. Res. 194-196 (2011) 425–428.

[29] T. Rackl, D. Johrendt, The MAX phase borides Zr_2SB and Hf_2SB, Solid State Sci. 106 (2020), 106316.
[30] W.B. Zhou, B.C. Mei, J.Q. Zhu, X.L. Hong, Rapid synthesis of Ti_2AlC by spark plasma sintering technique, Mater. Lett. 59 (1) (2005) 131–134.
[31] N.F. Gao, Y. Miyamoto, D. Zhang, On physical and thermochemical properties of high-purity Ti_3SiC_2, Mater. Lett. 55 (1) (2002) 61–66.
[32] G. Ying, X. He, M. Li, W. Han, F. He, S. Du, Synthesis and mechanical properties of high-purity Cr_2AlC ceramic, Mater. Sci. Eng. A 528 (6) (2011) 2635–2640.
[33] X. Wang, Y. Zhou, Solid-liquid reaction synthesis and simultaneous densification of polycrystalline Ti_2AlC, Zeitschrift für Metallkunde 93 (1) (2002) 66–71.
[34] J. Zhu, J. Gao, J. Yang, F. Wang, K. Niihara, Synthesis and microstructure of layered-ternary Ti_2AlC ceramic by high energy milling and hot pressing, Mater. Sci. Eng. A 490 (1-2) (2008) 62–65.
[35] P. Wang, B. Mei, X. Hong, J. Zhu, W. Zhou, Fabrication of Ti2AlC by spark plasma sintering from elemental powders and thermodynamics analysis of Ti-Al-C system, J. Wuhan Univ. Technol. Mater. Sci. Ed. 22 (2) (2007) 325–328.
[36] C. Hu, F. Li, J. Zhang, J. Wang, J. Wang, Y. Zhou, Nb_4AlC_3: A new compound belonging to the MAX phases, Scripta Mater. 57 (10) (2007) 893–896.
[37] M.F. Ud Din, C. Yang, Y. Tang, Y. Tian, Y. Luo, Y. Wu, W. Que, Efficient and cost-effective method to synthesize highly purified Ti_4AlN_3 and Ti_2AlN, J. Adv. Dielectr. 09 (01) (2019), 1950008.
[38] D.P. Riley, E.H. Kisi, The design of crystalline precursors for the synthesis of $M_{n+1}AX_n$Phases and their application to Ti_3AlC_2, J. Am. Ceram. Soc. 90 (7) (2007) 2231–2235.
[39] Z. Wang, W. Li, Y. Liu, J. Shuai, P. Ke, A. Wang, Diffusion-controlled intercalation approach to synthesize the Ti_2AlC MAX phase coatings at low temperature of 550 °C, Appl. Surf. Sci. 502 (2020), 144130.
[40] J.-H. Han, S.-S. Hwang, D. Lee, S.-W. Park, Synthesis and mechanical properties of Ti_3AlC_2 by hot pressing TiC_x/Al powder mixture, J. Eur. Ceram. Soc. 28 (5) (2008) 979–988.
[41] Y. Zhou, Z. Sun, Crystallographic relations between $Ti3SiC_2$ and TiC, Mater. Res. Innov. 3 (5) (2000) 286–291.
[42] Z. Xiao, X. Zhu, Z. Chu, W. Xu, Z. Wang, B. Wu, Investigation of Ti_2AlC formation mechanism through carbon and TiAl diffusional reaction, J. Eur. Ceram. Soc. 38 (4) (2018) 1246–1252.
[43] Y. Liu, L. Zhang, W. Xiao, L. Zhang, Y. Pu, S. Guo, Rapid synthesis of Ti_2AlN ceramic via thermal explosion, Mater. Lett. 149 (2015) 5–7.
[44] C. Peng, C.-A. Wang, Y. Song, Y. Huang, A novel simple method to stably synthesize Ti_3AlC_2 powder with high purity, Mater. Sci. Eng. A 428 (1-2) (2006) 54–58.
[45] J. Wang, B. Liu, J. Wang, Y. Zhou, Theoretical investigation of thermodynamic stability and mobility of the intrinsic point defects in Ti_3AC_2 (A = Si, Al), Phys. Chem. Chem. Phys. 17 (14) (2015) 8927–8934.
[46] S.R.G. Christopoulos, P.P. Filippatos, M.A. Hadi, N. Kelaidis, M.E. Fitzpatrick, A. Chroneos, Intrinsic defect processes and elastic properties of Ti_3AC_2 (A = Al, Si, Ga, Ge, In, Sn) MAX phases, J. Appl. Phys. 123 (2) (2018), 025103.
[47] K.E. Sickafus, L. Minervini, R.W. Grimes, J.A. Valdez, M. Ishimaru, F. Li, K. J. McClellan, T. Hartmann, Radiation tolerance of complex oxides, Science 289 (5480) (2000) 748.
[48] F. Kröger, H. Vink, Relations between the concentrations of imperfections in crystalline solids. Solid State Physics, Elsevier, 1956, pp. 307–435.
[49] S.R.G. Christopoulos, N. Kelaidis, A. Chroneos, Defect processes of M_3AlC_2 (M = V, Zr, Ta, Ti) MAX phases, Solid State Commun. 261 (2017) 54–56.
[50] H. Han, D. Wickramaratne, Q. Huang, J. Dai, T. Li, H. Wang, W. Zhang, P. Huai, A first-principles study on the defective properties of MAX phase Cr_2AlC: the magnetic ordering and strong correlation effect, RSC Adv. 6 (87) (2016) 84262–84268.
[51] J.-C. Lei, X. Zhang, Z. Zhou, Recent advances in MXene: preparation, properties, and applications, Front. Phys. 10 (3) (2015) 276–286.
[52] A. Feng, Y. Yu, Y. Wang, F. Jiang, Y. Yu, L. Mi, L. Song, Two-dimensional MXene Ti_3C_2 produced by exfoliation of Ti_3AlC_2, Mater. Des. 114 (2017) 161–166.
[53] Z. Guo, L. Zhu, J. Zhou, Z. Sun, Microscopic origin of MXenes derived from layered MAX phases, RSC Adv. 5 (32) (2015) 25403–25408.
[54] I. Shein, A. Ivanovskii, Graphene-like nanocarbides and nanonitrides of d metals (MXenes): synthesis, properties and simulation, Micro & Nano Letters, IET 8 (2013) 59–62.
[55] M.A. Hadi, S.R.G. Christopoulos, S.H. Naqib, A. Chroneos, M.E. Fitzpatrick, A.K. M.A. Islam, Physical properties and defect processes of M_3SnC_2 (M = Ti, Zr, Hf) MAX phases: effect of M-elements, J. Alloys. Compd. 748 (2018) 804–813.
[56] S.C. Middleburgh, G.R. Lumpkin, D. Riley, Y. Zhon, Accommodation, accumulation, and migration of defects in Ti_3SiC_2 and Ti_3AlC_2 MAX phases, J. Am. Ceram. Soc. 96 (10) (2013) 3196–3201.
[57] J. Emmerlich, D. Music, P. Eklund, O. Wilhelmsson, U. Jansson, J.M. Schneider, H. Högberg, L. Hultman, Thermal stability of Ti_3SiC_2 thin films, Acta Mater. 55 (4) (2007) 1479–1488.
[58] J. Zhang, J.Y. Wang, Y.C. Zhou, Structure stability of Ti_3AlC_2 in Cu and microstructure evolution of Cu-Ti_3AlC_2 composites, Acta Mater. 55 (13) (2007) 4381–4390.
[59] J. Wang, Y. Zhou, T. Liao, J. Zhang, Z. Lin, A first-principles investigation of the phase stability of Ti_2AlC with Al vacancies, Scripta Mater. 58 (3) (2008) 227–230.
[60] D.J. Tallman, L. He, B.L. Garcia-Diaz, E.N. Hoffman, G. Kohse, R.L. Sindelar, M. W. Barsoum, Effect of neutron irradiation on defect evolution in Ti_3SiC_2 and Ti_2AlC, J. Nucl. Phys. Mater. Sci. Radiat. Appl. 468 (2016) 194–206.
[61] J.C. Nappé, P. Grosseau, F. Audubert, B. Guilhot, M. Beauvy, M. Benabdesselam, I. Monnet, Damages induced by heavy ions in titanium silicon carbide: Effects of nuclear and electronic interactions at room temperature, J. Nucl. Phys. Mater. Sci. Radiat. Appl. 385 (2) (2009) 304–307.
[62] D.W. Clark, S.J. Zinkle, M.K. Patel, C.M. Parish, High temperature ion irradiation effects in MAX phase ceramics, Acta Mater. 105 (2016) 130–146.
[63] M. Le Flem, X. Liu, S. Doriot, T. Cozzika, I. Monnet, Irradiation damage in $Ti_3(Si, Al)C_2$: a TEM investigation, Int. J. Appl. Ceram. Tec. 7 (6) (2010) 766–775.
[64] S. Zhao, J. Xue, Y. Wang, Q. Huang, Ab initio study of irradiation tolerance for different Mn+1AXn phases: Ti3SiC2 and Ti3AlC2, J. Appl. Phys. 115 (2) (2014), 023503.
[65] H. Wang, R. Araujo, J.G. Swadener, Y.Q. Wang, X. Zhang, E.G. Fu, T. Cagin, Ion irradiation effects in nanocrystalline TiN coatings, Nucl. Instrum. Methods Phys. Res. B 261 (1) (2007) 1162–1166.
[66] M. Jiang, H.Y. Xiao, H.B. Zhang, S.M. Peng, C.H. Xu, Z.J. Liu, X.T. Zu, A comparative study of low energy radiation responses of SiC, TiC and ZrC, Acta Mater. 110 (2016) 192–199.
[67] Q. Huang, R. Liu, G. Lei, H. Huang, J. Li, S. He, D. Li, L. Yan, J. Zhou, Q. Huang, Irradiation resistance of MAX phases Ti_3SiC_2 and Ti_3AlC_2: characterization and comparison, J. Nucl. Phys. Mater. Sci. Radiat. Appl. 465 (2015) 640–647.
[68] T. Yang, C. Wang, C.A. Taylor, X. Huang, Q. Huang, F. Li, L. Shen, X. Zhou, J. Xue, S. Yan, Y. Wang, The structural transitions of Ti_3AlC_2 induced by ion irradiation, Acta Mater. 65 (2014) 351–359.
[69] T. Yang, C. Wang, W. Liu, S. Liu, J. Xiao, Q. Huang, J. Xue, S. Yan, Y. Wang, Formation of nano-twinned structure in Ti_3AlC_2 induced by ion-irradiation, Acta Mater. 128 (2017) 1–11.
[70] T. Yang, C. Wang, W. Liu, S. Liu, J. Xiao, Q. Huang, Y. Wang, S.J. Zinkle, Comparison of irradiation tolerance of two MAX phases-Ti_4AlN_3 and Ti_2AlN, J. Nucl. Phys. Mater. Sci. Radiat. Appl. 513 (2019) 120–128.
[71] C. Wang, T. Yang, J. Xiao, S. Liu, J. Xue, J. Wang, Q. Huang, Y. Wang, Irradiation-induced structural transitions in Ti_2AlC, Acta Mater. 98 (2015) 197–205.
[72] K.R. Whittle, M.G. Blackford, R.D. Aughterson, S. Moricca, G.R. Lumpkin, D. P. Riley, N.J. Zaluzec, Radiation tolerance of $M_{n+1}AX_n$ phases, Ti_3AlC_2 and Ti_3SiC_2, Acta Mater. 58 (13) (2010) 4362–4368.
[73] I.-T. Bae, M. Ishimaru, Y. Hirotsu, S. Matsumura, K.E. Sickafus, Ion-beam-induced amorphous structures in silicon carbide, Nucl. Instrum. Methods Phys. Res. B 206 (2003) 974–978.
[74] X.M. Liu, M. Le Flem, J.L. Béchade, I. Monnet, Nanoindentation investigation of heavy ion irradiated $Ti_3(Si,Al)C_2$, J. Nucl. Phys. Mater. Sci. Radiat. Appl. 401 (1–3) (2010) 149–153.
[75] L.F. Marion, I. Monnet, Saturation of irradiation damage in $(Ti,Zr)_3(Si,Al)C_2$ compounds, J. Nucl. Phys. Mater. Sci. Radiat. Appl. 433 (1–3) (2013) 534–537.
[76] T. El-Raghy, S. Chakraborty, M.W. Barsoum, Synthesis and characterization of Hf_2PbC, Zr_2PbC and M_2SnC (M=Ti, Hf, Nb or Zr), J. Eur. Ceram. Soc. 20 (14) (2000) 2619–2625.
[77] C. Hu, F. Li, L. He, M. Liu, J. Zhang, J. Wang, Y. Bao, J. Wang, Y. Zhou, In situ reaction synthesis, electrical and thermal, and mechanical properties of Nb_4AlC_3, J. Am. Ceram. Soc. 91 (7) (2008) 2258–2263.
[78] C. Hu, Z. Lin, L. He, Y. Bao, J. Wang, M. Li, Y. Zhou, Physical and mechanical properties of bulk Ta_4AlC_3 ceramic prepared by an in situ reaction Synthesis/Hot-Pressing method, J. Am. Ceram. Soc. 90 (8) (2007) 2542–2548.
[79] Y. Zhou, F. Meng, J. Zhang, New MAX-Phase compounds in the V-Cr-Al-C system, J. Am. Ceram. Soc. 91 (4) (2008) 1357–1360.
[80] Z. Liu, T. Waki, Y. Tabata, H. Nakamura, Mn-doping-induced itinerant-electron ferromagnetism in Cr_2GeC, Phys. Rev. B 89 (5) (2014), 054435.
[81] D. Ohmer, I. Opahle, H.K. Singh, H. Zhang, Stability predictions of magnetic M_2AX compounds, J. Phys. Condens. Matter 31 (40) (2019), 405902.
[82] Z. Liu, L. Zheng, L. Sun, Y. Qian, J. Wang, M. Li, G.P. Bei, $(Cr_{2/3}Ti_{1/3})_3AlC_2$ and $(Cr_{5/8}Ti_{3/8})_4AlC_3$: new MAX-phase compounds in Ti-Cr-Al-C system, J. Am. Ceram. Soc. 97 (1) (2014) 67–69.
[83] Z. Liu, E. Wu, J. Wang, Y. Qian, H. Xiang, X. Li, Q. Jin, G. Sun, X. Chen, J. Wang, M. Li, Crystal structure and formation mechanism of $(Cr_{2/3}Ti_{1/3})_3AlC_2$ MAX phase, Acta Mater. 73 (2014) 186–193.
[84] E.A.N. Caspi, P. Chartier, F. Porcher, F. Damay, T. Cabioc'h, Ordering of (Cr,V) layers in Nanolamellar $(Cr_{0.5}V_{0.5})_{n+1}AlC_n$ compounds, Mater. Res. Lett. 3 (2) (2014) 100–106.
[85] B. Anasori, J. Halim, J. Lu, C.A. Voigt, L. Hultman, M.W. Barsoum, Mo_2TiAlC_2: A new ordered layered ternary carbide, Scripta Mater. 101 (2015) 5–7.
[86] B. Anasori, M. Dahlqvist, J. Halim, E.J. Moon, J. Lu, B.C. Hosler, E.A.N. Caspi, S. J. May, L. Hultman, P. Eklund, J. Rosén, M.W. Barsoum, Experimental and theoretical characterization of ordered MAX phases Mo_2TiAlC_2 and $Mo_2Ti_2AlC_3$, J. Appl. Phys. 118 (9) (2015), 094304.
[87] R. Meshkian, Q. Tao, M. Dahlqvist, J. Lu, L. Hultman, J. Rosen, Theoretical stability and materials synthesis of a chemically ordered MAX phase, Mo_2ScAlC_2, and its two-dimensional derivate Mo_2ScC_2 MXene, Acta Mater. 125 (2017) 476–480.
[88] M. Dahlqvist, J. Rosen, Order and disorder in quaternary atomic laminates from first-principles calculations, Phys. Chem. Chem. Phys. 17 (47) (2015) 31810–31821.
[89] M. Dahlqvist, J. Rosen, Predictive theoretical screening of phase stability for chemical order and disorder in quaternary 312 and 413 MAX phases, Nanoscale 12 (2) (2020) 785–794.
[90] M. Sokol, V. Natu, S. Kota, M.W. Barsoum, On the chemical diversity of the MAX phases, Trends Analyt. Chem. 1 (2) (2019) 210–223.
[91] A.S. Ingason, A. Mockute, M. Dahlqvist, F. Magnus, S. Olafsson, U.B. Arnalds, B. Alling, I.A. Abrikosov, B. Hjorvarsson, P.O. Persson, J. Rosen, Magnetic self-organized atomic laminate from first principles and thin film synthesis, Phys. Rev. Lett. 110 (19) (2013), 195502.

[92] M. Dahlqvist, B. Alling, I.A. Abrikosov, J. Rosen, Magnetic nanoscale laminates with tunable exchange coupling from first principles, Phys. Rev. B 84 (22) (2011), 220403(R).

[93] A. Mockute, M. Dahlqvist, J. Emmerlich, L. Hultman, J.M. Schneider, P.O. Å. Persson, J. Rosen, Synthesis and ab initio calculations of nanolaminated (Cr, Mn)$_2$AlC compounds, Phys. Rev. B 87 (9) (2013), 094113.

[94] Q. Tao, M. Dahlqvist, J. Lu, S. Kota, R. Meshkian, J. Halim, J. Palisaitis, L. Hultman, M.W. Barsoum, P.O.A. Persson, J. Rosen, Two-dimensional $Mo_{1.33}C$ MXene with divacancy ordering prepared from parent 3D laminate with in-plane chemical ordering, Nat. Commun. 8 (2017) 14949.

[95] M. Dahlqvist, J. Lu, R. Meshkian, Q. Tao, L. Hultman, J. Rosen, Prediction and synthesis of a family of atomic laminate phases with Kagomé-like and in-plane chemical ordering, Sci. Adv. 3 (7) (2017), e1700642.

[96] M. Dahlqvist, A. Petruhins, J. Lu, L. Hultman, J. Rosen, Origin of chemically ordered atomic laminates (i-MAX): expanding the elemental space by a Theoretical/Experimental approach, ACS Nano 12 (8) (2018) 7761–7770.

[97] Q. Tao, J. Lu, M. Dahlqvist, A. Mockute, S. Calder, A. Petruhins, R. Meshkian, O. Rivin, D. Potashnikov, E.A.N. Caspi, H. Shaked, A. Hoser, C. Opagiste, R.-M. Galera, R. Salikhov, U. Wiedwald, C. Ritter, A.R. Wildes, B. Johansson, L. Hultman, M. Farle, M.W. Barsoum, J. Rosen, Atomically layered and ordered rare-earth i-MAX phases: a new class of magnetic quaternary compounds, Chem. Mater. 31 (7) (2019) 2476–2485.

[98] L. Chen, M. Dahlqvist, T. Lapauw, B. Tunca, F. Wang, J. Lu, R. Meshkian, K. Lambrinou, B. Blanpain, J. Vleugels, J. Rosen, Theoretical prediction and synthesis of $(Cr_{2/3}Zr_{1/3})_2AlC$ i-MAX phase, Inorg. Chem. 57 (11) (2018) 6237–6244.

[99] R. Meshkian, M. Dahlqvist, J. Lu, B. Wickman, J. Halim, J. Thornberg, Q. Tao, S. Li, S. Intikhab, J. Snyder, M.W. Barsoum, M. Yildizhan, J. Palisaitis, L. Hultman, P.O.A. Persson, J. Rosen, W-based atomic laminates and their 2D derivative $W_{1.33}C$ MXene with vacancy ordering, Adv. Mater. 30 (21) (2018), e1706409.

[100] J. Lu, A. Thore, R. Meshkian, Q. Tao, L. Hultman, J. Rosen, Theoretical and experimental exploration of a novel in-plane chemically ordered $(Cr_{2/3}M_{1/3})_2AlC$ i-MAX phase with m = Sc and Y, Cryst. Growth Des. 17 (11) (2017) 5704–5711.

[101] A. Petruhins, M. Dahlqvist, J. Lu, L. Hultman, J. Rosen, Theoretical prediction and experimental verification of the chemically ordered atomic-laminate i-MAX phases $(Cr_{2/3}Sc_{1/3})_2GaC$ and $(Mn_{2/3}Sc_{1/3})_2GaC$, Cryst. Growth Des. 20 (1) (2019) 55–61.

[102] A. Petruhins, J. Lu, L. Hultman, J. Rosen, Synthesis of atomically layered and chemically ordered rare-earth (RE) i-MAX phases; $(Mo_{2/3}RE_{1/3})_2GaC$ with RE = Gd, Tb, Dy, Ho, Er, Tm, Yb, and Lu, Mater. Res. Lett. 7 (11) (2019) 446–452.

[103] J. Thornberg, J. Halim, J. Lu, R. Meshkian, J. Palisaitis, L. Hultman, P.O. A. Persson, J. Rosen, Synthesis of $(V_{2/3}Sc_{1/3})_2AlC$ i-MAX phase and $V_{2-x}C$ MXene scrolls, Nanoscale 11 (31) (2019) 14720–14726.

[104] I. Persson, A. el Ghazaly, Q. Tao, J. Halim, S. Kota, V. Darakchieva, J. Palisaitis, M.W. Barsoum, J. Rosen, P.O.Å. Persson, Tailoring structure, composition, and energy storage properties of MXenes from selective etching of in-plane, chemically ordered MAX phases, Small 14 (17) (2018), 1703676.

[105] A. Champagne, F. Ricci, M. Barbier, T. Ouisse, D. Magnin, S. Ryelandt, T. Pardoen, G. Hautier, M.W. Barsoum, J.C. Charlier, Insights into the elastic properties of RE-i-MAX phases and their potential exfoliation into two-dimensional RE-i-MXenes, Phys. Rev. B Condens. Matter Mater. Phys. 4 (1) (2020), 013604.

[106] F.L. Meng, Y.C. Zhou, J.Y. Wang, Strengthening of Ti_2AlC by substituting Ti with V, Scripta Mater. 53 (12) (2005) 1369–1372.

[107] C. Hu, L. He, M. Liu, X. Wang, J. Wang, M. Li, Y. Bao, Y. Zhou, In situ reaction synthesis and mechanical properties of V_2AlC, J. Am. Ceram. Soc. 91 (12) (2008) 4029–4035.

[108] Y.C. Zhou, J.X. Chen, J.Y. Wang, Strengthening of Ti_3AlC_2 by incorporation of Si to form $Ti_3Al_{1-x}Si_xC_2$ solid solutions, Acta Mater. 54 (5) (2006) 1317–1322.

[109] H. Gao, R. Benitez, W. Son, R. Arroyave, M. Radovic, Structural, physical and mechanical properties of $Ti_3(Al_{1-x}Si_x)C_2$ solid solution with x=0-1, Mater. Sci. Eng. A 676 (2016) 197–208.

[110] M.W. Barsoum, T. El-Raghy, M. Ali, Processing and characterization of Ti_2AlC, Ti_2AlN, and $Ti_2AlC_{0.5}N_{0.5}$, Metall. Mater. Trans. A 31 (7) (2000) 1857–1865.

[111] L. Qu, G. Bei, B. Stelzer, H. Rueß, J.M. Schneider, D. Cao, S. van der Zwaag, W. G. Sloof, Synthesis, crystal structure, microstructure and mechanical properties of $(Ti_{1-x}Zr_x)_3SiC_2$ MAX phase solid solutions, Ceram. Int. 45 (1) (2019) 1400–1408.

[112] W. Tian, Z. Sun, H. Hashimoto, Y. Du, Synthesis, microstructure and properties of $(Cr_{1-x}V_x)_2AlC$ solid solutions, J. Alloys. Compd. 484 (1–2) (2009) 130–133.

[113] Z.-Y. Jiao, T.-X. Wang, S.-H. Ma, Phase stability, mechanical properties and lattice thermal conductivity of ceramic material $(Nb_{1-x}Ti_x)_4AlC_3$ solid solutions, J. Alloys. Compd. 687 (2016) 47–53.

[114] A. Ganguly, T. Zhen, M.W. Barsoum, Synthesis and mechanical properties of Ti_3GeC_2 and $Ti_3(Si_xGe_{1-x})C_2$ (x = 0.5, 0.75) solid solutions, J. Alloys. Compd. 376 (1–2) (2004) 287–295.

[115] S. Dubois, G.P. Bei, C. Tromas, V. Gauthier-Brunet, P. Gadaud, Synthesis, microstructure, and mechanical properties of $Ti_3Sn_{(1-x)}Al_xC_2$ MAX phase solid solutions, Int. J. Appl. Ceram. Tec. 7 (6) (2010) 719–729.

[116] G.P. Bei, V. Gauthier-Brunet, C. Tromas, S. Dubois, R. Scattergood, Synthesis, characterization, and intrinsic hardness of layered nanolaminate Ti_3AlC_2 and $Ti_3Al_{0.8}Sn_{0.2}C_2$ solid solution, J. Am. Ceram. Soc. 95 (1) (2012) 102–107.

[117] I. Salama, T. El-Raghy, M.W. Barsoum, Synthesis and mechanical properties of Nb_2AlC and $(Ti,Nb)_2AlC$, J. Alloys. Compd. 347 (1) (2002) 271–278.

[118] L. Chlubny, J. Lis, M.M. Bućko, D. Kata, Properties of Hot-pressed Ti_2AlN obtained by SHS process. Advanced Ceramic Coatings and Materials for Extreme Environments II, 2012, pp. 171–177.

[119] E.-S. Choi, J. Sung, Q.-m. Wang, K.-H. Kim, A. Busnaina, M.C. Kang, Material properties and machining performance of hybrid Ti_2AlN bulk material for micro electrical discharge machining, Trans. Nonferrous Met. Soc. China 22 (2012) s781–s786.

[120] D.-T. Wan, L.-F. He, L.-L. Zheng, J. Zhang, Y.-W. Bao, Y.-C. Zhou, A new method to improve the high-temperature mechanical properties of Ti_3SiC_2 by substituting Ti with Zr, Hf, or Nb, J. Am. Ceram. Soc. 93 (6) (2010) 1749–1753.

[121] P. Finkel, B. Seaman, K. Harrell, J. Palma, J.D. Hettinger, S.E. Lofland, A. Ganguly, M.W. Barsoum, Z. Sun, S. Li, R. Ahuja, Electronic, thermal, and elastic properties of $Ti_3Si_{1-x}Ge_xC_2$ solid solutions, Phys. Rev. B 70 (8) (2004), 085104.

[122] M.W. Barsoum, I. Salama, T. El-Raghy, J. Golczewski, H.J. Seifert, F. Aldinger, W. D. Porter, H. Wang, Thermal and electrical properties of Nb_2AlC, $(Ti, Nb)_2AlC$ and Ti_2AlC, Metall. Mater. Trans. A 33 (9) (2002) 2775–2779.

[123] J.X. Chen, Y.C. Zhou, J. Zhang, Abnormal thermal expansion and thermal stability of $Ti_3Al_{1-x}Si_xC_2$ solid solutions, Scripta Mater. 55 (8) (2006) 675–678.

[124] T. Cabioch, P. Eklund, V. Mauchamp, M. Jaouen, M.W. Barsoum, Tailoring of the thermal expansion of $Cr_2(Al_x,Ge_{1-x})C$ phases, J. Eur. Ceram. Soc. 33 (4) (2013) 897–904.

[125] H. Hu, X. Chen, X. Zhao, N. Li, Ab initio molecular dynamics study on thermal expansion of solid-solution compounds in MAX phase, Comp. Mater. Sci. 103 (2015) 200–203.

[126] T. Rackl, L. Eisenburger, R. Niklaus, D. Johrendt, Syntheses and physical properties of the MAX phase boride Nb_2SB and the solid solutions Nb_2SBxC_{1-x}(x = 0-1), Phys. Rev. B Condens. Matter Mater. Phys. 3 (5) (2019), 054001.

[127] M.A. Hadi, Superconducting phases in a remarkable class of metallic ceramics, J. Phys. Chem. Solids 138 (2020), 109275.

[128] J.D. Hettinger, S.E. Lofland, P. Finkel, T. Meehan, J. Palma, K. Harrell, S. Gupta, A. Ganguly, T. El-Raghy, M.W. Barsoum, Electrical transport, thermal transport, and elastic properties of M_2AlC(M=Ti, Cr, Nb, and V), Phys. Rev. B 72 (11) (2005), 115120.

[129] A.S. Ingason, A. Petruhins, M. Dahlqvist, F. Magnus, A. Mockute, B. Alling, L. Hultman, I.A. Abrikosov, P.O.Å. Persson, J. Rosen, a nanolaminated magnetic phase: Mn2GaC, Mater. Res. Lett. 2 (2) (2013) 89–93.

[130] I.P. Novoselova, A. Petruhins, U. Wiedwald, A.S. Ingason, T. Hase, F. Magnus, V. Kapaklis, J. Palisaitis, M. Spasova, M. Farle, J. Rosen, R. Salikhov, Large uniaxial magnetostriction with sign inversion at the first order phase transition in the nanolaminated Mn_2GaC MAX phase, Sci. Rep. 8 (1) (2018) 2637.

[131] M. Dahlqvist, A.S. Ingason, B. Alling, F. Magnus, A. Thore, A. Petruhins, A. Mockute, U.B. Arnalds, M. Sahlberg, B. Hjörvarsson, I.A. Abrikosov, J. Rosen, Magnetically driven anisotropic structural changes in the atomic laminate Mn_2GaC, Phys. Rev. B 93 (1) (2016) 014410.

[132] M. Dahlqvist, J. Rosen, Impact of strain, pressure, and electron correlation on magnetism and crystal structure of Mn_2GaC from first-principles, Sci. Rep. 10 (1) (2020) 11384.

[133] R. Salikhov, R. Meshkian, D. Weller, B. Zingsem, D. Spoddig, J. Lu, A.S. Ingason, H. Zhang, J. Rosen, U. Wiedwald, M. Farle, Magnetic properties of nanolaminated $(Mo_{0.5}Mn_{0.5})_2GaC$ MAX phase, J. Appl. Phys. 121 (16) (2017), 163904.

[134] C.-C. Lai, Q. Tao, H. Fashandi, U. Wiedwald, R. Salikhov, M. Farle, A. Petruhins, J. Lu, L. Hultman, P. Eklund, J. Rosen, Magnetic properties and structural characterization of layered (Cr0.5Mn0.5)2AuC synthesized by thermally induced substitutional reaction in (Cr0.5Mn0.5)2GaC, APL Mater. 6 (2) (2018), 026104.

[135] S. Lin, P. Tong, B.S. Wang, Y.N. Huang, W.J. Lu, D.F. Shao, B.C. Zhao, W.H. Song, Y.P. Sun, Magnetic and electrical/thermal transport properties of Mn-doped $M_{n+1}AX_n$ phase compounds $Cr_{2-x}Mn_xGaC$ ($0 \le x \le 1$), J. Appl. Phys. 113 (5) (2013), 053502.

[136] A. Mockute, P.O.Å. Persson, F. Magnus, A.S. Ingason, S. Olafsson, L. Hultman, J. Rosen, Synthesis and characterization of arc deposited magnetic $(Cr,Mn)_2AlC$ MAX phase films, Phys. Status Solidi 8 (5) (2014) 420–423.

[137] C.M. Hamm, M. Dürrschnabel, L. Molina-Luna, R. Salikhov, D. Spoddig, M. Farle, U. Wiedwald, C.S. Birkel, Structural, magnetic and electrical transport properties of non-conventionally prepared MAX phases V2AlC and (V/Mn)2AlC, Mater. Chem. Front. 2 (3) (2018) 483–490.

[138] W. Luo, R. Ahuja, Magnetic $Fe_{n+1}AC_n$ (n = 1, 2, 3, and A = Al, Si, Ge) phases: from ab initio theory, J. Phys. Condens. Matter 20 (6) (2008), 064217.

[139] C.M. Hamm, J.D. Bocarsly, G. Seward, U.I. Kramm, C.S. Birkel, Non-conventional synthesis and magnetic properties of MAX phases $(Cr/Mn)_2AlC$ and $(Cr/Fe)_2AlC$, J. Mater. Chem. C 5 (23) (2017) 5700–5708.

[140] Y. Li, J. Lu, M. Li, K. Chang, X. Zha, Y. Zhang, K. Chen, P.O.A. Persson, L. Hultman, P. Eklund, S. Du, J.S. Francisco, Z. Chai, Z. Huang, Q. Huang, Multielemental single-atom-thick A layers in nanolaminated V2(Sn, A)C (A = Fe, Co, Ni, Mn) for tailoring magnetic properties, Proc. Natl. Acad. Sci. U. S. A. 117 (2) (2020) 820–825.

[141] H.B. Zhang, Y.C. Zhou, Y.W. Bao, M.S. Li, Improving the oxidation resistance of Ti_3SiC_2 by forming a $Ti_3Si_{0.9}Al_{0.1}C_2$ solid solution, Acta Mater. 52 (12) (2004) 3631–3637.

[142] X.H. Wang, F.Z. Li, J.X. Chen, Y.C. Zhou, Insights into high temperature oxidation of Al_2O_3-forming Ti_3AlC_2, Corros. Sci. 58 (2012) 95–103.

[143] M.W. Barsoum, Oxidation of Ti_3SiC_2 in air, J. Electrochem. Soc. 144 (7) (1997) 2508–2516.

[144] B. Cui, D.D. Jayaseelan, W.E. Lee, Microstructural evolution during high-temperature oxidation of Ti_2AlC ceramics, Acta Mater. 59 (10) (2011) 4116–4125.

[145] G. Bei, B.-J. Pedimonte, T. Fey, P. Greil, Y. Zhou, Oxidation behavior of MAX phase $Ti_2Al_{(1-x)}Sn_xC$ solid solution, J. Am. Ceram. Soc. 96 (5) (2013) 1359–1362.
[146] S. Honda, S. Hashimoto, S. Iwata, Y. Iwamoto, Anisotropic properties of highly textured porous alumina formed from platelets, Ceram. Int. 42 (1) (2016) 1453–1458.
[147] Z.G. Yang, J.B. Yu, C.J. Li, Y.B. Zhong, W.D. Xuan, Z.M. Ren, Q.L. Wang, Y.M. Dai, H. Wang, Preparation of textured porous Al_2O_3 ceramics by slip casting in a strong magnetic field and its mechanical properties, Cryst. Res. Technol. 50 (8) (2015) 645–653.
[148] Z. Zhang, X. Duan, B. Qiu, Z. Yang, D. Cai, P. He, D. Jia, Y. Zhou, Anisotropic properties of textured h-BN matrix ceramics prepared using $3Y_2O_3$-$5Al_2O_3$(-4MgO) as sintering additives, J. Eur. Ceram. Soc. 39 (5) (2019) 1788–1795.
[149] H.T. Liu, J. Zou, D.W. Ni, W.W. Wu, Y.M. Kan, G.J. Zhang, Textured and platelet-reinforced ZrB_2-based ultra-high-temperature ceramics, Scripta Mater. 65 (1) (2011) 37–40.
[150] Z. Yang, J. Yu, K. Deng, Z. Ren, H. Fu, Preparation of c-axis textured TiB_2 ceramics by a strong magnetic field of 6 T assisted slip-casting process, Mater. Lett. 217 (2018) 96–99.
[151] Z. Zhang, X. Duan, B. Qiu, Z. Yang, D. Cai, P. He, D. Jia, Y. Zhou, Preparation and anisotropic properties of textured structural ceramics: a review, J. Adv. Ceram. 8 (3) (2019) 289–332.
[152] M. Yan, X. Duan, Z. Zhang, X. Liao, X. Zhang, B. Qiu, Z. Wei, P. He, J. Rao, X. Zhang, D. Jia, Y. Zhou, Effect of ball milling treatment on the microstructures and properties of Cr_2AlC powders and hot pressed bulk ceramics, J. Eur. Ceram. Soc. 39 (16) (2019) 5140–5148.
[153] Y. Liu, Y. Li, F. Li, H. Cui, Y. Pu, S. Guo, Z. Shi, Highly textured Ti_2AlN ceramic prepared via thermal explosion followed by edge-free spark plasma sintering, Scripta Mater. 136 (2017) 55–58.
[154] T. Uchikoshi, T.S. Suzuki, Y. Sakka, Crystalline orientation of alumina ceramics prepared by electrophoretic deposition under a high magnetic field, J. Mater. Sci. 41 (24) (2006) 8074–8078.
[155] W.D. Fei, Solid State Physics (in Chinese), Harbin Institute of Technology Press, Harbin (CN), 2014.
[156] L. Zhang, J. Vleugels, O. Van der Biest, Slip casting of alumina suspensions in a strong magnetic field, J. Am. Ceram. Soc. 93 (10) (2010) 3148–3152.
[157] F.K. Lotgering, Topotactical reactions with ferrimagnetic oxides having hexagonal crystal structures—I, J. Inorg. Nucl. Chem. 9 (2) (1959) 113–123.
[158] C.F. Hu, Y. Sakka, H. Tanaka, T. Nishimura, S. Grasso, Fabrication of textured Nb_4AlC_3 ceramic by slip casting in a strong magnetic field and spark plasma sintering, J. Am. Ceram. Soc. 94 (2) (2011) 410–415.
[159] C.F. Hu, Y. Sakka, S. Grasso, T. Suzuki, H. Tanaka, Tailoring $Ti3SiC_2$ ceramic via a strong magnetic field alignment method followed by spark plasma sintering, J. Am. Ceram. Soc. 94 (3) (2011) 742–748.
[160] S.Q. Li, K. Sassa, S. Asai, Textured crystal growth of Si_3N_4 ceramics in high magnetic field, Mater. Lett. 59 (2-3) (2005) 153–157.
[161] X. Zhu, Y. Sakka, Textured silicon nitride: processing and anisotropic properties, Sci. Technol. Adv. Mater. 9 (3) (2008), 033001.
[162] P. Finkel, J.D. Hettinger, S.E. Lofland, M.W. Barsoum, T. El-Raghy, Magnetotransport properties of the ternary carbide $Ti3SiC_2$: Hall effect, magnetoresistance, and magnetic susceptibility, Phys. Rev. B 65 (3) (2001), 035113.
[163] T. Lapauw, K. Vanmeensel, K. Lambrinou, J. Vleugels, A new method to texture dense $M_{n+1}AX_n$ ceramics by spark plasma deformation, Scripta Mater. 111 (2016) 98–101.
[164] C. Hu, Y. Sakka, T. Nishimura, S. Guo, S. Grasso, H. Tanaka, Physical and mechanical properties of highly textured polycrystalline Nb4AlC_3 ceramic, Sci. Technol. Adv. Mater. 12 (4) (2011), 044603.
[165] H.B. Zhang, C.F. Hu, K. Sato, S. Grasso, M. Estili, S.Q. Guo, K. Morita, H. Yoshida, T. Nishimura, T.S. Suzuki, M.W. Barsoum, B.N. Kim, Y. Sakka, Tailoring Ti_3AlC_2 ceramic with high anisotropic physical and mechanical properties, J. Eur. Ceram. Soc. 35 (1) (2015) 393–397.
[166] Y. Mizuno, K. Sato, M. Mrinalini, T.S. Suzuki, Y. Sakka, Fabrication of textured Ti_3AlC_2 by spark plasma sintering and their anisotropic mechanical properties, J. Ceram. Soc. Jpn. 121 (1412) (2013) 366–369.
[167] Y. Uchida, K. Morita, T.S. Suzuki, T. Nishimura, K. Fujimoto, Y. Sakka, Fabrication and mechanical properties of textured Ti_3SiC_2 systems using commercial powder, Mater. Trans 59 (5) (2018) 829–834.
[168] B.J. Kooi, R.J. Poppen, N.J.M. Carvalho, J.T.M. De Hosson, M.W. Barsoum, Ti_3SiC_2: A damage tolerant ceramic studied with nano-indentations and transmission electron microscopy, Acta Mater. 51 (10) (2003) 2859–2872.
[169] Z. Sun, A. Murugaiah, T. Zhen, A. Zhou, M. Barsoum, Microstructure and mechanical properties of porous Ti_3SiC_2, Acta Mater. 53 (16) (2005) 4359–4366.
[170] C.F. Hu, Y. Sakka, S. Grasso, T. Nishimura, S.Q. Guo, H. Tanaka, Shell-like nanolayered Nb_4AlC_3 ceramic with high strength and toughness, Scripta Mater. 64 (8) (2011) 765–768.
[171] X.H. Wang, Y.C. Zhou, Layered machinable and electrically conductive Ti_2AlC and Ti_3AlC_2 ceramics: a review, J. Mater. Sci. Technol. 26 (5) (2010) 385–416.
[172] M.W. Barsoum, C.J. Rawn, T. El-Raghy, A.T. Procopio, W.D. Porter, H. Wang, C. R. Hubbard, Thermal properties of Ti_4AlN_3, J. Appl. Phys. 87 (12) (2000) 8407–8414.
[173] Bouhemadou, First-principles study of structural, electronic and elastic properties of Nb_4AlC_3, Rev. Bras. Fisioter. 40 (1) (2010) 52–57.
[174] Y.C. Zhou, X.H. Wang, Z.M. Sun, S.Q. Chen, Electronic and structural properties of the layered ternary carbide Ti_3AlC_2, J. Mater. Chem. 11 (9) (2001) 2335–2339.
[175] T. Scabarozi, A. Ganguly, J.D. Hettinger, S.E. Lofland, S. Amini, P. Finkel, T. El-Raghy, M.W. Barsoum, Electronic and thermal properties of $Ti_3Al(C_{0.5},N_{0.5})_2$, $Ti_2Al(C_{0.5},N_{0.5})$ and Ti_2AlN, J. Appl. Phys. 104 (7) (2008), 073713.
[176] G.M. Song, Y.T. Pei, W.G. Sloof, S.B. Li, J.T.M. De Hosson, S. van der Zwaag, Early stages of oxidation of $Ti3AlC_2$ ceramics, Mater. Chem. Phys. 112 (3) (2008) 762–768.
[177] L. Xu, D. Zhu, Y. Liu, T.S. Suzuki, B.-n. Kim, Y. Sakka, S. Grasso, C. Hu, Effect of texture on oxidation resistance of Ti_3AlC_2, J. Eur. Ceram. Soc. 38 (10) (2018) 3417–3423.